STUDIES ON MATTER WAVE BRIGHT SOLITONS IN PARITY-TIME SYMMETRIC BOSE-EINSTEIN CONDENSATES

Thesis submitted to

Cochin University of Science and Technology

in partial fulfillment of the requirements
for the award of the degree of

DOCTOR OF PHILOSOPHY

by

Lini Devassy
Theory Division
Department of Physics
Cochin University of Science and Technology
Kochi - 682022

July 2017

Studies on matter wave bright solitons in parity-time symmetric Bose-Einstein condensates
PhD thesis in the field of $\mathcal{PT}$ symmetric BEC

Author
Lini Devassy
Department of Physics
Cochin University of Science and Technology
Kochi-682022
linidevassy@cusat.ac.in

Research Supervisor
Prof V. C. Kuriakose(Rtd.)
Department of Physics
Cochin University of Science and Technology
Kochi-682022
vck@cusat.ac.in

Dedicated to my Amma and Appachan.

CERTIFICATE

Certified that the work presented in this thesis is a bonafide research work done by Ms. Lini Devassy, under our guidance in the Department of Physics, Cochin University of Science and Technology, Kochi- 682022, India, and has not been included in any other thesis submitted previously for the award of any degree. All the relevant corrections and modifications suggested by the audience during the pre-submission seminar and recommended by the Doctoral committee have been incorporated in this thesis.

Prof. V. C. Kuriakose
(Supervising Guide)

Kochi-682022
July, 2017

Prof. Ramesh Babu T.
(Joint Guide)

DECLARATION

I hereby declare that the work presented in this thesis is based on the original research work done by me under the guidance of Prof. V. C. Kuriakose (Rtd.) and Dr. Ramesh Babu T., Department of Physics, Cochin University of Science and Technology, Kochi-682022, India, and has not been included in any other thesis submitted previously for the award of any degree.

Kochi-682022
July, 2017

Lini Devassy

Contents

PREFACE

The fundamental axiom of quantum mechanics assumes the Hermiticity of operators associated with any measurable quantities, observables. But there are certain class of complex non-Hermitian Hamiltonians which possess real spectra for certain parameter regimes if they obey parity-time symmetry($\mathcal{PT}$ symmetry); without losing any of the essential features of quantum mechanics. The parity reflection operator $\mathcal{P}$ and time reversal operator $\mathcal{T}$ are defined by their actions on the position and momentum operators $\hat{x}$ and $\hat{p}$ respectively as $\hat{p} \to -\hat{p}$, $\hat{x} \to -\hat{x}$, $\imath \to \imath$ and $\hat{p} \to -\hat{p}$, $\hat{x} \to \hat{x}$, $\imath \to -\imath$. If the $\mathcal{PT}$ symmetry of the Hamiltonian is not broken, then these non-Hermitian Hamiltonians will exhibit all the properties of a quantum theory described by the Hermitian Hamiltonian. Bose-Einstein condensate(BEC), a true quantum system, is used for theoretical and experimental studies of interplay between nonlinearity and $\mathcal{PT}$ symmetry. In this thesis, we have studied theoretically the matter wave bright solitons in $\mathcal{PT}$ symmetric BECs. The thesis is organized into six chapters:

Chapter 1 : In this chapter, a general introduction of features of $\mathcal{PT}$ symmetric non-Hermitian Hamiltonians is given. Since the thesis deals with $\mathcal{PT}$ symmetric BEC, a theoretical frame work for both non-interacting and interacting Bose gas (Gross-Pitaevskii mean field theory) is also shown here. An overview of the analytical and numerical methods used in the thesis is also presented.

Chapter 2 : Dynamics and properties of nonlinear matter waves in a quasi 1-D attractive BEC subjected to a $\mathcal{PT}$-symmetric trapping potential are discusssed in this chapter. We have employed both numerical and analytical methods to find the solutions of Gross-Pitaevskii equation (GPE). Stationary solutions of GPE are sought numerically by standard relaxation technique based on pseudospectral differentiation with Fourier differentiation matrices. We have used the variational approach suitable for non-Hermitian systems to obtain the approximated solutions of GPE using fundamental equations based on the Rayleigh-Ritz approximation. We have addressed how the shape of the imaginary part of the potential, that is, a gain-

loss mechanism, affects the self-localization and the stability of the condensate. The stability of the stationary solutions are analyzed using the Bogoliubov-de Gennes (BDG) equations and the results obtained from linear stability analysis have been checked numerically by computing soliton dynamics in the presence of noise.

Chapter 3 : The unidirectional properties shown by the $\mathcal{PT}$ symmetric defect in a quasi 1-D attractive BEC is shown in chapter 3. For that we have analyzed the scattering of soliton by $\mathcal{PT}$ symmetric defects(in terms of the reflection, transmission and capture coefficients), specifically studying the influence of the transverse profile of the imaginary component of the defect.

Chapter 4 : This chapter deals with the existence and stability of matter wave bright solitons governed by the GPE with repulsive interaction between the atoms of the condensate. The condensate is trapped in a super-Gaussian $\mathcal{PT}$-symmetric potential. We considered a cigar shaped condensate and studied the interplay among diffusion, repulsive nonlinearity and gain-loss mechanism on the existence of the matter wave solitons. The effects of gain-loss profiles are analyzed by considering two different transverse profiles for the imaginary part of the $\mathcal{PT}$-symmetric potential. We have checked the stability of the obtained solutions using linear stability analysis and results are confirmed using dynamical evolutions of the solutions.

Chapter 5 : Chapter 5 discusses the dynamics of BEC with $\mathcal{PT}$ symmetry beyond mean field Theory. We have considered the GPE with mean field correction terms(quantum fluctuations and effective range expansion) added to it. By means of variational approach we have obtained expressions for dynamics of soliton parameters. The effect of varying the strength of $\mathcal{PT}$ symmetric trapping potential along with mean field correction terms on the scattering process is also examined. The collective excitation frequencies in a quasi 1-D BEC trapped in a Gaussian PT symmetric potential are calculated using variational approach and have shown the effects of the trapping potential on the excitation frequencies.

Chapter 6 : A summary of the results is given in this chapter and the possible applications and future plan of studies are also presented.

List of publications

Papers published in refereed journals and presented in seminars and conferences.

Refereed Journals.

1. C. P. Jisha, Lini Devassy, Alessandro Alberucci and V C Kuriakose, *Influence of the imaginary component of the photonic potential on the properties of solitons in PT-symmetric systems*, Phys. Rev. A, 90, 043855 (2014).

2. Lini Devassy, C. P. Jisha, Alessandro Alberucci and V. C. Kuriakose, *Parity-time-symmetric solitons in trapped Bose-Einstein condensates and the influence of varying complex potentials: A variational approach*, Phys. Rev. E, 92, 022914 (2015).

3. Lini Devassy, C. P. Jisha, Alessandro Alberucci and V. C. Kuriakose, *Nonlinear waves in repulsive media supported by spatially localized parity-time symmetric potentials*, Phys. Lett. A, 381, 1955(2017).

4. Lini Devassy and V. C. Kuriakose, *Variational analysis of soliton scattering by PT symmetric potential in a 1-D Bose-Einstein condensate* (Submitted for publication).

5. Lini Devassy and V. C. Kuriakose, *Collective excitations in a quasi 1-D Bose-Einstein Condensate trapped in a PT -symmetric potential: Mean field theory and beyond*(Submitted for publication).

6. Lini Devassy, V. C. Kuriakose, Alessandro Alberucci and C. P. Jisha, *Interaction of solitons with PT-symmetric interface* (Article in preparation).

Conferences.

1. *A variational study of non-hermitian, $\mathcal{PT}$-symmetric BEC system with super-Gaussian trapping potential*, National conference, NCMOMS, 17-18 December 2015, Farook College, Kozhikode.

2. *Solitons in Kerr media with $\mathcal{PT}$-symmetric super-Gaussian potentials*, International conference,PSWS, 12-13 March 2015, St. Teresa's college, Ernakulam.

3. *Rotating Bose- Einstein condensate- A variational approach*, National conference, NCNSD, 27-30 January 2011, Tiruchirappalli.

ACKNOWLEDGMENTS

Although my name is the only one that appears on the cover of this Ph.D. thesis, the work presented in this thesis cannot be achieved by myself alone. First and foremost, I express my deepest gratitude to my supervisor Dr.V.C.Kuriakose, Professor(Rtd.), Dept. of Physics, Cochin University of Science and Technology for his constant support and advice. I am fortunate to work under him who has wide knowledge and good research experience. His ideas and visions are thought-provoking and has inspired me in my scientific journey. He is an understanding supervisor to all his students and the working environment that he created in the IRC (IUCAA Resource Centre) makes me to work like in a home rather than in a lab. I find no words to quantify all the support and freedom he has given to me throughout these years.

I would also like to acknowledge my Joint Guide Dr.Ramesh Babu T., for his care and support.

I would like to acknowledge Dr. C. P. Jisha, Centro de Física do Porto, Portugal for introducing me to the topic of parity-time symmetry and her

tireless patience to clarify my doubts even over nights. I have learnt too many things from her especially in numerical simulations. I am extremely indebted to her for her unconditional support through out my research work. My sincere thanks to Dr. Alessandro Alberucci, Tampere University of Technology, Finland for the fruitful discussions and collaborations.

I would like to acknowledge Cochin University of Science and Technology for providing me UJRF during 2010 (Dec)-2012 (March) and UGC for RFSMS-BSR fellowship during 2012 (April)-2017 (March).

Let me express my sincere thanks to Dr. M. Junaid Bushiri, Head of the Department of Physics and former Heads of this department for providing the necessary facilities for my research work. I thank all the members of the faculty, library and office staff of the department for the help they rendered during the entire period of my research study.

I really enjoyed the friendship and support of my seniors and juniors, Nima chechi, Bavya, Nijo, Tharanath, Saneesh, Vivek, Prasobh, Prasia and Jishnu. I entertained the spare time being with Athira, Paxy, Krishna and Thaskeena. Also I remember the helping hands of Jerin, Dinto and Navaneeth.

I would like to thank all research scholars, M. Phil. and M. Sc. students of Physics Department for the moments I had with them.

This will not be complete without thanking my family, my better half Jomon, daughter Heleina for their patience, understanding and love. I cannot forget the support given by my parents(P. P. Devassy and Rossy

Devassy) and in-laws(P. V. Mathai and Sosamma Mathai) to keep a balance in my life as a mother and as a research student.

Above all, I express my gratefulness to the Almighty God for making me able to achieve whatever I have.

Lini Devassy

1
Introduction

The measurements of energy spectrum of a physical system yield real values and hence in standard quantum mechanics, Hermitian Hamiltonians are used. But there are physical systems exhibiting dissipation, decays, resonances etc., represented by non-Hermitian Hamiltonians and non-Hermitian Hamiltonians possess complex energy eigen values. But there exists a class of parity-time symmetric($\mathcal{PT}$ symmetric) non-Hermitian Hamiltonians possessing real eigen values without violating any of the fundamental axioms of quantum mechanics. The parity operator $\mathcal{P}$ and time reversal operator $\mathcal{T}$ are defined by their action on the position and momentum operators $\hat{x}$ and $\hat{p}$ as $\hat{p} \to -\hat{p}$, $\hat{x} \to -\hat{x}$, $\imath \to \imath$ and $\hat{p} \to -\hat{p}$, $\hat{x} \to \hat{x}$, $\imath \to -\imath$, respectively. The concept of $\mathcal{PT}$ symmetry permits a complex potential in a Hamiltonian such that it should satisfy $V(\hat{x}) = V^*(-\hat{x})$ which is a necessary but not a sufficient condition and $*$ stands for complex conjugation. Such a potential signifies an even profile for the real part of the potential and an odd symmetry for the imaginary part. The imaginary part of the complex potential corresponds to the interaction of the system with the environment. These interactions are highly constrained so that gain from the environment and loss to the environment are exactly balanced thereby keeping the system in an equilibrium state. Above a critical point, known as the exceptional point, $\mathcal{PT}$-symmetry can be spontaneously broken even though the underlying Hamiltonian satisfies the $\mathcal{PT}$-symmetric condition.

Bose-Einstein condensate(BEC) seems to be a true quantum system for theoretical and experimental studies of interplay between nonlinearity and phenomena shown by Parity-Time ($\mathcal{PT}$) symmetry. In this thesis, we have studied theoretically the matter wave bright solitons in $\mathcal{PT}$ symmetric BECs. Before presenting the details of the research work, basic introduction of BEC, $\mathcal{PT}$ symmetry, historical development and current status of $\mathcal{PT}$ symmetric BECs are given below. An introduction to the basic analytical and numerical methods used in this thesis is also presented in this chapter.

1.1 Bose-Einstein condensates

The existence of a peculiar state of matter, BEC, was first predicted by S. N. Bose[1] and Albert Einstein[2, 3] in 1920's in a system of non-interacting bosons such that system exhibits a phase transition at ultra cold temperatures and a large fraction of the atoms macroscopically populate at the ground state. The relevant theoretical frame work for the condensation in a uniform ideal gas(non-interacting gas) can be understood by considering quantum mechanics of many particle system in which particles are identical and indistinguishable[4, 5]. As an example, if we are taking a two particle wave function in a one dimensional box, the particles are said to be identical when the observable square modulus of quantum mechanical wave functions of the system does not change under particle exchange; i.e., $|\psi(x_1, x_2)|^2$=$|\psi(x_2, x_1)|^2$, $\psi(x_1, x_2) = \exp(\imath\alpha)\psi(x_2, x_1)$ and hence shows two possibilities i.e., the wave function must be either symmetric or antisymmetric under the exchange of the two particles. Hence the spin-statistics theorem is stated as 1) systems of identical particles with integer spin(s = 0,1,2...), known as bosons, have wave functions which are symmetric under interchange of any pair of particles and obey

Bose-Einstein statistics and 2) fermions with half-odd-integer spin(s = 1/2, 3/2,...), have wave functions which are antisymmetric under particle interchange, obeying Fermi-Dirac statistics. So, at low temperatures, bosons behave entirely different from fermions (which obey Pauli's exclusion principle) in such a way that an unlimited number of them can condense into same energy state giving rise to a peculiar state of matter: the Bose-Einstein condensate.

For non-interacting bosons in thermodynamic equilibrium, the mean occupation number(or the average number of particles) for a single-particle energy ϵ_k is given by

$$f(\epsilon_k) = \frac{1}{\exp(\beta(\epsilon_k - \mu)) - 1}, \tag{1.1}$$

where μ, the chemical potential determined by the condition that the total number of particles be equal to the sum of the occupancies of the individual levels and $\beta = 1/kT$. i.e., $\Sigma_k f(\epsilon_k) = N$, with N being the total number of particles. The chemical potential must be small or equal to the smallest energy level, $\mu \leq \epsilon_0$, otherwise the system will have negative occupation numbers which is meaningless.

At high temperatures the chemical potential of this system lies well below ϵ_0, and the mean occupation number of any state is much less than unity(i.e., $\exp(\beta(\mu - \epsilon_k)) \ll 1$). When the temperature is decreased, the chemical potential rises and the mean occupation number increases. Hence the occupation number of the single-particle ground state is arbitrarily large compared to any excited single-particle state. The number of particles in excited states will be much less than the total number of particles N in the system. That means, the remaining particles will obviously occupy the ground state: the system has now become Bose-Einstein condensate. The temperature at which the above said condensation starts

is termed as Bose-Einstein transition temperature and is given by,

$$T_c = \frac{2\pi\hbar^2}{k_B m}\left(\frac{n}{\zeta(3/2)}\right)^{2/3}, \tag{1.2}$$

with n, the particle density and $\zeta(3/2) \approx 2.612$. Since the system is in the thermodynamic limit, the particle density at the ground state $n_0 = N_0/V$ stays finite ($N \to \infty$, $V \to \infty$ hence $n = N/V$ remains constant).

Later it was found that the assumed 'non-interacting' nature of the Bose gas is not sufficient to get into real situations and it demands a mean filed theory(Gross-Pitaevskii mean field theory) which assumes both an external trapping and inter-particle interactions. The experimental realization of BEC became thinkable after the invention of powerful methods in 1970's for cooling alkali metal atoms by lasers [6, 7] and evaporative cooling techniques(where more energetic atoms are removed[8]), combined with development of novel traps. The exploitation of these technologies led to the first observation of BEC of a weakly interacting atomic Bose gas in the laboratory in 1995 by JILA group led by E. Cornell and C. Wieman in dilute gases of ^{87}Rb below 170 nK [9] and Ketterle's groups at MIT succeeded in ^{23}Na [10]. These achievements merited those scientists to receive the 2001 Nobel Prize for physics. Again, BEC of ^{7}Li with an attractive interaction was created by Hulet's group at Rice University[11]. Some other examples are atomic hydrogen which was achieved in 1998[12] by D. G. Fried et.al., metastable Helium[13], Potassium [14], Cesium[15], Ytterbium[16], Calcium [17], and Strontium[18, 19]. Special attention is being paid to BEC created from Chromium[20], Dysprosium [21] and Erbium [22] owing to their large magnetic dipole-dipole interactions.

The dynamics of the condensate can thus theoretically be described with the Gross-Pitaevskii equation(GPE)[23] which is effectively a mean-field approximation for the inter particle interactions at temperatures $T < T_c$ (T_c is critical condensation temperature) and in dilute limit. The

required GPE for weakly interacting dilute Bose gas (which is similar to nonlinear Schrödinger equation (NLSE)) upon which the main discussions of the present thesis have been done, is derived in the following section[23, 24].

A related point to mention is the fermionic condensate; cooling to extremely low temperatures makes the fermions to 'pair up' to form bosonic compound particles(molecules or Cooper pairs) and these compound particles exhibit condensation. The first fermionic condensate was created by Deborah S. Jin in 2003[25, 26].

1.2 Gross-Pitaevskii mean field theory

The dynamics of a BEC can be well described by means of an effective mean-field theory which means that the action felt by a given particle due to the rest of the particles is substituted by the mean field action of the system over the particle. This approximation is fairly good since the gas is diluted and it is relevant for experimental realization of BEC. Also, this approach is much simpler than treating the full many-body Schrödinger equation and this theory accurately describes the static and dynamic properties of BECs. Since, BEC is a dilute ultracold gas which has only binary collisions at these low energy states, the parameter, s-wave scattering length a, alone is sufficient to describe the inter-particle interaction.

The dynamics of the condensate can theoretically be described with the GPE which is a classical nonlinear evolution equation. It was derived independently by E. P. Gross[27] and L. P. Pitaevskii[28] in 1961. In fact, this is a variant of nonlinear Schrödinger equation (NLSE)[23, 24, 29, 30], which is a universal model describing the evolution of complex field envelopes in nonlinear dispersive media. In BEC, the nonlinearity

is due to the interatomic interactions and it is considered via an effective mean-field. Another important factor is that the GP equation successfully predicts and describes the experimentally relevant nonlinear effects and nonlinear states such as solitons and vortices. The GPE is derived from the second quantized Hamiltonian for a gas of interacting bosons.

The many-body Hamiltonian for N bosons of mass m interacting by two-body collisions and confined in an external potential $V_{ext}(r)$ is given in second quantized form as[4, 23, 24, 31, 32],

$$\begin{aligned}\hat{H} = &\int d\boldsymbol{r}\hat{\Psi}^{\dagger}(\boldsymbol{r},t)\left[-\frac{\hbar^2}{2m}\nabla^2 + V_{ext}(\boldsymbol{r})\right]\hat{\Psi}(\boldsymbol{r},t) \\ &+ \frac{1}{2}\int d\boldsymbol{r}\int d\boldsymbol{r}^{'}\hat{\Psi}^{\dagger}(\boldsymbol{r},t)\hat{\Psi}^{\dagger}(\boldsymbol{r}^{'},t)V(\boldsymbol{r}-\boldsymbol{r}^{'})\hat{\Psi}(\boldsymbol{r},t)\hat{\Psi}(\boldsymbol{r}^{'},t),\end{aligned} \tag{1.3}$$

where $\hat{\Psi}(\boldsymbol{r},t)$ and $\hat{\Psi}^{\dagger}(\boldsymbol{r},t)$ are the boson annihilation and creation field operators respectively, which satisfy the equal-time commutation relations [4],

$$\left[\hat{\Psi}(\boldsymbol{r},t),\hat{\Psi}(\boldsymbol{r}^{'},t)\right] = \left[\hat{\Psi}^{\dagger}(\boldsymbol{r},t),\hat{\Psi}^{\dagger}(\boldsymbol{r}^{'},t)\right] = 0, \tag{1.4}$$

and,

$$\left[\hat{\Psi}(\boldsymbol{r},t),\hat{\Psi}^{\dagger}(\boldsymbol{r}^{'},t)\right] = \delta(\boldsymbol{r}-\boldsymbol{r}^{'}). \tag{1.5}$$

$V(\boldsymbol{r}-\boldsymbol{r'})$ is the two-body interatomic potential which can be simplified by assuming the case of a dilute ultracold gas with binary collisions at low energy. In this constraint, the interatomic potential can be replaced by an effective interaction represented by a delta-function potential [23, 24, 33, 34], since the s-wave scattering length a is small compared to the de-Broglie wavelength. So,

$$V(\boldsymbol{r}-\boldsymbol{r}^{'}) = g\delta(\boldsymbol{r}-\boldsymbol{r}^{'}), \tag{1.6}$$

where the coupling constant g is given by,

$$g = \frac{4\pi\hbar^2 a}{m},$$

with a is the s-wave scattering length which alone is sufficient to describe the inter-particle interaction in the low energy case as stated above.

The time evolution of the field operator $\hat{\Psi}(\boldsymbol{r},t)$ is then obtained from the Heisenberg equation of motion,

$$\imath\hbar\frac{\partial\hat{\Psi}(\boldsymbol{r},t)}{\partial t} = \left[\hat{\Psi}(\boldsymbol{r},t),\hat{H}\right]. \tag{1.7}$$

Assuming the mean-field theory for dilute gases, formed by N. N. Bogolubov in 1947[35], the field operator $\hat{\Psi}(\boldsymbol{r})$ is decomposed in to[23, 24, 36],

$$\hat{\Psi}(\boldsymbol{r}) = \psi(\boldsymbol{r},t) + \hat{\psi}(\boldsymbol{r},t), \tag{1.8}$$

where the complex function $\psi(\boldsymbol{r},t)$ is the expectation value of the field operator, regarding the same as the order parameter and it is called the macroscopic wavefunction of the condensate. The second one, $\hat{\psi}(\boldsymbol{r},t)$ represents the non-condensed fraction present even below the transition temperature, T_c which may be thermally-excited atoms or quantum-mechanical fluctuations in the system. The expectation value of the field operator $\hat{\Psi}(\boldsymbol{r})$ is taken such that $\left\langle\hat{\psi}(\boldsymbol{r},t)\right\rangle = 0$. Substituting the Hamiltonian (Eq.1.3) in to the equation of motion (Eq.1.7) and then using the commutation relations(Eqs.1.4,1.5) and simplified form of potential (Eq.1.6), and also substituting the decomposed form of field operator $\hat{\Psi}(\boldsymbol{r})$, we get,

$$\begin{aligned}\imath\hbar\frac{\partial\psi(\boldsymbol{r},t)}{\partial t} = &\left\{-\frac{\hbar^2}{2m}\nabla^2 + V_{ext}(\boldsymbol{r}) + g\left(n_c(\boldsymbol{r},t) + 2\tilde{n}(\boldsymbol{r},t) + \tilde{m}(\boldsymbol{r},t)\right)\right\}\psi(\boldsymbol{r},t)\\ &+ g\left\langle\hat{\psi}^\dagger(\boldsymbol{r},t)\hat{\psi}(\boldsymbol{r},t)\hat{\psi}(\boldsymbol{r},t)\right\rangle,\end{aligned} \tag{1.9}$$

with the condensate density $n_c(\boldsymbol{r},t) = |\psi(\boldsymbol{r},t)|^2$ and the non-condensate density $\tilde{n}(\boldsymbol{r},t) = \left\langle\hat{\psi}^\dagger(\boldsymbol{r},t)\hat{\psi}(\boldsymbol{r},t)\right\rangle$(which constitutes the depletion of the condensate by collisional interactions). $\tilde{m}(\boldsymbol{r},t)$ represents the off-diagonal non-condensate density due to the anomalous correlations between the

non-condensed atoms and is given by $\tilde{m}(\boldsymbol{r},t) = \left\langle \hat{\psi}(\boldsymbol{r},t)\hat{\psi}(\boldsymbol{r},t)\right\rangle$. The final term in Eq.1.9, viz, $\left\langle \hat{\psi}^{\dagger}(\boldsymbol{r},t)\hat{\psi}(\boldsymbol{r},t)\hat{\psi}(\boldsymbol{r},t)\right\rangle$ corresponds to the three field correlation function. The non-condensate fraction in trapped atomic gases at temperatures well below T_c is calculated to be less than 1% [31, 37, 38], and hence it is reasonable to assume that the non-condensate density, the off-diagonal non-condensate density, and the correlation functions are negligible. Hence Eq.1.9 yields the evolution of complex classical field $\psi(\boldsymbol{r},t)$ [34],

$$\imath\hbar\frac{\partial\psi(\boldsymbol{r},t)}{\partial t} = \left\{-\frac{\hbar^2}{2m}\nabla^2 + V_{ext}(\boldsymbol{r}) + g\left(\left|\psi(\boldsymbol{r},t)\right|^2\right)\right\}\psi(\boldsymbol{r},t). \tag{1.10}$$

The conserved quantity is the total number of atoms, N, according to,

$$N = \int \left|\psi(\boldsymbol{r},t)\right|^2 d\boldsymbol{r}. \tag{1.11}$$

The strength of nonlinearity is determined by the coefficient g in Eq.1.10 and it may be either positive or negative depending on scattering length $a > 0$ (repulsive interaction) or $a < 0$ (attractive interaction). It may be regarded as the defocusing or focusing Kerr-type nonlinearities in the context of nonlinear optics [39, 40]. By manipulating the interactions and collision properties of the atoms, one can vary either the sign or the magnitude of the scattering length which leads to important experimental observations like the formation of bright matter-wave solitons in BEC[41, 42]. Different methods for external potential V_{ext} are used in experiments in which magnetic trapping is employed in earlier experiments [23, 24, 34, 43, 44], and later pure optical confinement was achieved [45–48].

Eq.1.10 is the time-dependent Gross-Pitaevskii equation, which is the basis of the present discussions of the dynamics of BEC in the following chapters. In order to study the static properties of Bose-Einstein condensates, the time independent form of GPE is employed. It is obtained from

Eq.1.10 by making the ansatz,

$$\psi(\boldsymbol{r},t) = \psi(\boldsymbol{r})\exp(\frac{-\imath\mu t}{\hbar}), \tag{1.12}$$

where μ is the chemical potential and substituting it in Eq.1.10 will follow,

$$\mu\psi(\boldsymbol{r}) = \left\{-\frac{\hbar^2}{2m}\nabla^2 + V_{ext}(\boldsymbol{r}) + g\left(|\psi(\boldsymbol{r})|^2\right)\right\}\psi(\boldsymbol{r}); \tag{1.13}$$

where the eigen value is the chemical potential μ instead of the energy E as in the linear Schrödinger equation [23].

Next, we briefly look at the basics of $\mathcal{PT}$ symmetry transformations. The action of parity operator $\mathcal{P}$ and time reversal operator $\mathcal{T}$ are reviewed first and then follows their combined action.

1.3 $\mathcal{PT}$ symmetry

Symmetry transformations are the special ways of changing our point of view such that the laws of nature do not change [49], i.e., the new physical state obtained after the symmetry transformation obeys the same laws as the old one possessed and the transition probabilities $\langle\Psi,\Phi\rangle$, the modulus square of the quantum mechanical scalar product between arbitrary states Ψ and Φ remain invariant. According to a fundamental theorem by Eugene Wigner [50], there are two possibilities to fullfill the transition probability invariant; 1) the effect of a symmetry transformation on any state vector Ψ is a transformation $\Psi \to \hat{U}\Psi$ with $\hat{U}$, a linear unitary operator and obey,

$$\left\langle\hat{U}\Psi|\hat{U}\Phi\right\rangle = \left\langle\Psi|\hat{U}^\dagger\hat{U}\Phi\right\rangle = \langle\Psi|\Phi\rangle\,, \tag{1.14}$$

with $\hat{U}^\dagger\hat{U} = \mathbf{1}$ and 2) with $\hat{U}$, as an antilinear operator obeying antiunitary:

$$\hat{U}\left(\alpha\,|\Psi\rangle + \beta\,|\Phi\rangle\right) = \alpha^*\hat{U}\,|\Psi\rangle + \beta^*\hat{U}\,|\Phi\rangle\,, \tag{1.15}$$

and

$$\left\langle \hat{U}\Psi|\hat{U}\Phi\right\rangle = \langle\Psi|\Phi\rangle^* . \tag{1.16}$$

Now, we have to consider two discrete symmetry operators, the space inversion or parity operator $\mathcal{P}$ and the time reversal operator $\mathcal{T}$ for the present thesis. The operator on state vector space which gives the space inversion transformation $\boldsymbol{r} \rightarrow -\boldsymbol{r}$ is called the parity operation. The parity operator reverses the signs of the position $\hat{\boldsymbol{r}}$ and the momentum operator $\hat{\boldsymbol{p}}$ as,

$$\mathcal{P}\hat{\boldsymbol{r}}\mathcal{P}^{-1} = -\hat{\boldsymbol{r}}, \tag{1.17}$$

and

$$\mathcal{P}\hat{\boldsymbol{p}}\mathcal{P}^{-1} = -\hat{\boldsymbol{p}}. \tag{1.18}$$

In order to check whether $\mathcal{P}$ is linear or antilinear operator, we have to consider the operation of $\mathcal{P}$ on canonical commutation relation,

$$\begin{aligned} \imath\hbar\delta_{ij} = [\hat{\boldsymbol{r}}_i, \hat{\boldsymbol{p}}_j] &\stackrel{!}{=} \left[-\mathcal{P}\hat{\boldsymbol{r}}_i\mathcal{P}^{-1}, -\mathcal{P}\hat{\boldsymbol{p}}_j\mathcal{P}^{-1}\right] = \mathcal{P}\left(\hat{\boldsymbol{r}}_i\hat{\boldsymbol{p}}_j - \hat{\boldsymbol{p}}_j\hat{\boldsymbol{r}}_i\right)\mathcal{P}^{-1} \\ &= \mathcal{P}\imath\hbar\delta_{ij}\mathcal{P}^{-1}, \end{aligned} \tag{1.19}$$

which should be invariant and it will be satisfied if $\mathcal{P}^{-1}\imath\mathcal{P} = \imath$, hence we can say the parity operator is a linear unitary operator which satisfies $\mathcal{P}^{-1} = \mathcal{P}^\dagger$. The action of parity operator on vectors and wave functions is as follows, $\mathcal{P}\hat{\boldsymbol{r}}\,|\boldsymbol{r}\rangle = \mathcal{P}\boldsymbol{r}\,|\boldsymbol{r}\rangle$ and we can write $\mathcal{P}\hat{\boldsymbol{r}}\,|\boldsymbol{r}\rangle = \mathcal{P}\hat{\boldsymbol{r}}(\mathcal{P}\mathcal{P}^{-1})\,|\boldsymbol{r}\rangle = -\hat{\boldsymbol{r}}\mathcal{P}\,|\boldsymbol{r}\rangle$, that implies $\hat{\boldsymbol{r}}\mathcal{P}\,|\boldsymbol{r}\rangle = -\boldsymbol{r}(\mathcal{P}\,|\boldsymbol{r}\rangle)$. Comparing it with $\hat{\boldsymbol{r}}\,|-\boldsymbol{r}\rangle = -\boldsymbol{r}\,|-\boldsymbol{r}\rangle$, we can write,

$$\mathcal{P}\,|\boldsymbol{r}\rangle = |-\boldsymbol{r}\rangle . \tag{1.20}$$

In order to keep the uniqueness of the eigen functions, the vectors $|-\boldsymbol{r}\rangle$ and $\mathcal{P}\,|\boldsymbol{r}\rangle$ differs in phase; and this phase is selected to be unity. Similarly the operation on wave function is defined: $\Psi(\boldsymbol{r}) \equiv \langle\boldsymbol{r}|\Psi\rangle$, $\mathcal{P}\Psi(\boldsymbol{r}) \equiv \langle\boldsymbol{r}|\mathcal{P}|\Psi\rangle = \langle -\boldsymbol{r}|\Psi\rangle$. Since $\mathcal{P}^2 = 1$ and therefore $\mathcal{P}$ possesses two eigen values, ± 1 and hence 1) even parity ($\Psi_e(\boldsymbol{r}) = \Psi_e(-\boldsymbol{r})$) for any even function 2) odd parity ($\Psi_o(\boldsymbol{r}) = -\Psi_o(-\boldsymbol{r})$) for any odd function.

Now we can look for the action of $\mathcal{T}$ operator. Eventhough the conventional word 'time reversal' is used for this operator, what it actually means is the 'motion reversal' and the time is only a parameter which cannot be directly affected by an operator, and the action of $\mathcal{T}$ and the parameter t can only be connected indirectly. By the definition, the effect of the time reversal operator $\mathcal{T}$ is to reverse the linear and angular momentum while keeping the position unchanged:

$$\begin{aligned} \mathcal{T}\hat{\boldsymbol{r}}\mathcal{T} &= \hat{\boldsymbol{r}}, \\ \mathcal{T}\hat{\boldsymbol{p}}\mathcal{T} &= -\hat{\boldsymbol{p}}, \end{aligned} \tag{1.21}$$

and operation on commutation relation between $\hat{\boldsymbol{r}}$ and $\hat{\boldsymbol{p}}$ gives $\mathcal{T}\imath\mathcal{T}^{-1} = -\imath$, hence $\mathcal{T}$ is antilinear. Following the same convention as in[51] that antilinear operators act only to the right, and never to the left and therefore, not using the adjoint, $A^{\dagger}$, for an antilinear operator. The operation of $\mathcal{T}$ on the Schrödinger equation is necessary for the further discussions, hence,

$$\begin{aligned} &\hat{H}\left|\Psi(t)\right\rangle = \imath\hbar\frac{\partial}{\partial t}\left|\Psi(t)\right\rangle, \\ &\mathcal{T}\hat{H}\mathcal{T}^{-1}\mathcal{T}\left|\Psi(t)\right\rangle = \mathcal{T}\imath\hbar\frac{\partial}{\partial t}\left|\Psi(t)\right\rangle = -\imath\hbar\frac{\partial}{\partial t}\mathcal{T}\left|\Psi(t)\right\rangle. \end{aligned} \tag{1.22}$$

Assume that the Hamiltonian $\hat{H}$ is invariant under time reversal and we do not get any conserved quantity as like in linear transformation. But replacing the dummy parameter t with $-t$ in Eq. 1.22, the solutions of the Schrödinger equation occur in pairs, $\left|\Psi(t)\right\rangle$ and $\mathcal{T}\left|\Psi(-t)\right\rangle$. To get a clear picture, Schrödinger equation in coordinate representation is used,

$$\left[-\frac{\hbar^2}{2m}\nabla^2 + V(r)\right]\Psi(r,t) = \imath\hbar\frac{\partial}{\partial t}\Psi(r,t) \tag{1.23}$$

Its complex conjugate with parameter t replaced with $-t$ is given by,

$$\left[-\frac{\hbar^2}{2m}\nabla^2 + V^*(r)\right]\Psi^*(r,-t) = -\imath\hbar\frac{\partial}{\partial t}\Psi^*(r,-t) \tag{1.24}$$

In order to keep the Hamiltonian invariant under complex conjugation, the potential should satisfy $V(r) = V^*(r)$. Here also, $\Psi(r,t)$ and $\Psi^*(r,-t)$ are the pair of solutions to the Schrödinger equation. Therefore we may identify the time reversal operator with the complex conjugation operator defined by

$$\mathcal{T}\Psi(\boldsymbol{r},t) = \Psi^*(\boldsymbol{r},-t). \tag{1.25}$$

Now we can go to the combined action of $\mathcal{P}$ and $\mathcal{T}$, the $\mathcal{PT}$ operator. The name $\mathcal{PT}$ symmetry linked with the real spectrum of non-Hermitian Hamiltonian was identified first by Bender and Boettcher in 1998[52]. Before entering into how it generalized the postulates of quantum mechanics, its operation on Hamiltonian is given first.

A Hamiltonian $\hat{H}$ is said to be $\mathcal{PT}$ symmetric, when the commutator relation,

$$\left[\mathcal{PT}, \hat{H}\right] = 0, \tag{1.26}$$

holds. The Hamiltonian $\hat{H}$ is $\hat{p}^2/2m + V(\hat{\boldsymbol{r}})$ for a particle in a potential. The action of $\mathcal{PT}$ symmetry on the potential function is given as,

$$\begin{aligned}\mathcal{PT}V(\hat{\boldsymbol{r}}) &= \mathcal{PT}\sum_{n=0}^{\infty} v_n \hat{\boldsymbol{r}}^n = \mathcal{P}\sum_{n=0}^{\infty} v_n^* \hat{\boldsymbol{r}}^n \mathcal{T} = \sum_{n=0}^{\infty} v_n^* (-\hat{\boldsymbol{r}})^n \mathcal{PT} \\ &= V^*(-\hat{\boldsymbol{r}})\mathcal{PT}.\end{aligned} \tag{1.27}$$

To get the condition under which the Hamiltonian to be $\mathcal{PT}$ symmetric, we examine,

$$\mathcal{PT}\hat{H} = \mathcal{PT}\left[\frac{\hat{p}^2}{2m} + V(\hat{\boldsymbol{r}})\right] = \mathcal{P}\left[\frac{\hat{p}^2}{2m} + V^*(\hat{\boldsymbol{r}})\right]\mathcal{T} = \left[\frac{\hat{p}^2}{2m} + V^*(-\hat{\boldsymbol{r}})\right]\mathcal{PT}, \tag{1.28}$$

which will be equal to $\hat{H}\mathcal{PT}$, if the potential satisfies,

$$V(\hat{\boldsymbol{r}}) = V^*(-\hat{\boldsymbol{r}}). \tag{1.29}$$

In terms of real and imaginary parts,

$$\begin{aligned} \Re V(\hat{\boldsymbol{r}}) &= \Re V(-\hat{\boldsymbol{r}}), \\ \operatorname{Im} V(\hat{\boldsymbol{r}}) &= -\operatorname{Im} V(-\hat{\boldsymbol{r}}). \end{aligned} \tag{1.30}$$

Thus the concept of $\mathcal{PT}$ symmetry permits a complex potential in a Hamiltonian such that the real part of the potential must be symmetric and the imaginary part must be antisymmetric with respect to parity operator.

Next we sail through the complex generalization of postulates of quantum mechanics, properties of $\mathcal{PT}$ symmetric systems and the historical developments in the field of $\mathcal{PT}$ symmetry.

Some authors have already mentioned the reality of eigen spectrum for Hamiltonians with singularity[53–56]. Eventhough D. Bessis conjectured[52] the occurrence of real and positive spectrum for Hamiltonian of the form $H = p^2 + x^2 + ix^2$ on the basis of numerical studies, $\mathcal{PT}$ symmetry gets its significance only when it modifies the conventional quantum mechanics[52]. Lots of new kinds of Hamiltonians which are neglected due to the non-Hermicity are considered again with this new concept. What it makes more beautiful is that by replacing the condition of Hermiticity with $\mathcal{PT}$ symmetry, none of the physical properties that a quantum theory possesses are lost.

1.3.1 Features of $\mathcal{PT}$ symmetry

The fundamental axiom in quantum mechanics with the observables ensures the Hermiticity of any operator associated with the measurable quantity(eigen values)[57]. It excludes the possibility of complex Hamiltonians which are necessary to represent many physical situations. The key role of $\mathcal{PT}$ symmetry in quantum mechanics[52] is that it makes certain complex Hamiltonians to possess real energy. How this is possible is discussed below. From Eq.1.30, it is clear that $\mathcal{PT}$ symmetry proposes the possibility

of a complex potential. Due to the complex nature of external potential, the equation of continuity is generalized in the form,

$$\dot{\rho} + \overrightarrow{\nabla} . \overrightarrow{j} = \frac{2\rho}{\hbar} \operatorname{Im} V, \tag{1.31}$$

with ρ, the position probability density and $\overrightarrow{j}$, the probability current density. For real type of potential(Hermitian Hamiltonian), the R.H.S of Eq.1.31 is zero. So, the extra feature that added by the complex potential is that, it gives the system an extra 1) a source if $\operatorname{Im} V$ is positive or 2) sink if $\operatorname{Im} V$ is negative. The imaginary part of a potential is antisymmetric, and hence for every sink there also presents a source in the $\mathcal{PT}$ symmetric potential. These source and sink(gain and loss) work in such way that an equilibrium state is attained(unbroken $\mathcal{PT}$ symmetry) otherwise we can say that the system is in non-equilibrium state(broken $\mathcal{PT}$ symmetry). In simple language[58], PT-symmetric systems can be thought of as non-isolated systems interacting with the environment. This interaction with the environment can be represented by the imaginary part of the complex potential; if the imaginary part is positive, it means that the system gains energy from surrounding otherwise the system loses energy to surroundings. When this give-and-take is balanced, system possesses physical equilibrium otherwise a non-equilibrium state.

Other features of $\mathcal{PT}$ symmetric systems are orthogonality and conservation of norm[59]. By slightly modifying the scalar product, these features can be stated as i) two eigen states $|\psi_1\rangle$ and $|\psi_2\rangle$ belonging to different eigenvalues of a $\mathcal{PT}$ symmetric operator are quasi-orthogonal, $\langle\psi_1|\mathcal{P}|\psi_2\rangle = 0$, ii) norm is conserved with respect to quasi scalar product, $\frac{\partial}{\partial t}\langle\psi(t)|\mathcal{P}|\psi(t)\rangle = 0$. It can also be found that the eigen values of the $\mathcal{PT}$ symmetric systems are a) real for the unbroken $\mathcal{PT}$ symmetry and b) complex eigenvalues(at least one pair) for the broken $\mathcal{PT}$ symmetry. This can be demonstrated as follows; let $|\psi\rangle$ be the eigen state of $\mathcal{PT}$ with

eigen value λ, by using $(\mathcal{PT})^2 = 1$, it can be written as,

$$\begin{aligned} |\psi\rangle = \mathcal{PTPT}\,|\psi\rangle = \mathcal{PT}\lambda\,|\psi\rangle = \lambda^*\mathcal{PT}\,|\psi\rangle = |\lambda|^2\,|\psi\rangle \\ \Rightarrow |\lambda| = 1 \Rightarrow \lambda = \exp(i\varphi), \end{aligned} \tag{1.32}$$

which means the eigenvalue depends on the phase of the eigenfunction because of the antilinearity of $\mathcal{PT}$ operator. Using the Eq.1.26, we can write,

$$\hat{H}\,|\psi\rangle = E\,|\psi\rangle \Leftrightarrow \mathcal{PT}\hat{H}\,|\psi\rangle = \mathcal{PT}E\,|\psi\rangle \Leftrightarrow \hat{H}\mathcal{PT}\,|\psi\rangle = E^*\mathcal{PT}\,|\psi\rangle\,, \tag{1.33}$$

$$\begin{aligned} &\hat{H}\mathcal{PT}\,|\psi\rangle = E^*\mathcal{PT}\,|\psi\rangle \Leftrightarrow \hat{H}\mathcal{PT}\,|\psi\rangle \Leftrightarrow \hat{H}\exp(i\varphi)\,|\psi\rangle = E^*\exp(i\varphi)\,|\psi\rangle\,, \\ &\hat{H}\,|\psi\rangle = E^*\,|\psi\rangle \Rightarrow E = E^*. \end{aligned} \tag{1.34}$$

Hence we can conclude that eigen values are real if $\mathcal{PT}$ symmetry is not broken.

1.3.2 $\mathcal{PT}$ symmetry with nonlinear Hamiltonians

Next we review how $\mathcal{PT}$ operates on nonlinear Hamiltonians of NLSE, GPE etc.[60, 61]. In position representation,

$$\imath\hbar\frac{\partial}{\partial t}\psi(\boldsymbol{r},t) = \left\{\hat{H}_{lin} + f[\psi(\boldsymbol{r},t)]\right\}\psi(\boldsymbol{r},t). \tag{1.35}$$

$\hat{H}_{lin} = \frac{\hat{p}^2}{2m} + V(\hat{\boldsymbol{r}})$ and nonlinear term is represented by $f[\psi]$ which is a functional of ψ. For Gross-Pitaevskii non-linearity, the functional takes the form,

$$f[\psi(\boldsymbol{r},t)] = \int d^3\boldsymbol{r}'\,V_{int}(\boldsymbol{r},\boldsymbol{r}')\left|\psi(\boldsymbol{r}',t)\right|^2. \tag{1.36}$$

These nonlinear Hamiltonian will regain the properties of linear $\mathcal{PT}$ symmetry if it satisfies the conditions $f[\exp(i\varphi)\psi]$=$f[\psi]$, $\varphi\epsilon R$ and $\mathcal{PT}f[\psi] = f[\mathcal{PT}\psi]$. Since the nonlinearity appears as square modulus of the wave

function, it is not changed by an arbitrary phase. And by satisfying the next condition,

$$\begin{aligned}\mathcal{PT}\int d^3\boldsymbol{r}^{'}V_{int}(\boldsymbol{r},\boldsymbol{r}^{'})\left|\psi(\boldsymbol{r}^{'},t)\right|^2 &= \int d^3\boldsymbol{r}^{'}V^{*}_{int}(-\boldsymbol{r},\boldsymbol{r}^{'})\left|\psi(\boldsymbol{r}^{'},t)\right|^2 \\ &= \int d^3\boldsymbol{r}^{'}V^{*}_{int}(-\boldsymbol{r},-\boldsymbol{r}^{'})\left|\psi(-\boldsymbol{r}^{'},t)\right|^2 \\ &\stackrel{!}{=} \int d^3\boldsymbol{r}^{'}V_{int}(\boldsymbol{r},\boldsymbol{r}^{'})\left|\psi(-\boldsymbol{r}^{'},t)\right|^2,\end{aligned} \tag{1.37}$$

where, $\mathcal{P}$ acts only on the $\boldsymbol{r}$ coordinate ($\boldsymbol{r}^{'}$ is an integration variable which is not visible outside the integral) and for the second equality, $\boldsymbol{r}^{'} \rightarrow -\boldsymbol{r}^{'}$ is substituted. Also, we must have $V^{*}_{int}(-\boldsymbol{r},-\boldsymbol{r}^{'})$=$V_{int}(\boldsymbol{r},\boldsymbol{r}^{'})$. It interprets that if the interaction potential is real and it is only determined by the norm of the difference, $|\boldsymbol{r}-\boldsymbol{r}^{'}|$, then such type of potential will fulfill the $\mathcal{PT}$ symmetric conditions. Other potential types, seen in BEC, like monopole interaction[62] and dipole interaction[61, 63, 64] also satisfy these conditions. Hence BEC(i.e., GPE) is a suitable candidate for the $\mathcal{PT}$ symmetric studies.

1.4 Progresses in nonlinear $\mathcal{PT}$ symmetric systems

$\mathcal{PT}$ symmetry becomes useful as 1) it provides a complex generalization of quantum mechanics 2) it follows many properties as like in a conservative linear and nonlinear systems and 3) a possibility to have a control over loss/gain of the system via a complex potential, especially the loss of the system can be engineered in $\mathcal{PT}$ symmetric systems.

$\mathcal{PT}$ symmetry gives real spectrum only for a certain class of non-Hermitian Hamiltonians. i.e., it is a necessary but not a sufficient condition for the reality of the eigen spectrum of non-Hermitian Hamiltonians.

Later in 2002, Mostafazadeh [65, 66] widened the concept of $\mathcal{PT}$ symmetry with pseudo-Hermiticity. Optics became the first fruitful area for the implementation of $\mathcal{PT}$ symmetric concept eventhough the origin was in non-Hermitian quantum mechanics. There are proposals where one can create an optical analogue of $\mathcal{PT}$ symmetric quantum mechanics in structured wave guides[67]. Later, El-Ganainy et al.[68] explored the real connection between PT-symmetric quantum mechanics and optics. This connection is due to the close similarity of the equation describing the paraxial ray of a wave guide and the Schrödinger equation in quantum mechanics. In optics, the gain/loss mechanism is run by complex refractive index of the medium instead of the complex $\mathcal{PT}$ symmetric potential in quantum mechanics. A detailed description of light propagation and $\mathcal{PT}$ symmetry breaking are given in [69]. Soon, these $\mathcal{PT}$ symmetric optical theories were experimentally realized [70–73]. Other areas where intense experimental works done using $\mathcal{PT}$ symmetric concepts are multiple wave guides[74, 75], $\mathcal{PT}$ symmetric microwave cavities[76], $\mathcal{PT}$ symmetric cavity lasers[77], unidirectional invisibility[78, 79], optical whispering gallery resonators[80], $\mathcal{PT}$ symmetric atomic diffusion[81], super conducting wires[82], $\mathcal{PT}$ symmetric electronic circuits[83], NMR[84], Surface plasmon polaritons[85], graphene[86] and metamaterials[87].

As already stated, Bose-Einstein condensate, a true quantum system, is a suitable candidates for $\mathcal{PT}$ symmetric studies. The bright matter wave solitons in $\mathcal{PT}$ symmetric Bose-Einstein condensates are the main focus of this thesis. Below we describe some of the results in $\mathcal{PT}$ symmetric BECs.

1.5 $\mathcal{PT}$ symmetry in BEC

Similar to loss/gain mechanism in $\mathcal{PT}$ symmetric optical wave guides, Klaiman et. al, [69] suggested a similar mechanism can be implemented in Bose-Einstein condensates in which the external trapping potential is in the form of double well, one well acts as particle source and the other is a particle sink. What makes the realization of $\mathcal{PT}$ symmetric BEC crucial is that the interaction in BECs(represented by non-linear terms in GPE) may alter even $\mathcal{PT}$ symmetric properties. Hence the experimental evidence is still lacking eventhough attempts are going on. Next we consider many theoretical proposals in literature which may realize the scenario in future.

The first attempt in this regard which tackles both the nonlinearity and $\mathcal{PT}$ symmetry is the $\mathcal{PT}$ symmetric Bose-Hubbard model[88–90] for a Bose-Einstein condensate in a double well potential. This model gives a good approximation in the mean field limit. Yet another description based on GPE and a δ- type $\mathcal{PT}$ symmetric potential is given by Cartarius et.al., [61, 91]. With vanishing nonlinearity, this model shows all the properties of a $\mathcal{PT}$ symmetric optical wave guide and with nonlinearity, it explains BEC with loss and gain in a double well potential. Hermitian four-well potential has been proposed for the realization of a PT -symmetric system[92] where the tunneling of the outer wells can be used to add and remove particles from the inner wells.

Some of the experimental works which route to the realization of $\mathcal{PT}$ symmetric BEC include optical dipole traps generated by red/blue tuned resonance laser light[93], optical weak link between two spatially separated Bose-Einstein condensates[94], the local interaction of the electron beam with the atomic ensemble by using high resolution scanning electron microscopy[95], a pumped atom laser for replenishing a BEC[96] and controlling the dynamics of an open many-body quantum system with localized dissipation[97].

1.6 Bright matter wave solitons in $\mathcal{PT}$ symmetric systems

The localized solution of an integrable system is usually refereed to as soliton [98]. In a nonlinear medium such as BEC, the interplay between the nonlinearity and dispersion results in the appearance of solitons(localized wavepackets moving without distortion). In BEC, bright or dark solitons can be generated which depend on whether the interaction between atoms is attractive or repulsive. A dark soliton is a localized absence of atoms or depression of the atomic field and it is restricted to propagate in the nonlinear medium(BEC). Bright solitons are condensates itself and have no such restriction on the propagation medium.

The Ecole Normale Superieure group in Paris[99] and another group at Rice University[100] have succeeded in creating bright matter wave solitons in ^7Li condensates using Feshbach resonance. Feshbach resonance is a scattering resonance in which pairs of free atoms are tuned via the Zeeman effect into resonance with a vibrational state of the diatomic molecule[101] and thus provide a continuous variation in scattering length(a) from positive to negative values. The Feshbach resonance provides a continuous knob to vary the atom-atom interaction from repulsive to attractive and from weak to strong.

Solitons supported by various $\mathcal{PT}$-symmetric complex potential are reported in nonlinear lattices[102, 103], dark soliton and vortices[104], Gray soliton[105] and stable bright soliton in defocusing Kerr media[106]. Nonlinear localized modes in PT-symmetric optical media with varying gain-loss[107] and with varying nonlinearity[108] are reported. The role of PT-symmetry on soliton propagation in nonlinear couplers has been investigated in[109–111]. Two dimensional solitons in PT-symmetric periodic[112], nonlocal [113] and inhomogeneous[114] nonlinear media are also studied.

Next, an overview of the analytical and numerical methods used in this thesis is given below.

1.7 Variational approach to dissipative systems

Variational approach is a good analytical approximation method often providing deeper insights into the physics at work. It is based on Ritz's optimization procedure where a trial wave function is selected to match the physical constraints of the investigated system[115, 116]. Variational method has been used to solve some types of nonlinear wave equations[117–119]. The NLSE[120, 121] in nonlinear optics, GPE in the context of BECs[23, 24, 27, 28] are some examples where variational approach gives both qualitative and quantitative results. The main task in this approximation is the selection of a suitable trial function which should match with the real solution of the system in hand otherwise the results obtained may be wrong. Adjusting the variational parameters in the trial function is very important to attain the lowest energy configuration.

Below we are recollecting the variational method which can be used for both conservative and dissipative systems[116, 122]. It's noteworthy that the analytical approach provides approximate solutions when the system involves loss/gain processes. A mathematical formulation of variational approach with dissipative terms is described with help of Rayleigh-Ritz method for NLSE in[122].

The total Lagrangian of the system can be written as,

$$\boldsymbol{L}\left(q, q^*, \xi, \tau, q_\xi, q_\tau, q_\xi^*, q_\tau^*\right) = \boldsymbol{L}_C + \boldsymbol{L}_{NC}, \tag{1.38}$$

where, L_C corresponds to conservative part of the Lagrangian while L_{NC} to the non-conservative part. $q(\xi, \tau)$ is the trial function we chose, that

makes the Lagrangian integral stationary. This corresponds to the amplitude envelope of the optical filed in the realm of optical wave guide or it represents trial function with BEC parameters like width, curvature, centre of mass, etc. q_ξ and q_τ are the partial derivatives of q with respect to ξ and τ respectively.

In Hamilton's principle and there by the Euler-Lagrange equations of motion is given by,

$$\delta\left[\int\int(\boldsymbol{L})\,d\xi d\tau\right]=\delta\left[\int\int(\boldsymbol{L}_C+\boldsymbol{L}_{NC})\,d\xi d\tau\right]=0, \tag{1.39}$$

$$\frac{\delta\boldsymbol{L}}{\delta q_i}=\frac{\partial}{\partial\xi}\frac{\partial\boldsymbol{L}_C}{\partial\left(\frac{\partial q_i}{\partial\xi}\right)}+\frac{\partial}{\partial\tau}\frac{\partial\boldsymbol{L}_C}{\partial\left(\frac{\partial q_i}{\partial\tau}\right)}-\frac{\partial\boldsymbol{L}_C}{\partial q_i}=Q_i, \tag{1.40}$$

where Q_i is responsible for all the dissipative terms in the system and is given by,

$$Q_i=\frac{\partial\boldsymbol{L}_{NC}}{\partial q_i}-\frac{\partial}{\partial\xi}\frac{\partial\boldsymbol{L}_{NC}}{\partial\left(\frac{\partial q_i}{\partial\xi}\right)}-\frac{\partial}{\partial\tau}\frac{\partial\boldsymbol{L}_{NC}}{\partial\left(\frac{\partial q_i}{\partial\tau}\right)}. \tag{1.41}$$

Now we assume the trial function of the following form,

$$q(\xi,\tau)=f(\eta_1(\xi),\eta_2(\xi),.....\eta_N(\xi),\tau)\,, \tag{1.42}$$

which consists of a number of unknown parameter functions $\eta_N(\xi)$ that clearly explains the system behaviors. Now the $\boldsymbol{L}$ will be functions of $\left(\xi,\tau,f,f^*,q_\xi,q_\tau,q_\xi^*,q_\tau^*\right)$. Then the action integral can be written as,

$$I=\int\int\boldsymbol{L}\left(\xi,\tau,f,f^*,q_\xi,q_\tau,q_\xi^*,q_\tau^*\right)d\xi d\tau. \tag{1.43}$$

The extremum of the variation integral I satisfies,

$$\Sigma_{k=1}^{n}\delta\int\int\left(\frac{d}{d\xi}\frac{\partial\boldsymbol{L}_C}{\partial f_\xi}-\frac{\partial\boldsymbol{L}_C}{\partial f}+Q_q(f)\right)\frac{\partial f}{\partial\eta_i}\delta\eta_i d\xi d\tau=0, \tag{1.44}$$

where it is assumed that the only independent variable is ξ. Again, the variational equations in terms of ξ and η_i are given by,

$$\Sigma_{k=1}^{n}\delta\int\int\left(\frac{d}{d\xi}\frac{\partial L_{KC}}{\partial(\eta_i)_\xi}-\frac{\partial L_{KC}}{\partial\eta_i}+Q_K\right)\delta\eta_i d\xi d\tau=0, \tag{1.45}$$

where the subindex K is taken to distinct the Lagrangian and Q before and after substitution of η_i. In terms of reduced Lagrangian $\langle L_{KC}\rangle$, the Euler-Lagrange equations for the variational parameters η_i is,

$$\frac{d}{d\xi}\frac{\partial\langle L_{KC}\rangle}{\partial(\eta_i)_\xi}-\frac{\partial\langle L_{KC}\rangle}{\partial\eta_i}=\int Q_K\frac{\partial q}{\partial\eta_i}d\tau. \tag{1.46}$$

For a conservative system the R.H.S. of the Eq.1.46 is zero. In the case of GPE, ξ and τ are interchanged.

1.8 Linear Stability Analysis(LSA)

In order to get physically observable outcomes of a system, the corresponding theoretical solutions obtained must be stable with respect to perturbations. Hence solutions of non-linear systems are usually checked for the stability. We have done the stability analysis of the stationary solutions using the Bogoliubov-de Gennes(BdG) equations which are obtained by linearizing the GPE(NLSE) by using the Bogoliubov ansatz for elementary excitation [123]. The ansatz is in the form,

$$\psi(\boldsymbol{r},t)=\exp(-i\mu t)\left[\psi_0(\boldsymbol{r})+\Sigma_j\left(p_j(r)\exp(-i\Omega_j t)+q_j(r)\exp(i\Omega_j^* t)\right)\right], \tag{1.47}$$

where, p_j and q_j are complex perturbations which oscillate at frequency $\pm\Omega_j$. Substituting the ansatz, Eq.1.47 in to the GPE given in Eq. 1.10, and keeping only the linear terms in p_j and q_j, we will get a matrix relation

as,

$$\begin{bmatrix} \hat{H}_0 - \mu + 2g\psi_0^2(\boldsymbol{r}) & g\psi_0^2(\boldsymbol{r}) \\ g\psi_0^{*2}(\boldsymbol{r}) & \hat{H}_0 - \mu + 2g\psi_0^2(\boldsymbol{r}) \end{bmatrix} \begin{bmatrix} p_j(\boldsymbol{r}) \\ q_j^*(\boldsymbol{r}) \end{bmatrix} = \begin{bmatrix} \hbar\Omega_j \\ -\hbar\Omega_j \end{bmatrix} \begin{bmatrix} p_j(\boldsymbol{r}) \\ q_j^*(\boldsymbol{r}) \end{bmatrix}, \tag{1.48}$$

with $\hat{H}_0 = -\frac{\hbar^2}{2m}\nabla^2 + V_{ext}(\boldsymbol{r})$. Eq.1.48 is known as Bogoliubov-de Gennes (BdG) equations and it is connected to the stability of the state Φ_0 as,

$$\left(\Omega_j - \Omega_j^*\right) \int \left(\left|p_j^2\right|^2 - \left|q_j^2\right|^2\right) d\boldsymbol{r} = 0. \tag{1.49}$$

We can see that if $\left(\Omega_j - \Omega_j^*\right) = 0$, i.e., if the eigen frequencies Ω_j are real, then the state ψ_0 is stable. For this case, the normalization condition for the eigenmodes p_j and q_j is of the form $\int \left(\left|p_j^2\right|^2 - \left|q_j^2\right|^2\right) d\boldsymbol{r}$=1. If the eigen frequencies are complex, the state ψ_0 is dynamically unstable and Eq.1.49 satisfies only if $\int \left|p_j^2\right|^2 d\boldsymbol{r}$=$\int \left|q_j^2\right|^2 d\boldsymbol{r}$.

1.9 Numerical methods

Different numerical schemes used in the following chapters of this thesis to find stationary solution and dynamics of the system are briefly explained below.

Stationary solutions of GPE, Eq.1.10 are sought using standard relaxation technique based on pseudospectral differentiation with Fourier differentiation of matrices [124]. This method is successful in solving problems arising in many areas of science[125, 126] due to its spatially spectral accuracy. Spectral methods are powerful methods used for solving the partial differential equations. Unlike the finite difference methods, spectral methods are global methods, where the computation at any given point

depends not only on the information at neighboring points, but also on the information from the entire domain. Spectral methods are converged exponentially, which makes them more accurate than local methods. To find the stationary solution, first we convert the differential eigenvalue problem to a matrix eigenvalue problem. Then the standard relaxation technique is used: i.e., begin with an initial guess for the solution x_0 to the matrix equation $Ax = b$ and iterate until the updated solution x_k that is close to the exact solution within some pre-specified error tolerance ($|b - Ax_k| <$ error tolerance($e.g., \sim 10^{-6}$)). Hence the stationary solutions of GPE can be found as explained below. Eq.1.13 is expressed in dimensionless 1-D form as,

$$\mu\psi = -\frac{1}{2}\frac{\partial^2\psi}{\partial x^2} + (V_R + iV_I)\psi - |\psi|^2\,\psi, \tag{1.50}$$

where, $V_{ext}(r)$ is expressed in complex form to include the notion of $\mathcal{PT}$ symmetry. Let $\psi = u + \imath v$ be the initial guess for the solution and substituting in Eq.1.50 and we have obtained after separating real and imaginary parts,

$$\mu u = -\frac{1}{2}\frac{\partial^2 u}{\partial x^2} + V_R u - V_I v - (u^2 + v^2)u, \tag{1.51}$$

$$\mu v = -\frac{1}{2}\frac{\partial^2 v}{\partial x^2} + V_R v + V_I u - (u^2 + v^2)v. \tag{1.52}$$

The new assumed solution after one iteration will be $u = u + \Delta u$ and $v = v + \Delta v$. To get Δu and Δv, substitute first, the perturbed form of solution as $u = u + \Delta u$ and $v = v + \Delta v$ in Eq.1.51 and in Eq.1.52, we have obtained the equations in matrix form as(higher order terms in delta are neglected),

$$P \begin{bmatrix} \Delta u \\ \Delta v \end{bmatrix} = Q \begin{bmatrix} u \\ v \end{bmatrix} \tag{1.53}$$

with matrices P and Q are given by,

$$\begin{bmatrix} \frac{1}{2}\frac{d^2}{dx^2} + (u^2+v^2) + \mu - V_R + 2u^2 & 2uv + V_I \\ 2uv - V_I & \frac{1}{2}\frac{d^2}{dx^2} + (u^2+v^2) + \mu - V_R + 2v^2 \end{bmatrix} \tag{1.54}$$

and

$$\begin{bmatrix} -\frac{1}{2}\frac{d^2}{dx^2} - (u^2+v^2) - \mu + V_R & -V_I \\ V_I & \frac{-1}{2}\frac{d^2}{dx^2} - (u^2+v^2) - \mu + V_R \end{bmatrix}. \tag{1.55}$$

Now we can write,

$$\begin{bmatrix} \Delta u \\ \Delta v \end{bmatrix} = P^{-1}Q \begin{bmatrix} u \\ v \end{bmatrix}. \tag{1.56}$$

The iteration will be continued till the new solution which closes to the exact solution(within the specified error tolerance) is obtained.

For the dynamical evolution, we numerically solve Eq.1.10 using the operator splitting technique. For the generic evolution equation,

$$u_t = \hat{A}u + \hat{B}u, \tag{1.57}$$

the solution $u(t+\Delta t)$ at time $t+\Delta t$ can be computed starting from $u(t)$ by using different splitting methods. In our case operators $\hat{A}$ and $\hat{B}$ correspond to the diffusion term and to the overall effective potential, V_{eff}. For the diffusion term, the Crank-Nicolson scheme was utilized. According to the chosen splitting method, the solution can be obtained as:

Lee: $$u(t+\Delta t) = e^{\Delta t\hat{A}}e^{\Delta t\hat{B}}u(t), \tag{1.58}$$

Strang: $$u(t+\Delta t) = e^{0.5\Delta t\hat{A}}e^{\Delta t\hat{B}}e^{0.5\Delta t\hat{A}}u(t), \tag{1.59}$$

SWSS: $$u(t+\Delta t) = \frac{1}{2}(e^{\Delta t\hat{A}}e^{\Delta t\hat{B}} + e^{\Delta t\hat{B}}e^{\Delta t\hat{A}})u(t). \tag{1.60}$$

Due to the non-Hermitian nature of the system, numerical convergence strongly depends on the underlying operator splitting method used. For a

conservative system(as well as the $\mathcal{PT}$ symmetric system below $\mathcal{PT}$ breaking point), a simple Lee splitting with a first order accuracy is sufficient to achieve numerical convergence. In our case the dynamics of the condensate requires the symmetrically weighted sequential splitting(SWSS), which is second order accurate. We also employed the Strang method, encompassing a second order accuracy as well. Nonetheless, the Strang method fails for V_i values close to the exceptional point.

1.10 Outline of the thesis

In this thesis we have studied the consequences of interplay between the nonlinearity (originating from the interatomic interactions) and $\mathcal{PT}$ symmetry(gain and loss mechanism) in BEC. We look for localized solutions(matter wave bright solitons) of the Gross-Pitaevskii equation (GPE) with trapping potential chosen in complex form to account for the gain and loss effects in a $\mathcal{PT}$-symmetric system. The thesis is organized into six chapters: An introductory remarks on $\mathcal{PT}$ symmetry and BEC are given in chapter 1. Behavior of the matter wave bright solitons in BEC with a competing attractive nonlinearity and $\mathcal{PT}$ symmetry are discussed in chapter 2. We have checked the non-reciprocal behavior shown by BEC trapped in 1-D super-Gaussian $\mathcal{PT}$ symmetric potential in chapter 3. A competing repulsive nonlinearity with $\mathcal{PT}$ symmetry is dealt in chapter 4. Dynamics of BEC with $\mathcal{PT}$ symmetry beyond mean field theory are discussed in chapter 5 and finally concluded in chapter 6.

2

Existence, stability and dynamics of $\mathcal{PT}$ symmetric bright soliton in an attractive BEC

Non-Hermitian $\mathcal{PT}$ symmetric Hamiltonians are useful to describe the gain and loss mechanisms in open quantum systems[127] like Bose-Einstein Condensates(BEC) as presented in chapter 1. Hence the non-Hermitian description of the Gross-Pitaevskii equation is expected to provide interesting outcomes concerning basic physical principles. In this chapter, how the gain/losss mechanism affects the existence, stability and dynamics of matter wave bright solitons in BEC trapped in a $\mathcal{PT}$ symmetric potential is investigated. Optical solitons in nonlinear optical media and matter wave solitons existing in dilute BEC, share the same main features due to the mathematical equivalence between the nonlinear Schrödinger equation, describing nonlinear light propagation, and the GPE, describing quantum phases of matter[99, 100]. In both cases, the nonlinearity stems from many-body interactions which are neglected in the linear models. In contrast to optics, experimental realizations of $\mathcal{PT}$-symmetric quantum systems are lacking, but there are considerable theoretical proposals[92, 128–130]. Different types of complex $\mathcal{PT}$ symmetric potentials used in BECs are already mentioned in chapter 1 and in this thesis, the fundamental

single peak $\mathcal{PT}$-symmetric soliton supported by a single well potential is considered.

The present chapter deals with the $\mathcal{PT}$-symmetric matter wave solitons in a reduced 1D setting, where the BEC is harmonically trapped in two spatial dimensions, whereas in the third spatial direction a super-Gaussian potential acts on the matter wave. Family of super-Gaussian profiles have been chosen which allows in varying the shape of the trapping potential from a Gaussian to a square-well, thus helping to address the role played by the steepness of the potential on the confinement of the condensate. Furthermore, it is assumed that the BEC interacts with the local environment by adding an imaginary component on the potential profile, accounting phenomenologically for gain and loss in the system. The condition which has to hold true to get $\mathcal{PT}$-symmetry is that the imaginary part of the complex potential has to be anti-symmetric, i.e, losses in the trap should be compensated by the gain in the trap. Previous works on $\mathcal{PT}$-symmetric solitons concentrated on potentials with fixed profile for imaginary potential(gain/loss mechanism), considering only changes in the amplitude of the potential[131].

To account for the gain/loss mechanisms, two kinds of transverse profile for the imaginary potential are considered in the present thesis: 1) the imaginary part of the potential is taken as the first derivative of the real part of the potential and 2) an imaginary potential which is given by the real profile multiplied by a first degree polynomial, thus slightly varying with the profile of the real part of the potential. The form of the potential and its purpose in the study are detailed in the next section.

To experimentally implement gain/loss mechanisms in a BEC trapped in a single well potential, a pumping scheme similar to the one implemented in atom lasers[96] can be exploited as well as optical dipole traps, suitably adjusting the detuning to red or blue [132]. The loss mechanisms

can also be implemented by shining the BEC with electron beams[97]. Manipulation of atoms could also be achieved using state-dependent potentials [133] as well as multi-well systems[134, 135].

Both variational and numerical analysis have been used to find the properties of the system trapped in super-Gaussian $\mathcal{PT}$ symmetric potential and it is demonstrated that variational results are in good agreement with numerical simulations of the GPE.

In the following sections, the problem is stated and solutions in the linear and nonlinear cases are obtained and the stability and dynamics of the solutions are checked. Finally, the results obtained by variational and numerical methods are compared.

2.1 Governing equation and dimensional reduction

In the mean field approximation, the condensate wave function $\Phi(\mathbf{R}, T)$ obeys the Gross-Pitaevskii equation given by,

$$i\hbar\frac{\partial\Phi}{\partial T} = -\frac{\hbar^2}{2m}\nabla^2\Phi + g\left|\Phi\right|^2\Phi + V_{ext}(\mathbf{R})\Phi, \tag{2.1}$$

with m the atomic mass, $\hbar$ the Planck's constant, $g = 4\pi\hbar^2 a/m$, a the scattering length, V_{ext} the trapping potential and $\mathbf{R} = (X, Y, Z)$ is the spatial coordinate. Eq.2.1 is valid under the condition that (i) both thermal and quantum depletions are fully accounted by the imaginary part of the potential V_{ext}(in other words, the number of particles $N_0 = \int |\Phi|^2 d^3\mathbf{R}$ is constant in time if $\mathrm{Im}\,(V_{ext}) = 0$) and (ii) phenomena investigated using Eq.2.1 should take place over distances larger than the scattering length a(i.e., the dilute limit case). Assuming that the condensate is harmonically trapped in the Y and Z directions and with an axial trap potential $U(X)$ in the X direction, the external trapping potential can be written

as $V_{ext} = \frac{1}{2}mw_\perp^2(Y^2+Z^2)+U(X)$, with $w_\perp$ being the frequency of atomic oscillations in the radial direction.

For a cigar shaped condensate, i.e., if the density along the X direction, $n_x = \int_{-\infty}^{\infty}|\Phi|^2 dYdZ$, is such that $|a|n_x \ll 1$ ($w_\perp \gg w_x$), the full 3D GPE equation can be reduced to a monodimensional geometry by making the ansatz [136],

$$\Phi(X,Y,Z,T) = \sigma(X,T)\chi(Y,Z), \tag{2.2}$$

$$\chi(Y,Z) = \frac{1}{a_\perp\sqrt{\pi}}\exp\left(-\frac{Y^2+Z^2}{2a_\perp^2}\right), \tag{2.3}$$

with $a_\perp = \sqrt{\frac{\hbar}{mw_\perp}}$. Substitution of Eq.2.2 into Eq.2.1 provides

$$\begin{aligned} i\hbar\frac{\partial\sigma}{\partial T}\chi = &-\frac{\hbar^2}{2m}\frac{\partial^2\sigma}{\partial X^2}\chi - \frac{\hbar^2}{2m}\sigma\Big(\frac{\partial^2\chi}{\partial Y^2}+\frac{\partial^2\chi}{\partial Z^2}\Big) \\ &+ g|\sigma|^2\sigma|\chi|^2\chi + \Big[\frac{1}{2}mw_\perp^2(Y^2+Z^2)+U(X)\Big]\sigma\chi. \end{aligned} \tag{2.4}$$

Multiplying both sides by χ^* and integrating across the whole YZ plane, Eq.2.4 can be recast as,

$$\begin{aligned} i\hbar\frac{\partial\sigma}{\partial T} = -\frac{\hbar^2}{2m}\frac{\partial^2\sigma}{\partial X^2} + \left(g\int\int|\chi|^4 dYdZ\right)|\sigma|^2\sigma \\ +\Big[C+U(X)\Big]\sigma, \end{aligned} \tag{2.5}$$

where,

$$C = \frac{\hbar^2}{2m}\int_{-\infty}^{\infty}\left(\left|\frac{\partial\chi}{\partial Y}\right|^2+\left|\frac{\partial\chi}{\partial Z}\right|^2\right)dYdZ + \int_{-\infty}^{\infty}\frac{1}{2}mw_\perp^2(Y^2+Z^2)|\chi|^2 dYdZ.$$

Given that the constant, C does not depend either on time and X, posing $\sigma = \psi\exp(-iCt)$ Eq.2.5 becomes the 1D GPE,

$$i\hbar\frac{\partial\psi}{\partial T} = -\frac{\hbar^2}{2m}\frac{\partial^2\psi}{\partial X^2} + \beta|\psi|^2\psi + U(X)\psi, \tag{2.6}$$

with $\beta = g\int\int |\chi|^4 dY dZ = \frac{g}{2\pi a_\perp^2}$. The above 1D reduction is valid, if the condensate is strongly confined in the radial direction[100]. Specifically, a dimensionality cross-over constant(from 3D to 1D) $D_{co} = N_0 a w_x/a_\perp w_\perp$ can be defined such that if $D_{co} \ll 1$, the dynamics of the condensate can be described by Eq.2.6[137, 138]. As we are interested in self-focusing nonlinearity, we consider a negative scattering length resulting in attractive interactions between the particles; moreover, we normalize Eq.2.6 using the dimensionless variables $t = Tw_\perp$, $x = X/a_\perp$, $U(X) = V(x)\hbar w_\perp$ and $\psi = u/\sqrt{2a}$, obtaining,

$$i\frac{\partial u}{\partial t} = -\frac{1}{2}\frac{\partial^2 u}{\partial x^2} - |u|^2 u + V(x)u. \tag{2.7}$$

In Eq.2.7 we take $V(x)$ to be complex-valued and $\mathcal{PT}$-symmetric, i.e., possessing a symmetric real part and an anti-symmetric imaginary part so that the potential obeys the necessary(but not sufficient) condition for possessing real eigenvalues. The potential now reads $V(x) = V_R(x) + iV_I(x)$. The real part of the trapping potential is chosen to be of super-Gaussian form, i.e,

$$V_R = -V_r \exp\left(-x^{2l}\right) \ (l = 1, 2, \ldots). \tag{2.8}$$

Increasing l permits to span from a Gaussian-shaped trap($l = 1$) to a rectangular trap($l \gg 1$), thus allowing to address the role played by the abruptness of the trapping potential. The imaginary part of the potential is chosen in order to enable a complete understanding about the flux of particles associated with $\mathcal{PT}$ potentials. For this purpose, two different transverse profiles are chosen: type A encompassing,

$$V_I^A(x) = -V_i x^{2l-1} \exp(-x^{2l}), \tag{2.9}$$

where the gain/loss profile is given by the first derivative of $V_R(x)$, irrespective of the value assumed by the parameter l; type B encompassing,

$$V_I^B(x) = -V_i x \exp(-x^{2l}), \tag{2.10}$$

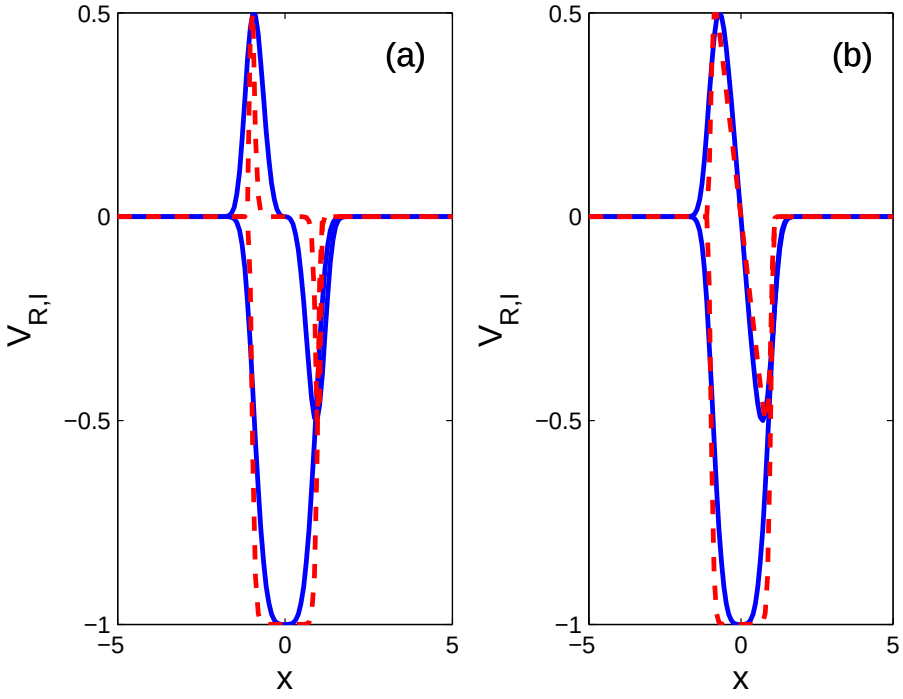

Figure 2.1: Sketch of the transverse profiles of the real and imaginary part of the potential for (a) potential A and (b) potential B for $l = 2$(solid lines) and $l = 8$ (dashed lines) showing how the imaginary part varies. It is to be noted that for $l = 1$ both the potentials are equivalent.

where the profile $V_I(x)$ now is a super-Gaussian multiplied by x. Fig.2.1 depicts both kinds of potentials together with their real part: the gain/loss distribution for type A tends to become sharply peaked as l is increased whereas V_I slightly changes with l for type B, conserving indeed a smoother profile as l grows up. The total number of particles $N = \int_{-\infty}^{\infty} |u|^2 \, dx$ in the normalized frame is related to the actual number of particles N_0 by $N = \int_{-\infty}^{\infty} |u|^2 \, dx = 2aN_0/a_\perp$. To be concrete, taking the parameters of quasi-1D ^7Li condensate consisting of $N_0 = 6000$ atoms, experimentally demonstrated in[100], with $a = -3a_B$(a_B is the Bohr radius), we obtain $a_\perp = 0.3\mu m$, $N \approx 6$ and $D_{co} = 0.025 \leq 1$ for $w_x/w_\perp = 1/100$.

Now, we can find the stationary solutions of Eq.2.7 in the linear and nonlinear cases separately.

2.2 Stationary solutions in the linear case

Before dealing with the nonlinear case, the existence and the behavior of confined modes in the linear case are studied in this section. Bound states can be found numerically from Eq.2.7 making the ansatz $u(x,t) = \phi(x)e^{-i\mu t}$, providing the linear eigenvalue problem $\mu\phi = -\frac{1}{2}\frac{\partial^2\phi}{\partial x^2} + (V_R + iV_I)\phi$. Due to the presence of dissipative terms, eigenvalue μ in general will be complex, that is, we can write $\mu = \mu_R + i\mu_I$. Now we have solved numerically the equation to get the ground state with V_r fixed at $V_r = 1$. Fig.2.2 and Fig.2.3 show that eigenvalues of the system follow an analogous behavior as the gain/loss magnitude V_i is changed. In fact, for V_i lower than a critical value, V_c, $\mathcal{PT}$-symmetry is conserved and all the eigenvalues are real. The eigenmode has a symmetric real and anti-symmetric imaginary part(Fig.2.2 last row last column). Condition $V_i = V_c$ identifies the exceptional point where $\mathcal{PT}$-symmetry is spontaneously broken: the eigenvalues corresponding to the maximum μ_R becomes complex, thus

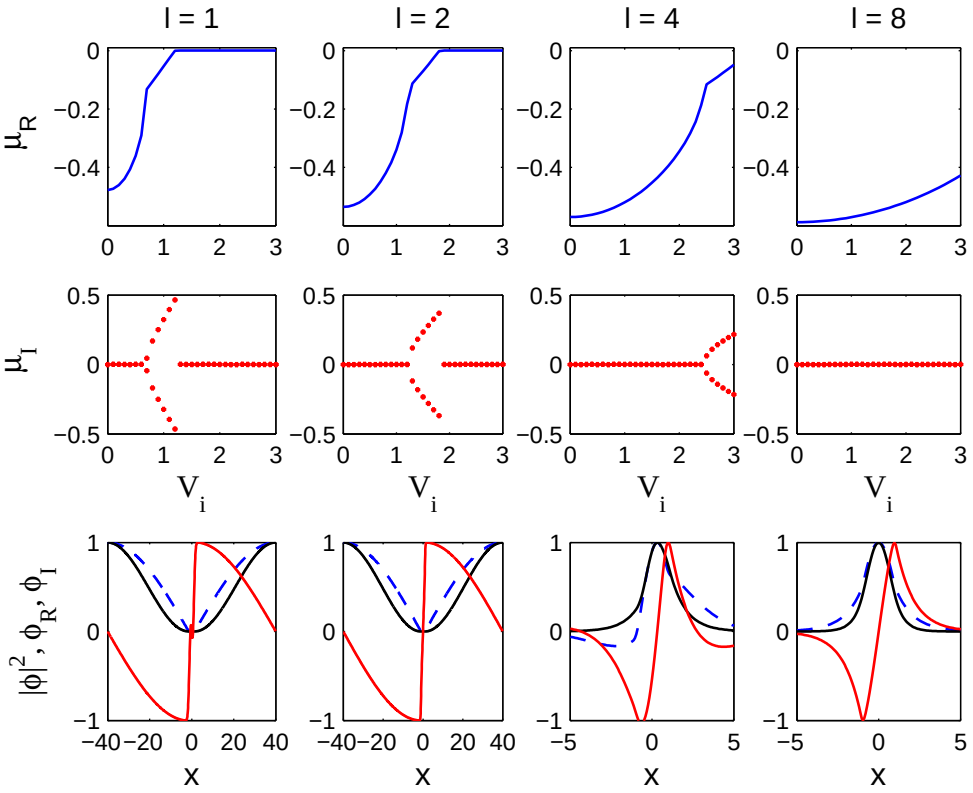

Figure 2.2: Ground state μ vs V_i for the potential of type A. Top row depicts real part μ_R and middle row depicts imaginary part μ_I, plotted versus V_i. Imaginary eigenvalues with equal magnitude but opposite in sign appear at the exceptional point. The stationary profiles at $V_i = 3$, which falls in different spectral region for each l, is plotted in the last row; black symmetric solid line is the intensity, blue dashed line is the real part of ϕ and finally the antisymmetric red solid line is the imaginary part of the field ϕ. Here $V_r = 1$.

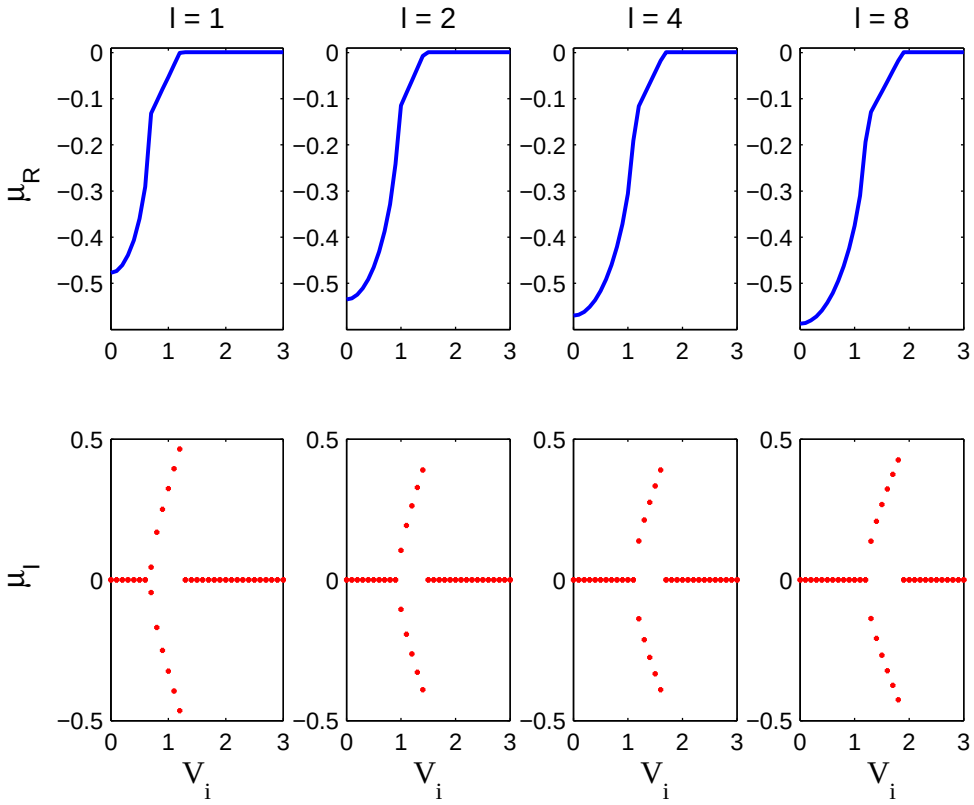

Figure 2.3: Ground state μ vs V_i for the potential of type B. Top row depicts real part μ_R and the bottom row depicts imaginary part μ_I, plotted versus V_i. As compared to type A, trend of the eigenvalue μ_I versus V_i depends much less on l given that $V_I(x)$ is kept constant. Here $V_r = 1$.

the corresponding eigenmodes are subjected to an exponential decay or amplification, according to the sign of the imaginary part of μ. The real part of the eigenmode now becomes asymmetric(an example is shown in Fig.2.2 last row third column). Further increase in V_i induce an almost linear growth for $|\mu_I|$; μ_R follows a raising quasi-linear trend with V_i as well. This trend is abruptly interrupted for a certain threshold value, V_t, after that both the μ_R and μ_I vanish. At this point the eigenvalues are in the continuum and the corresponding eigenmodes are spread in space(Fig.2.2 last row first two columns; size of the numerical grid is [-40 40] with solutions required to vanish at the boundary.)

The dynamics described above is shared by both the types of imaginary potentials V_I described by Eqs.2.9 and 2.10. For potentials of type A(Eq.(2.9)) the critical potential is $V_c^A \approx lV_r/2+1/5$(i.e., linearly increase with l) and follows more or less the trend for analytically solvable complex Scarf II potential[139], thus providing $V_c \approx 0.7$ for $l = 1$, $V_c \approx 1.2$ for $l = 2$, $V_c \approx 2.2$ for $l = 4$, and $V_c \approx 4.2$ for $l = 8$. For the type B(Eq.2.10), the transition occurs at $V_c^B \geq V_r$ for $l \geq 2$($l = 1$ is analogous to type A), then undergoing small increases as l gets larger. The threshold potential V_t follows an analogous trend, the increase with V_i being larger for potentials of type A.

The complex nature of the potential impacts deeply on the nature of the stationary solutions. In the presence of a complex potential the behavior of V_c and V_t can be understood by invoking the particle conservation on each point of the transverse plane. The particle conservation for the Schrödinger equation reads,

$$\overrightarrow{\nabla} \cdot \overrightarrow{j} = -\frac{\partial \rho}{\partial t} + 2V_i(x)\rho, \tag{2.11}$$

where $\rho = |\phi|^2$ is the particle intensity and the particle flux j is given by $j = \frac{1}{2i}\left(u^*\frac{\partial u}{\partial x} - u\frac{\partial u^*}{\partial x}\right)$. Setting $\phi = \sqrt{\rho}e^{i\xi(x)}$, the flux reads, $j = \rho\frac{\partial \xi}{\partial x}$. For

stationary modes, $\partial\rho/\partial t = 0$ holds valid. Thus, Eq.2.11 implies [140],

$$\frac{\partial}{\partial x}\left(\rho\frac{\partial\xi}{\partial x}\right) = 2V_i(x)\rho. \tag{2.12}$$

Eq.2.12 tells us that the eigenmodes feature a non-flat phase profile on the transverse plane x, the latter corresponding to a net motion of particles from the gain to loss regions, as required to conserve the overall particle number in the presence of V_i[141]. According to Eq.2.12, an even ρ corresponds to an odd ξ, that is, an even real part and an odd imaginary part, respectively. Physically, particles are created within the gain region and then they diffuse towards the loss region in order to keep the overall(i.e., integrated along x) particle number $\int n_x dx$ constant. It is to be noted that the flux j is an even function, that is, a unidirectional flow takes place when the real part of ϕ is even[141]. Eq.2.12 also states that larger the V_i, larger the anti-symmetric component of the wave function is. Physically, the transverse flux must be larger in order to compensate the inhomogeneous gain/loss.

2.3 Stationary solutions in the nonlinear case

Let us now discuss the nonlinear case. In full analogy with the linear case, solitonic solutions of Eq.2.7 are in the form $u(x,t) = \phi(x)\exp(-i\mu t)$, μ being the chemical potential. Due to the non-linear term both $\phi(x)$ and μ depends on the number of particles N, defined in the dimensionless framework as $N = \int |\psi|^2 dx$. Substituting for $u(x,t)$, Eq.2.7 turns into,

$$\mu\phi = -\frac{1}{2}\frac{\partial^2\phi}{\partial x^2} + (V_R + iV_I)\phi - |\phi|^2\phi. \tag{2.13}$$

Stationary solutions of Eq.2.13 are sought using standard relaxation technique based on pseudo-spectral differentiation with Fourier differentiation matrices[124]. We look for stationary solutions for different l and V_I values

keeping the amplitude of real part V_r fixed (V_r=1). The most striking effects ascribable to the nonlinearity is the *generation* of a nonlinear bound state featuring $\mu_R < 0$ and $\mu_I = 0$, regardless of the magnitude of V_i (i.e., even above the exceptional point). Differently stated, the nonlinearity provokes a transition from broken $\mathcal{PT}$ to a $\mathcal{PT}$-symmetric state[140–142], even if all the linear eigenvalues are complex. An overview of the features of the fundamental soliton showing the minimum μ_R for varying V_i and l is shown in Fig.2.4.

Typical profiles of the shape-invariant solutions for potentials of type A are depicted in Fig.2.5 and for potentials of type B in Fig.2.6. In both the figures soliton transverse profiles for fixed values of the eigenvalue μ are plotted. In accordance with Eq.2.12, the fundamental soliton has an even real part and an odd imaginary part[106, 131, 140, 141].

Let us now discuss the soliton properties depending on the shape of the potential, starting from type A. For $V_i = 0.5$ soliton profiles are slightly perturbed by the small transverse flux(Eq.2.12), whatever the values of μ and the degree l are. Increasing the magnitude of V_i, profiles of ϕ are affected by the dissipative terms when μ is small, corresponding to wide solitons strongly overlapping with the gain/loss regions. To minimize the spatial overlap between the intensity distribution and the gain/loss regions, solitons get narrower as V_i increases(third column in Fig.2.5). In agreement with this interpretation, this effect disappears as l is increased. Solitons propagating in type B potentials confirm our interpretation. In fact, regardless of the shape of V_R (i.e., independently from l), solitons get narrower as V_i is raised up, given that the spatial shape of V_I does not vary appreciably with l.

Now, Eq.2.7 is solved using variational method and the results obtained are compared with that found from numerical methods.

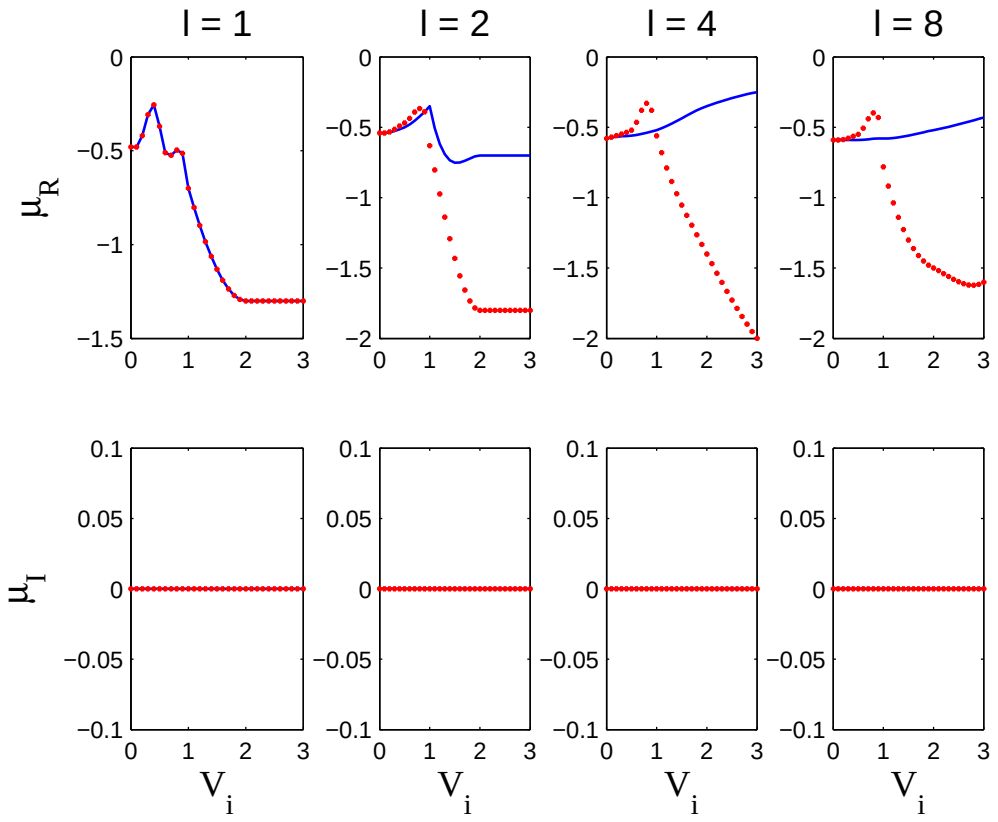

Figure 2.4: Features of the fundamental soliton vs V_i for the lowest μ_R allowed, both for potentials of type A (blue solid lines) and type B (red points). The two rows depict real part μ_R and the imaginary part μ_I respectively.

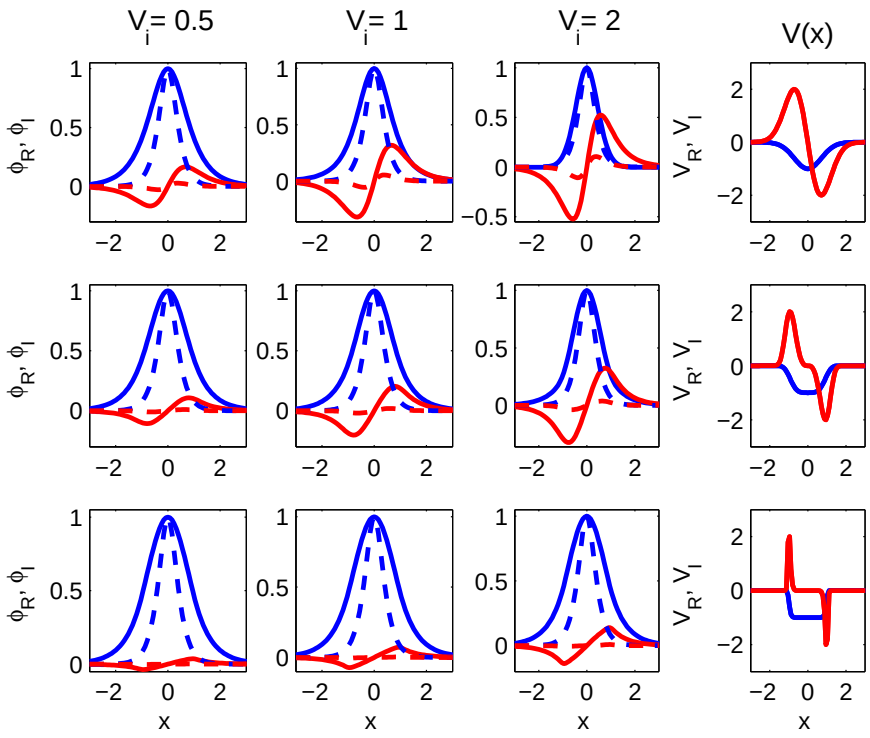

Figure 2.5: Soliton profiles for potentials of type A for $l = 1$, 2, and 8 (top to bottom rows) for V_i as marked. Symmetric solid curves represent the normalized real part of the profile for $\mu = 1.3$ (solid lines) and $\mu = 6$ (dashed lines). Antisymmetric curves represent the imaginary part normalized to the peak of the real part; higher the magnitude lower the μ. The behavior of V_R (blue symmetric lines) and V_I (red antisymmetric lines) versus x are shown in the last column for each l for $V_i = 2$.

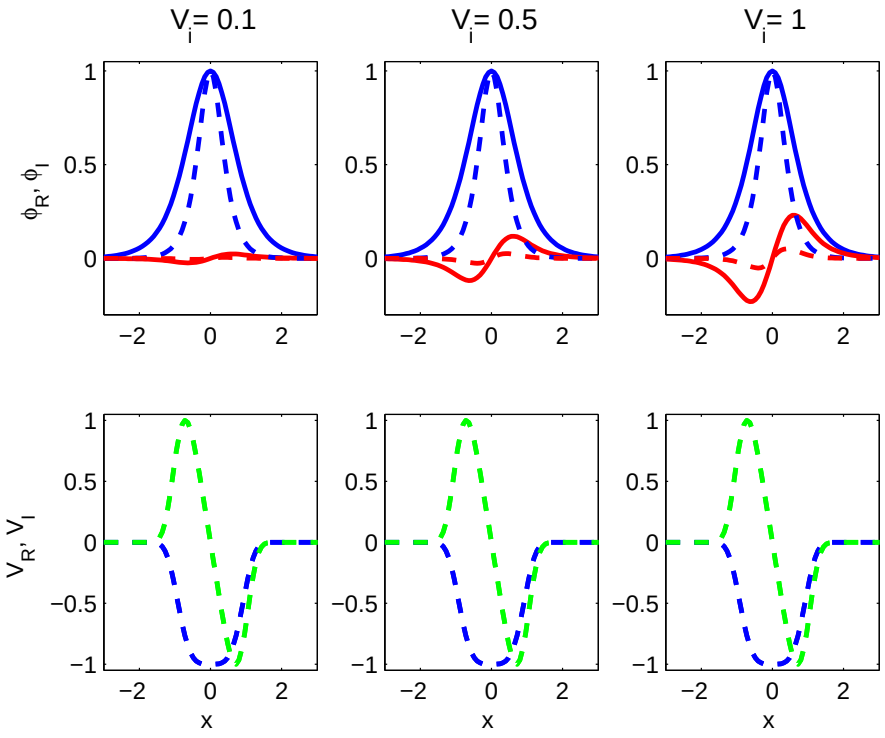

Figure 2.6: Soliton profiles for potentials of type B for $l = 2$ (other values of l provide almost identical results), for V_i as marked. Symmetric blue curves represent the normalized real part of the profile for $\mu = 1.8$ (solid lines) and $\mu = 6$ (dashed dotted lines). Solid red lines are the imaginary component of the field normalized with respect to the peak of the real part: the higher the magnitude the lower μ is. In the bottom row, symmetric dashed blue lines represent the real part of the potential. Antisymmetric dashed green line represents the imaginary part of the potential.

2.4 Variational approach

The variational method has been widely used to obtain solutions for nonlinear waves obeying the GPE (or, equivalently, the NLSE). In fact, the method provides closed form solutions in qualitative(or quantitative) agreement with the actual dynamical behavior. It also ensures a deeper insight on the underlying physics. In order to adopt it in the presence of $\mathcal{PT}$-symmetry, we use the variational approach developed for dissipative systems[140, 143, 144]. Making the ansatz $u(x,t) = \phi(x,t)\exp(-i\mu t)$, Eq.2.7 can be recast as,

$$i\frac{\partial\phi}{\partial t} + \mu\phi + \frac{1}{2}\frac{\partial^2\phi}{\partial x^2} + |\phi|^2\phi + V_r\exp(-x^{2l})\phi = iV_I\phi. \tag{2.14}$$

The Lagrangian for the conservative part, corresponding to the left hand side(LHS) of Eq.2.14, is

$$\begin{aligned} L_c =& \frac{i}{2}\left(\frac{\partial\phi^*}{\partial t}\phi - \frac{\partial\phi}{\partial t}\phi^*\right) - \mu|\phi|^2 + \frac{1}{2}\left|\frac{\partial\phi}{\partial x}\right|^2 \\ & - V_r\exp(-x^{2l})|\phi|^2 - \frac{1}{2}|\phi|^4, \end{aligned} \tag{2.15}$$

for both type A and B potentials.

We assume a trial solution such that it accounts for the non-zero phase associated with $\mathcal{PT}$-symmetric stationary states as,

$$\phi(x,t) = A(t)\exp\left(-\frac{x^2}{\omega_b^2}\right)\exp[i\theta f(x)], \tag{2.16}$$

where $A(t)$ corresponds to the wave amplitude supposed to be real, w_b is the width of the soliton, θ is the amplitude of the phase profile and $f(x)$ is the phase distribution along x(in other words we set $\xi = \theta f(x)$, $f(x)$ being a conveniently chosen normalized function so that the overall phase jump across the soliton is equal to θ). Since the real part of the solution is symmetric and the imaginary part is antisymmetric, $f(x)$ can

be assumed to be an odd function of x. The particle number of the solution is defined as $N = \int_{-\infty}^{\infty} |\phi|^2 \, dx = \sqrt{\frac{\pi}{2}} A^2 \omega_b = 2aN_0/a_\perp$. Inserting Eq.2.16 into Eq.2.15 yields the following Lagrangian,

$$\begin{aligned} L_c = & -\mu A^2 \exp\left(-\frac{2x^2}{\omega_b^2}\right) + \frac{A^2}{2} \exp\left(-\frac{2x^2}{\omega_b^2}\right) \theta^2 \left(\frac{df(x)}{dx}\right)^2 \\ & + \frac{2x^2}{\omega_b^4} A^2 \exp\left(-\frac{2x^2}{\omega_b^2}\right) - V_r \exp(-x^{2l}) A^2 \exp\left(-\frac{2x^2}{\omega_b^2}\right) \\ & - \frac{1}{2} A^4 \exp\left(-\frac{4x^2}{\omega_b^2}\right). \end{aligned} \tag{2.17}$$

Integrating Eq.2.15 across the whole x axis provides the reduced Lagrangian, $\langle L_c \rangle = \int_{-\infty}^{+\infty} L_c dx$. From Eq.2.17 we find

$$\begin{aligned} \langle L_c \rangle = & -\frac{\mu A^2 \sqrt{\pi} \omega_b}{\sqrt{2}} \\ & + \frac{1}{2} A^2 \theta^2 \int_{-\infty}^{+\infty} \left(\frac{df(x)}{dx}\right)^2 \exp\left(-\frac{2x^2}{\omega_b^2}\right) dx \\ & + \frac{2}{\omega_b^4} \frac{A^2 \sqrt{\pi} \omega_b^3}{4\sqrt{2}} - V_r A^2 \int_{-\infty}^{+\infty} \exp\left(-x^{2l}\right) \exp\left(-\frac{2x^2}{\omega_b^2}\right) dx \\ & - \frac{1}{2} A^4 \frac{\sqrt{\pi}}{2} \omega_b. \end{aligned} \tag{2.18}$$

Eq.2.18 can be further simplified and rewritten in terms of the particle

number N, yielding,

$$\begin{aligned}\langle L_c\rangle = &-\mu N + \frac{\sqrt{2}N\theta^2}{\sqrt{\pi}\omega_b}\int_0^\infty \left(\frac{df(x)}{dx}\right)^2 \exp\left(-\frac{2x^2}{\omega_b^2}\right)dx \\ &+ \frac{N}{2\omega_b^2} - \frac{2\sqrt{2}V_r N}{\sqrt{\pi}\omega_b}\int_0^\infty \exp(-x^{2l})\exp\left(-\frac{2x^2}{\omega_b^2}\right)dx \\ &- \frac{N^2}{2\sqrt{\pi}\omega_b}.\end{aligned} \tag{2.19}$$

The last term on the RHS of Eq.2.19 depends on the square of the particle number N, denoting its nonlinear origin stemming from two-body interactions. The standard variational approach for systems with dissipative terms can be modified as[143, 144],

$$\frac{d}{dt}\left(\frac{\partial\langle L_c\rangle}{\partial\varphi_t}\right) - \frac{\partial\langle L_c\rangle}{\partial\varphi} = 2\mathrm{Re}\int_{-\infty}^{\infty} Q\frac{\partial\phi^*}{\partial\varphi}dx, \tag{2.20}$$

with $Q = iV_I(x)\phi$ representing the source/sink of new particles, thus being responsible for the non-conservation of the Hamiltonian for the general solution. Symbol φ stands for the three variational parameters introduced above, thus including the particle number N, the soliton width ω_b and the overall phase delay θ. Summarizing, Eq. 2.20 provides three variational expressions allowing the computation of μ, w_b and θ for a fixed number of particle N.

Computing the variation with respect to N, the corresponding RHS of Eq.2.20 is,

$$2\mathrm{Re}\int_{-\infty}^{\infty} Q\frac{\partial\phi^*}{\partial N}dx = \sqrt{\frac{2}{\pi w_b^2}}\mathrm{Re}\left\{i\int_{-\infty}^{\infty} V_I\exp\left(-\frac{2x^2}{w_b^2}\right)dx\right\}. \tag{2.21}$$

Eq.2.21 vanishes for two reasons: the integrand is a purely imaginary number, but at the same time the integral is zero owing to the odd symmetry

of its argument. Thus $\frac{d}{dt}\left(\frac{\partial\langle L_c\rangle}{\partial N_t}\right) - \frac{\partial\langle L_c\rangle}{\partial N} = 0$, from which we can find an explicit expression for the chemical potential μ as,

$$\begin{aligned}\mu = & \frac{\theta^2}{\sqrt{2\pi}\omega_b}\int_{-\infty}^{\infty}\left(\frac{df(x)}{dx}\right)^2\exp\left(-\frac{2x^2}{\omega_b^2}\right)dx \\ & + \frac{1}{2\omega_b^2} - \frac{N}{\sqrt{\pi}\omega_b} \\ & - \frac{\sqrt{2}V_r}{\sqrt{\pi}\omega_b}\int_{-\infty}^{\infty}\exp\left(-x^{2l}\right)\exp\left(-\frac{2x^2}{\omega_b^2}\right)dx.\end{aligned} \tag{2.22}$$

First term on the RHS of Eq.2.22 stems from the influence of the phase profile $\theta f(x)$ on the nonlinear eigenvalue μ; physically, μ increases as the overall phase profile across x grows up, that is, the net effect of the transverse flux is to weaken the localization of the condensate. Second and third term on the RHS of Eq.2.22 originate from the dispersive spreading and the two-body interaction term, respectively. In fact, their sign is opposed due to their opposite effect on the trapping of the condensate. Moreover, in agreement with the local Kerr like nonlinearity assumed in Eq.2.1, the nonlinear term depends on the intensity N/w_b. The last term in Eq.2.22 accounts for the trapping exerted by $V_R(x)$ and it is negative(thus favours the stabilization of the condensate). Also, it is directly proportional to the overlap between the particle distribution and the real potential V_R.

When variation with respect to the condensate width ω_b is computed, the integral involving the dissipative term vanishes in full analogy with

Eq.2.21. Euler-Lagrange equation in this case provides,

$$\begin{aligned}&\frac{1}{\omega_b^3}-\frac{N}{2\sqrt{\pi}\omega_b^2}\\&=\frac{\theta^2}{\sqrt{2}\sqrt{\pi}}\frac{\partial}{\partial\omega_b}\left\{\frac{1}{\omega_b}\int_{-\infty}^{\infty}\left(\frac{df(x)}{dx}\right)^2\exp\left(-\frac{2x^2}{\omega_b^2}\right)dx\right\}\\&-\frac{\sqrt{2}V_r}{\sqrt{\pi}}\frac{\partial}{\partial\omega_b}\left\{\frac{1}{\omega_b}\int_{-\infty}^{\infty}\exp\left(-x^{2l}\right)\exp\left(-\frac{2x^2}{\omega_b^2}\right)dx\right\}.\end{aligned}\tag{2.23}$$

The LHS of Eq.2.23 gives the competition between dispersion of the particles(term proportional to ω_b^{-3}) and negative scattering length(term proportional to w_b^{-2}) in determining the condensate width when the $\mathcal{PT}$ potential is lacking. We find that $N\propto w_b^{-1}$, thus avoiding the catastrophic collapse ascribable to a soliton width independent from N, occurring in the presence of Kerr nonlinearity(attractive two-body interaction) when diffraction/dispersion acts in more than one dimension[145]. The RHS of Eq.2.23 accounts for the influence of the $\mathcal{PT}$ potential on the condensate width, confirming the presence of an additional effective term on the potential well stemming from the transverse inhomogeneous phase of the soliton, as already discussed for the case of Eq.2.22.

Finally, we compute the Euler-Lagrange equation for θ. We have $\frac{\partial\phi^*}{\partial\theta}=-if(x)\phi^*$, the dissipative term in Eq.2.20 is purely real. Furthermore, the corresponding integrand is an even function of x. Thus, the overall phase delay θ is,

$$\theta=-2\frac{\int_0^{\infty}V_I(x)\exp\left(-\frac{2x^2}{\omega_b^2}\right)f(x)dx}{\int_0^{\infty}\left(\frac{df(x)}{dx}\right)^2\exp\left(-\frac{2x^2}{\omega_b^2}\right)dx},\tag{2.24}$$

with $V_I=-V_ix^{2l-1}\exp(-x^{2l})$ for potential A and $V_I=-V_ix\exp(-x^{2l})$ for potential B. Eq.2.24 shows that the phase of the solution vanishes when

the potential is purely real, hence demonstrating that, for purely real potentials, stationary solutions feature a flat phase profile across x, whereas the introduction of complex potentials results in stationary solutions with phase following the symmetry of the potential.

In the following sections of this chapter, we discuss and compare the variational results with those obtained from numerical analysis for different transverse profiles of the imaginary potential.

2.5 Discussion

To proceed with variational analysis, we have to choose a suitable form for the function $f(x)$ introduced in Eq.2.16. Numerically obtained stationary profiles suggest a $\tanh(x)$ profile for the phase of the solutions for low l. So, throughout the calculations we choose $f(x) = \tanh(x)$. We will also discuss how differences with the numerical simulations arise for high values of l and V_i.

2.5.1 Gaussian potential

Typical stationary profiles obtained numerically(dashed lines) are shown in Fig.2.7 for $l = 1$, that is, a Gaussian trapping potential and an odd profile for gain/loss(V_I for $l = 1$ is the first derivative of the Gaussian, both for potentials of type A and B). The corresponding solutions obtained using variational approach are also shown(solid lines). The density distribution $|\phi|^2$ of fundamental solitons is bell-shaped, irrespective of the values of V_i, V_r and μ. Results from the two approaches are in good agreement for low values of V_i, with a small discrepancy in the amplitude. The larger the V_i, the bigger the differences are. In fact, for $V_i > 0.7$ the corresponding linear system is actually in the $\mathcal{PT}$ broken state($V_c = 0.7$) as explained in section 2.2. The size of the condensate predicted from the variational

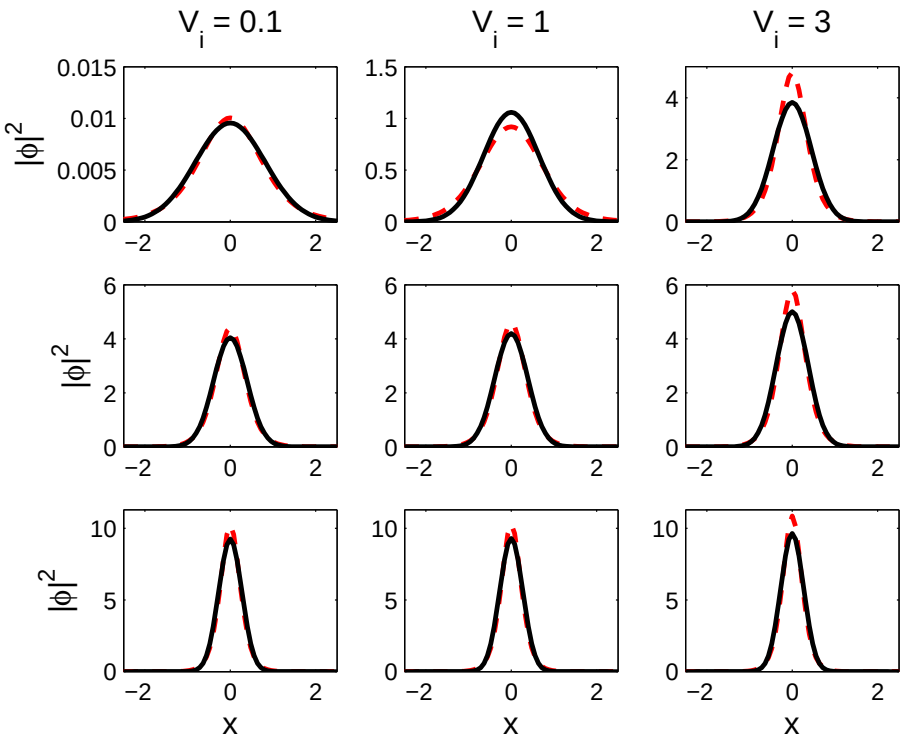

Figure 2.7: Soliton profiles versus x obtained from numerical simulations (dashed lines) and from variational analysis (solid lines), for different V_i as marked. Real potential $V_R(x)$ is Gaussian, i.e., it is $l = 1$. Top row: waveform for the lowest $|\mu|$ value ensuring soliton existence for each V_i, corresponding to $|\mu| = 0.48$, 0.7, and 2.26 from left to right, respectively. The other two rows correspond to $\mu = -3$ and $\mu = -6$, from top to bottom respectively. In all the plots we set $V_r = 1$. In all the panels comparison is made choosing μ and finding the corresponding particle number N from numerical simulations; then the variational solution corresponding to that value of N is used for comparison.

approach differs from the actual size, hence resulting in a comparatively large difference in the predicted amplitude. Dependence on the nonlinear eigenvalue μ can be appreciated comparing different rows: discrepancies depend slightly on the values of $|\mu|$, showing instead a strong dependence on V_i. Phase profiles of the solitonic solutions versus x are shown in the first two rows of Fig.2.8. The variational curves follow the same trend of the full numerical simulations stemming from Eq.2.1, but the two phase profiles differ by a small factor for which the variational approach is unable to account.

A detailed comparison of various parameters predicted from the variational analysis and the numerical simulations is presented in the last two rows of Fig.2.8 for three representative values of V_i. Regarding the nonlinear eigenvalue μ, a quantitative agreement between the two approaches is found for small V_i and small N. For very large V_i, the qualitative trend versus N is reproduced, but quantitative difference arise even for the lowest N. Finally, last row in Fig.2.8 shows that the two theories predict a very similar width, w_b, of the condensate with number of particles N. The accordance being improved as the particle number increases.

Some general conclusions can be drawn about the nature of solitons in the presence of a $\mathcal{PT}$-symmetric potential. As solitons become narrower, the number of particles N is increased due to the attractive two-body interaction, as in the case of self-focusing in a homogeneous Kerr media. The presence of V_i imposes a lower threshold in N for solitons to exist: physically the threshold appears owing to the transverse flux and the requirement for particle conservation. In particular, the fundamental soliton becomes narrower as V_i is increased. Despite the fact that the predicted values for the threshold(by both methods) do not match perfectly, variational analysis captures qualitatively the presence of a finite existence range for large V_i(the last two rows in Fig.2.8). To be specific, for the

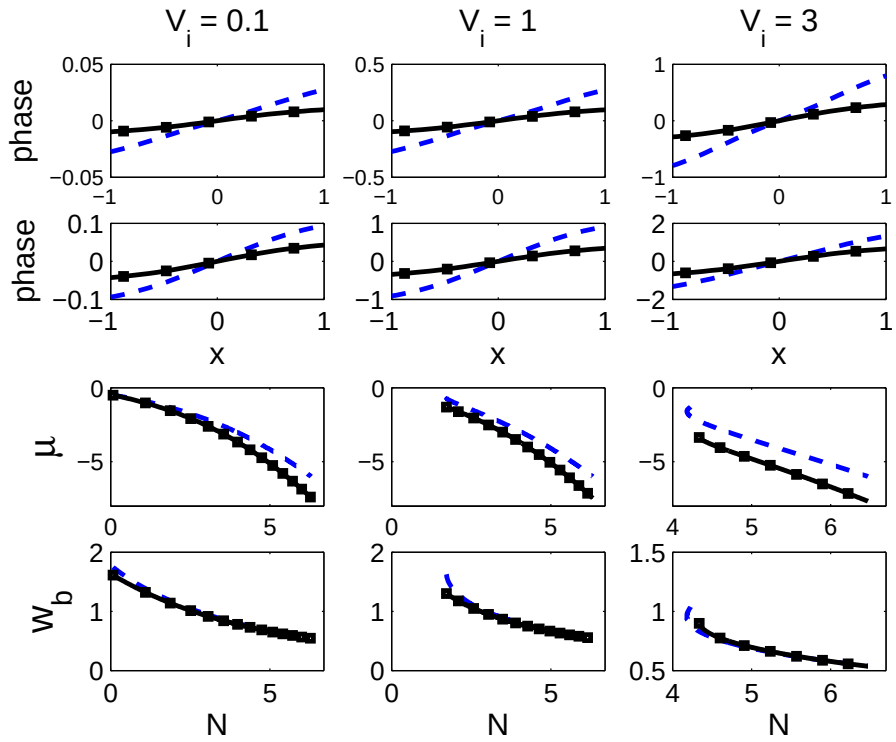

Figure 2.8: Phase profiles versus x for three V_i when $\mu = -6$ (top row) and for the lowest $|\mu|$ allowed (second row); in the latter case it is found that $|\mu| = 0.48$, 0.37 and 2.26, from left to right. The third and the fourth row report the behavior of the nonlinear eigenvalue μ and of the soliton width w_b versus the particle number N, respectively. In all the plots numerical and variational results are represented by dashed and solid line with $\square$, respectively.

case of $V_i = 3$, variational solutions exist from $\mu = -2.26$ and $N > 4.33$, whereas numerical simulations predict solitons existing for $N > 4.23$ with nonlinear eigenvalues smaller than $\mu = -1.3$.

2.5.2 Potential A

Now, we concentrate our effort on potential A, where the transverse profile of the imaginary component varies together with the profile of the real part of the potential. Fig.2.1 shows that in this case the gain/loss distribution, as l is increased, is more and more localized in proximity of the edge of the real potential. As the number of particles is increased, solitons shrink around the symmetry axis(i.e., $x = 0$) of the system so that only their tails interact with the gain/loss region. Thus, the transverse flux gets minimized. Solitonic profiles versus x are plotted in Fig.2.9 for three values of V_i and for three different l, both for low and high μ. Variational approach reproduces faithfully the actual solitons for $l = 2$, independent of the values of V_i. Quantitative differences take place for l larger than 4 for broad solitons, whereas the accordance remains very good for narrow solitons, no matter how large l is. In fact, in the latter case, there is no appreciable spatial overlapping between the intensity distribution and the imaginary potential.

The behavior of the chemical potential μ (Eq.2.22) and that of the beam width w_b (Eq.2.23) versus the particle number N are plotted in Fig.2.10, together with the corresponding numerical results. Qualitatively, variational analysis is capable of describing the behavior of both μ and w_b with the corresponding curves featuring a very similar shape; as for $l = 1$. Variational analysis is also able to specify a threshold for the soliton existence when V_i is large. At the same time, the quantitative differences can be appreciated. For small V_i and $l = 2$, the nonlinear eigenvalue μ matches for small N, tending to diverge as the particle number is increased. For

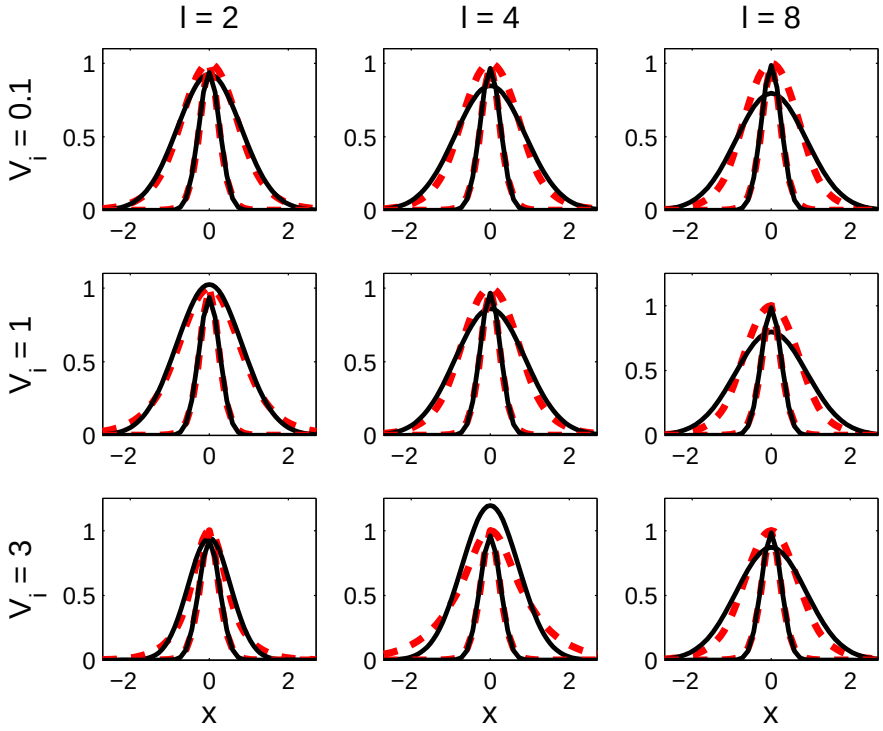

Figure 2.9: Family of potentials A. Normalized intensity profiles of the solitons obtained numerically (dashed lines) and those obtained from variational analysis (solid lines) are depicted for three different V_i as marked. All the curves are normalized with respect to the peak of the numerical solutions. Narrow profiles correspond to $\mu = -6$, whereas wider solitons correspond to the lowest eigenvalue ($|\mu|$), the latter depending on the pair l and V_i: for $l = 2$ the eigenvalues for each V_i is 0.54, 0.35 and 0.7 (from the smaller to the larger V_i, respectively); for $l = 4$ it is $|\mu| = [0.57, 0.52, 0.25]$; for $l = 8$ its $|\mu| = [0.75, 0.72, 0.6]$. In all cases $V_r = 1$.

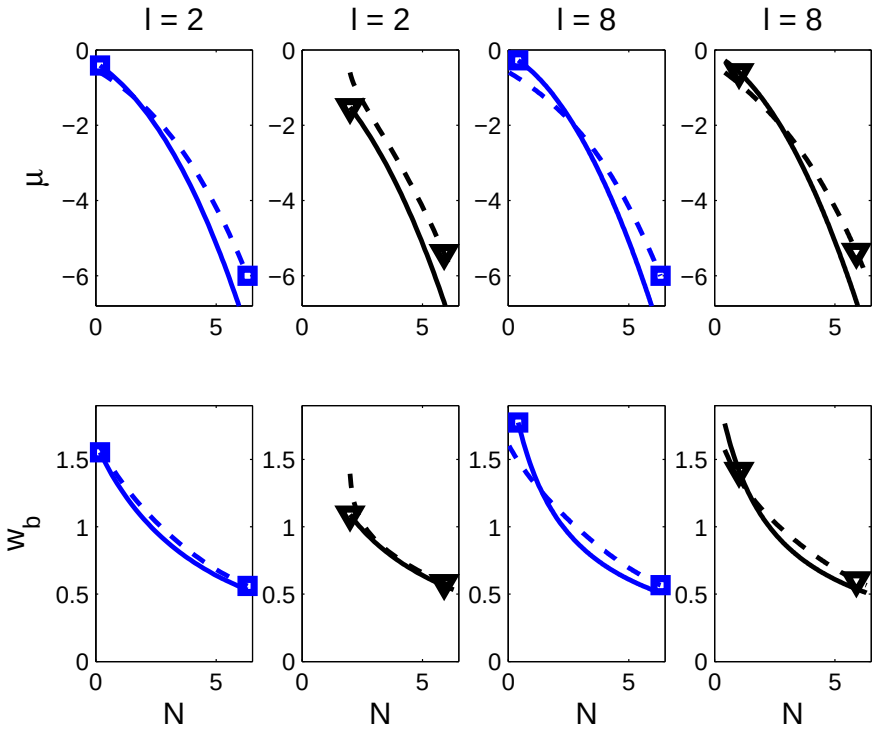

Figure 2.10: Family of potentials A. Behavior of μ and of the soliton width w_b versus the particle number N is plotted in the top and bottom row, respectively. Imaginary potential V_i is 0.1 in the first and third column ($\square$), whereas $V_i = 3$ in the second and fourth column($\triangle$), respectively. In all the plots numerical and variational results are represented by dashed line with symbols on the right and by solid lines with symbols on the left, respectively.

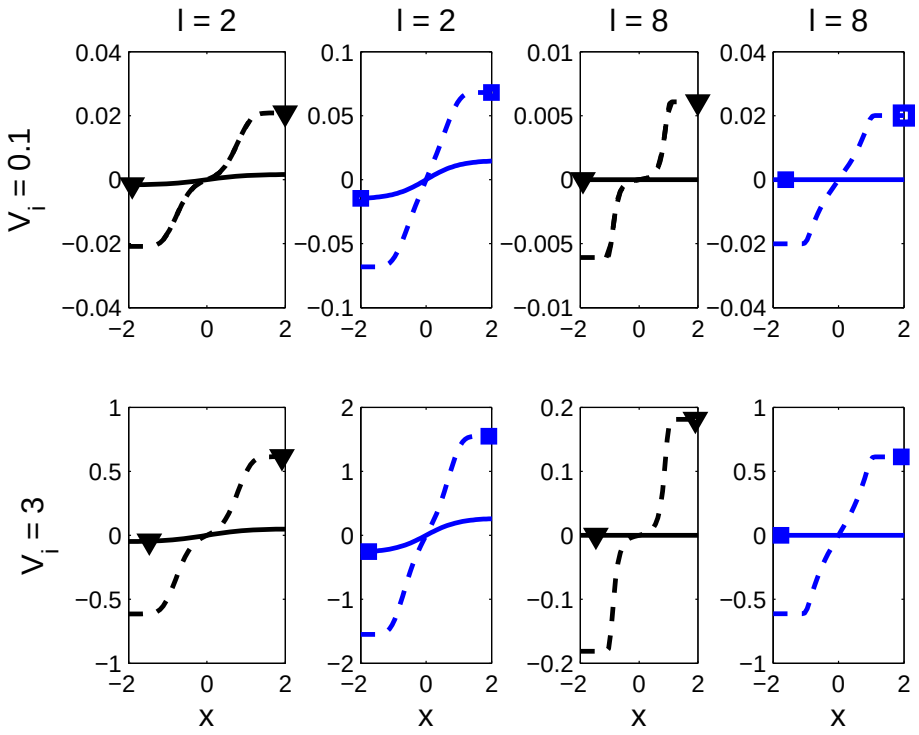

Figure 2.11: Family of potentials A. Soliton phase versus x profile for different shapes of the $\mathcal{PT}$-symmetric potential, determined by the values of l and V_i marked in the figure. Phase is plotted for $\mu = -6$ ($\triangle$, first and third column) and for the lowest allowed eigenvalue $|\mu|$ ($\square$, second and fourth column): for $l = 2$, the $|\mu|$ values are 0.54, and 0.7 for $V_i = 0.1$ and 3, respectively; similarly, for $l = 8$ the $|\mu|$ values are 0.75, and 0.6. Numerical and variational results are represented by dashed line with symbols on the right and by solid lines with symbols on the left, respectively.

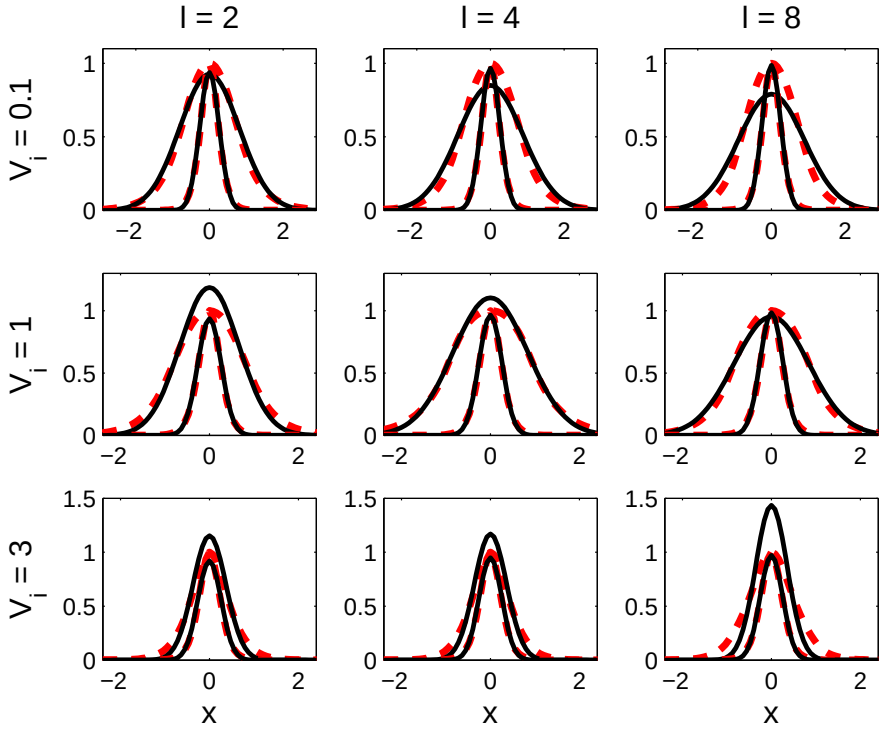

Figure 2.12: Family of potentials B. Normalized intensity profiles of the solitons obtained numerically (dashed lines) and those obtained from variational analysis (solid lines) are depicted for three different V_i as marked. All the curves are normalized with respect to the peak of the numerical solutions. Narrow profiles correspond to $\mu = -6$, whereas wider solitons correspond to the lowest eigenvalue ($|\mu|$), the latter depending on the pair l and V_i: for $l = 2$ the eigenvalues for each V_i is 0.54, 0.63 and 1.8 (from the smaller to the larger V_i, respectively); for $l = 4$ it is $|\mu| = [0.57, 0.39, 2]$; for $l = 8$ its $|\mu| = [0.74, 0.6, 1.6]$. In all cases $V_r = 1$.

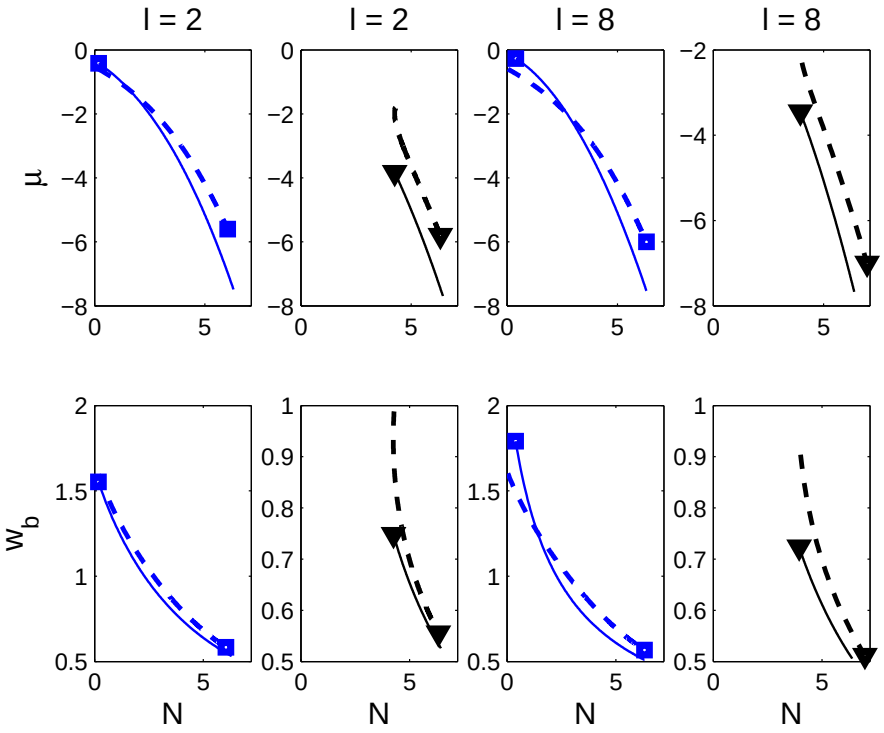

Figure 2.13: Family of potentials B. Behavior of μ and of the soliton width w_b versus the particle number N is plotted in the top and bottom row, respectively. Imaginary potential V_i is 0.1 in the first and third column ($\square$), whereas $V_i = 3$ in the second and fourth column($\triangle$), respectively. In all the plots numerical and variational results are represented by dashed line with symbols on the right and by solid lines with symbols on the left, respectively.

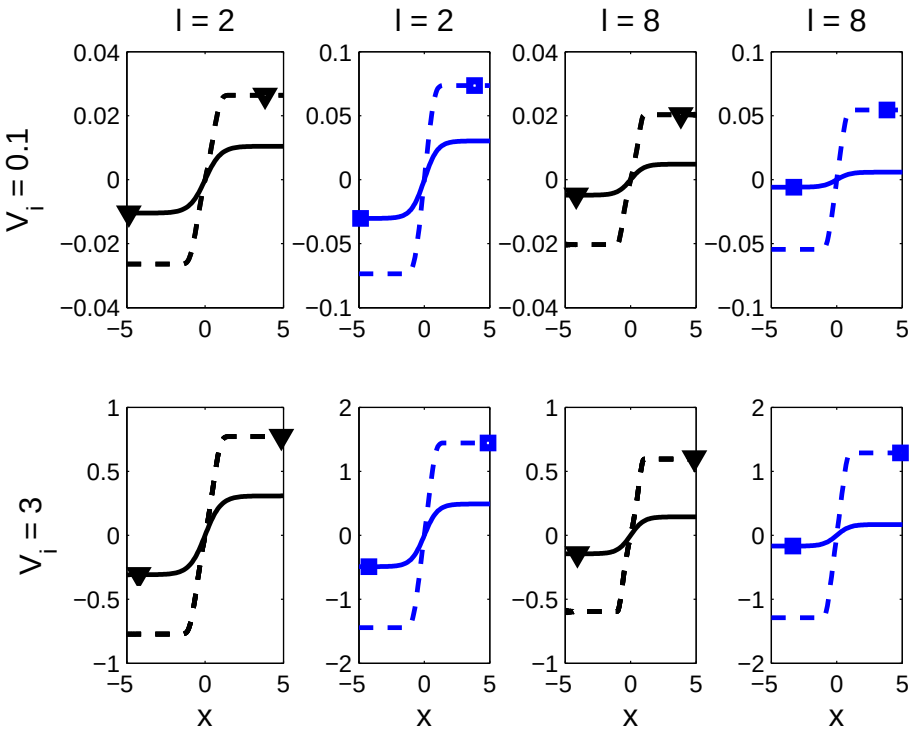

Figure 2.14: Family of potentials B. Soliton phase versus x profile for different shapes of the $\mathcal{PT}$-symmetric potential, determined by the values of l and V_i marked in the figure. Phase is plotted for $\mu = -6$ ($\triangle$, first and third column) and for the lowest allowed eigenvalue $|\mu|$ ($\square$, second and fourth column): for $l = 2$, the $|\mu|$ values are 0.54, and 1.8 for $V_i = 0.1$ and 3, respectively; similarly, for $l = 8$ the $|\mu|$ values are 0.74, and 1.6. Numerical and variational results are represented by dashed line with symbols on the right and by solid lines with symbols on the left, respectively.

$l = 2$ and $V_i = 3$, an initial displacement(i.e., in correspondence to the threshold) between the two curves is observed. Then, for high N the eigenvalue μ approaches the same values for each V_i owing to the high degree of spatial localization achieved. For $l = 8$, the soliton threshold almost disappears owing to the small overlap of the field with the imaginary potential. For the same reason, and according to both the techniques, the trend of μ with N results to be slightly dependent on V_i. Finally, the variational and the numerical curves cross around $N = 2$, stating that differences at small N arise from the shape of the potential.

Behavior of w_b is similar: for $l = 2$ an appreciable divergence between the two approaches occurs only in the proximity of the threshold for large V_i, whereas the soliton width matches almost perfectly for other N values. For $l = 8$ variational analysis predicts a wider condensate width for small N. After the crossing point, variational widths become narrower, tending to coincide with the exact values for $N \approx 6$.

The quantitative discrepancies between variational and exact solutions can be mainly attributed to the trial function used for the phase profile $f(x)$. The phase profiles obtained from the two approaches do not even show the same spatial shape (Fig.2.11): in fact, the hyperbolic tangent profile assumed for $f(x)$ is best suited for $l = 1$ whatever μ is.

Let us start from the nature of the exact phase profile. First, the overall phase jump increases with V_i owing to the larger flux of particles required for particle conservation. Second, the overall phase jump for $l = 8$ is about half the value for $l = 2$, owing to the smaller overlap between the field and the imaginary potential. Third, the overall phase jump decreases as μ diminishes(N increases) owing to the stronger self-localization. Let us now discuss the spatial shape of the phases. According to Eq.2.12, the phase gradient does not appreciably change when the local imaginary potential is small, whereas it can undergo a change in the convexity($d^2\xi/dx^2$

changes its sign) when the generation/destruction of particles is relevant. Accordingly, for low l and small V_i phase shows a single inflection point placed at $x = 0$(case $l = 2$, $V_i = 0.1$ and $\mu = -0.54$ in Fig.2.11 and also in Fig.2.8). As N increases, for $V_i = 0.1$ and $l = 2$ the single inflection point separates into two distinct points, symmetrically placed with respect to $x = 0$. A similar but faster(i.e., occurring at lower N) transition can be observed if V_i is increased. For example, for $V_i = 3$ and $l = 2$ the first existing soliton already shows two inflection points(Fig.2.11). For larger values of l the two inflection points appear even for lower excitations due to the larger strength of the local imaginary potential. For example, for $l = 8$, the phase profile is almost flat around $x = 0$ and increases on the edges due to the narrowness of solitons and the low overlap with the gain/loss regions(Fig.2.11). The simple trial function used in the variational computation does not account for this: as a consequence, a very small θ value is predicted: particularly for $l = 8$ it is of the order of 10^{-3} for small N, the magnitude of which further decreases with increasing N.

2.5.3 Potential B

Now, let us turn our attention towards potential B, where the transverse profile of the imaginary part of the potential varies slightly and does not undergo strong localization as the real part of the potential is varied. Stated otherwise, the gain/loss regions now span throughout the real potential, irrespective of the profile of the real potential. Analogously to potential A, for low values of l and V_i, the soliton solutions match quite well with numerical findings, above all when the condensate is strongly self-confined(Fig.2.12). Behavior of μ and width w_b versus N for $V_i = 0.1$ is very similar to potential A due to the small transverse flux(Fig.2.13). Conversely, differences between A and B are relevant when V_i becomes larger. For example, when $V_i = 3$ soliton threshold shifts towards larger

N, both for l equal to 2 and 8(Fig.2.13); variational equations are used to compute the threshold positions with a good degree of accuracy. Additionally, both μ and w_b computed from variational method are smaller than the numerically found values. Finally, Fig.2.14 shows the phase profile of solitons for potential belonging to type B. Due to the spatially wider imaginary potential, the numerical phase shows a single inflection point at $x = 0$, regardless of V_i and l. Thus, the trial function assumed for $f(x)$ possesses the same shape as of the actual phase. Nonetheless, the corresponding phase profiles for $l = 2$ have a mismatch by a factor of 2 in the magnitude θ, the latter increasing for greater l. For $l = 8$, the overall phase jump θ computed from variational method undergoes slight modifications as μ changes.

2.6 Stability and Dynamical Evolution

The stability of the stationary solutions ϕ is analyzed using the Bogoliubov-de Gennes(BdG) equations[123] which are obtained by linearizing the GPE by considering the Bogoliubov ansatz for elementary excitations:

$$u = (\phi + p(x)\exp(i\lambda t) + q(x)\exp(-i\lambda^* t))\exp(-i\mu t), \tag{2.25}$$

which gives the linearized BDG equations as,

$$\lambda \begin{bmatrix} p \\ q^* \end{bmatrix} = \begin{bmatrix} L_1 - iV_I(\xi) & \phi^2 \\ -(\phi^*)^2 & -L_1 - iV_I(\xi) \end{bmatrix} \begin{bmatrix} p \\ q^* \end{bmatrix}, \tag{2.26}$$

where $L_1 = -\mu + \frac{1}{2}\frac{\partial^2}{\partial x^2} + 2|\phi|^2 - V_R$.

If the frequency λ is real, the perturbed stationary state will be stable, whereas, if the frequency is complex, the stationary state experiences oscillatory instability(OI). If it is purely imaginary, the solutions are said to be linearly unstable undergoing exponential amplification. Solving Eq.2.26

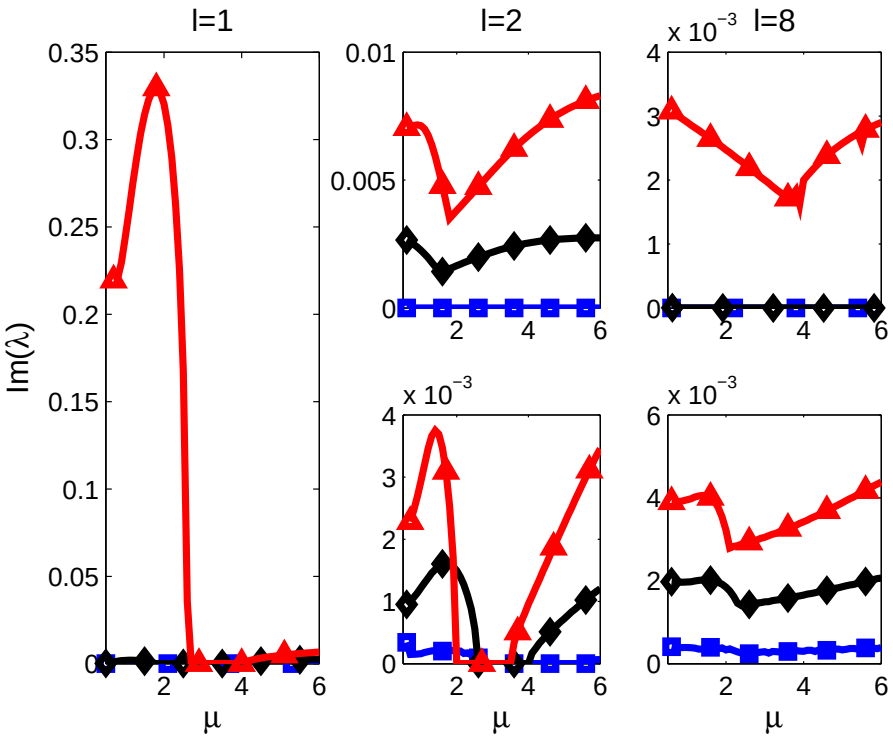

Figure 2.15: Stability eigenspectrum computed from Eq.2.26 for varying V_i values with $V_i = 0.1$ (blue $\square$), $V_i = 0.5$ (black $\diamond$) and $V_i = 1$ (red $\triangle$). In general solitons become highly unstable when $V_i > V_c$. Keeping V_i fixed, larger l enhances soliton instability for potentials of type B (bottom row) if compared with type A (top row). Instability spectrum also shows a dependence on the chemical potential μ.

we find that the eigen values of the instability spectrum are either real implying linear stability or complex implying oscillatory instability. In general, we can say that the condensate will be dynamically stable when the imaginary part of the potential V_i is much less than the critical point V_c at which the $\mathcal{PT}$-symmetry is spontaneously broken. The stability of the condensate also depends on the chemical potential μ. Representative behavior of the instability spectrum is depicted in Fig.2.15 for various V_i and l values, for numerically obtained solutions. From this, we can infer that, the profiles deviating from the actual stationary solution will act as a perturbation and the evolution of this perturbation will depend on the instability associated at that particular chemical potential value. That is, for example, for low V_i values, the Bogoliubov analysis suggests stable condensate. The condensate will survive small perturbations to it. That is, the initial condensate profiles differing slightly from the actual profile can be stable for sufficiently long time. Qualitatively, similar instability spectrum is obtained for the variational solutions as well predicting stability for low V_i and instability for high V_i.

2.7 Propagation dynamics

The results obtained above from the linear stability analysis of solitons have been checked numerically by computing soliton dynamics in the presence of noise. We have employed standard beam propagation method using Crank-Nicolson scheme for diffraction. The Strang splitting, an asymmetric operator splitting featuring second order accuracy, is used for simulations with high V_i, where stationary solutions are obtained near the $\mathcal{PT}$-symmetry breaking point.

We have investigated field dynamics when a soliton, perturbed with Gaussian noise encompassing a magnitude 1% of the soliton amplitude,

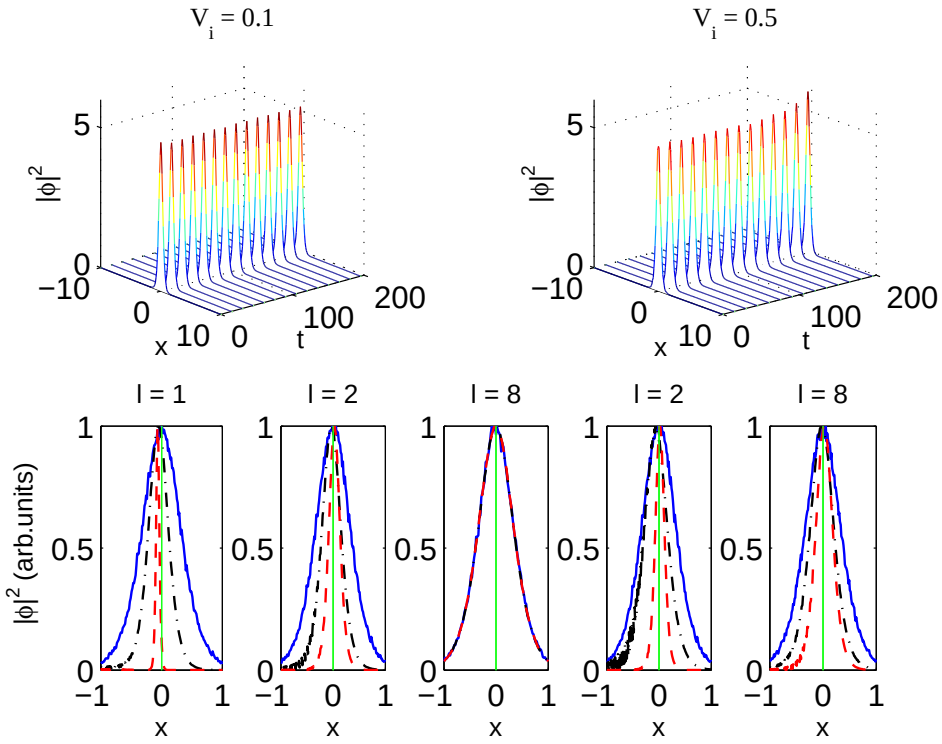

Figure 2.16: Top row: Intensity evolution of soliton solutions for $\mu = 3.4$ and (left panel) $V_i = 0.1$ showing unperturbed soliton and (right panel) $V_i = 0.5$ showing increase in power. Bottom row: Transverse profiles of the solution for $V_i = 1$, $\mu = 3.4$ for potential A are shown for $\zeta = 0$ (blue solid line), $\zeta = 100$ (black dotted line) and $\zeta = 110$ (red dashed line) for $l = 1$; $\zeta = [0\ 140\ 150]$ for $l = 2$; $\zeta = [0\ 150\ 200]$ for $l = 8$ and for potential B (last two columns) for $\zeta = [0\ 130\ 140]$ for $l = 2$ and $\zeta = [0\ 129\ 135]$ for $l = 8$ showing narrowing and peak oscillation upon propagation. The profiles are normalized with power for better visibility.

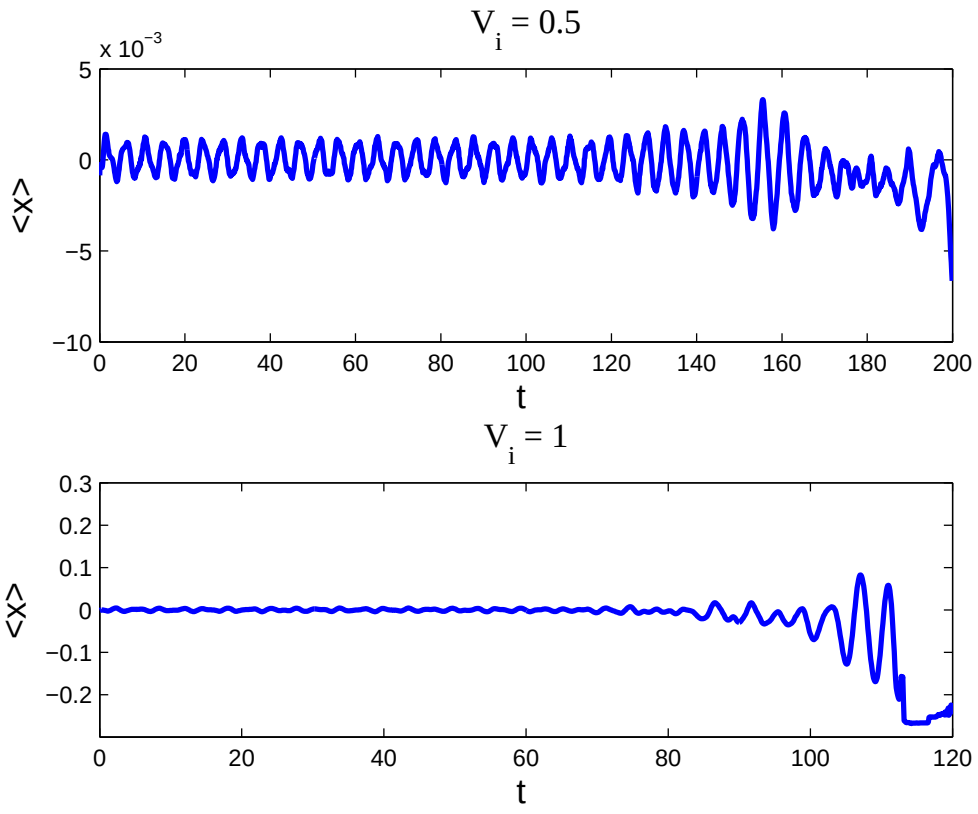

Figure 2.17: Evolution of soliton trajectory $\langle x \rangle$ for $V_i = 0.5$ and $V_i = 1$ for $l = 1$ and $\mu = 3.4$ showing the oscillations in the nonlinear wave trajectory.

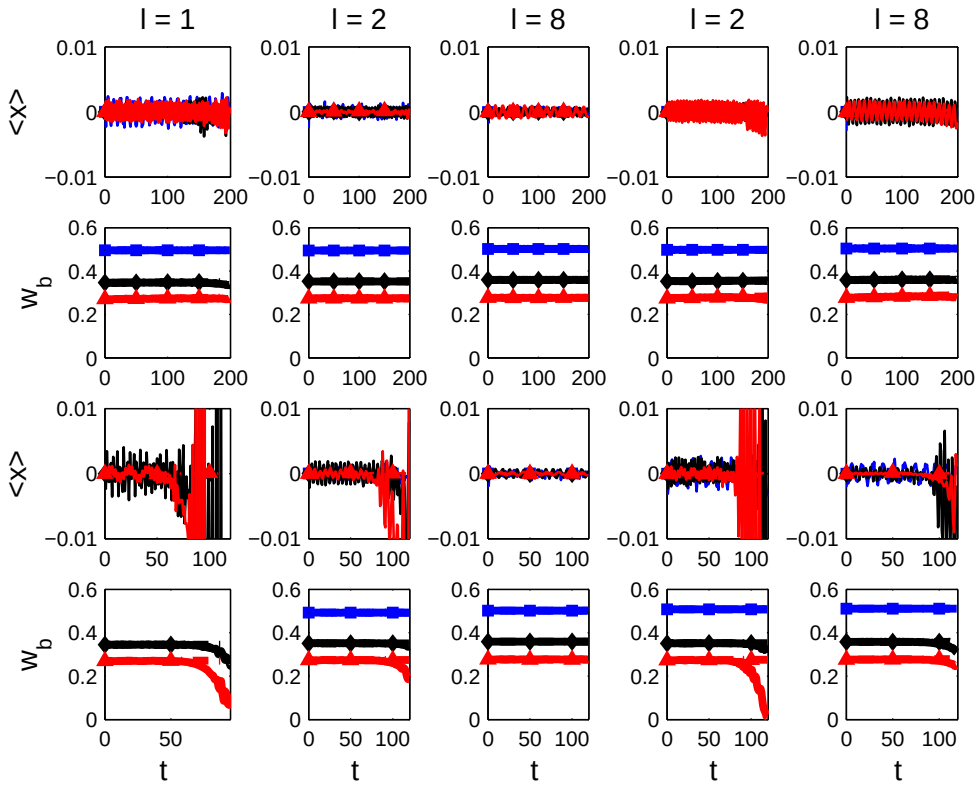

Figure 2.18: Evolution of trajectory $\langle x \rangle$ and width w_b vs t for $V_i = 0.5$ (top two rows) and $V_i = 1$ (bottom two rows) for potentials of type A (second and third column) and potentials of type B (last two columns) for different l and V_i as marked; for $l = 1$ both the potentials are equivalent. Dotted lines correspond to the propagation of stationary nonlinear modes where as solid lines correspond to wave evolution initially perturbed by 1% random noise in amplitude for $\mu = 0.7$ ($\square$), $\mu = 3.4$ ($\diamond$) and $\mu = 6$ ($\triangle$).

is taken as the input beam. Representative results are shown in Fig.2.16. For $V_i = 0.1$ the soliton is stable over the dynamical evolution whereas for $V_i = 0.5$, solution experiences exponential growth due to an instability mode with $\mathrm{Im}(\lambda_{\mathrm{dom}}) \approx 2 \times 10^{-3}$($\lambda_{\mathrm{dom}}$ is the maximum of imaginary part of the eigenvalue λ), in good agreement with Linear Stability Analysis(LSA). Results from LSA are confirmed also in the presence of stronger instability: in this case field distribution loses its spatial symmetry and undergo a much stronger exponential growth. In the bottom row of Fig.2.16, transverse profiles of the beam at various longitudinal sections are shown for $V_i = 1$, for both types of potentials A and B, and for various l values. At each section field is normalized to the local power to improve the visibility. Solitons acquire an asymmetric profile across x while evolving and eventually converting to a strongly localized mode which undergoes exponential amplification.

The oscillations in the peak of the solution owing to OI can also be observed; the time evolution of the *center of mass* of the field $\langle x \rangle = \int |\psi|^2 x dx / \int |\psi|^2 dx$ is graphed in Fig.2.17 and also in Fig.2.18, together with the width of the beam, w_b. Specifically, solitons with three different μ values with low, intermediate and high magnitude were considered for the propagation studies. The intermediate value is chosen to be $\mu = 3.4$, which for low l falls in the window where the solutions are predicted to be quasi-stable by LSA. Numerically found time evolutions are depicted in Fig.2.18. The time evolution of the beam width is depicted for different l values as marked for both propagation with noise(dotted lines) and without added noise(solid lines). Simulations are in very good agreement with LSA predictions: for low V_i, solitons are quasi-stable for both the potentials; LSA predicts a small exponential amplification for $V_i = 0.5$, confirmed by numerics. A good agreement is found also for $V_i = 1$: field intensity first starts to breathe upon time evolution owing to the inter-

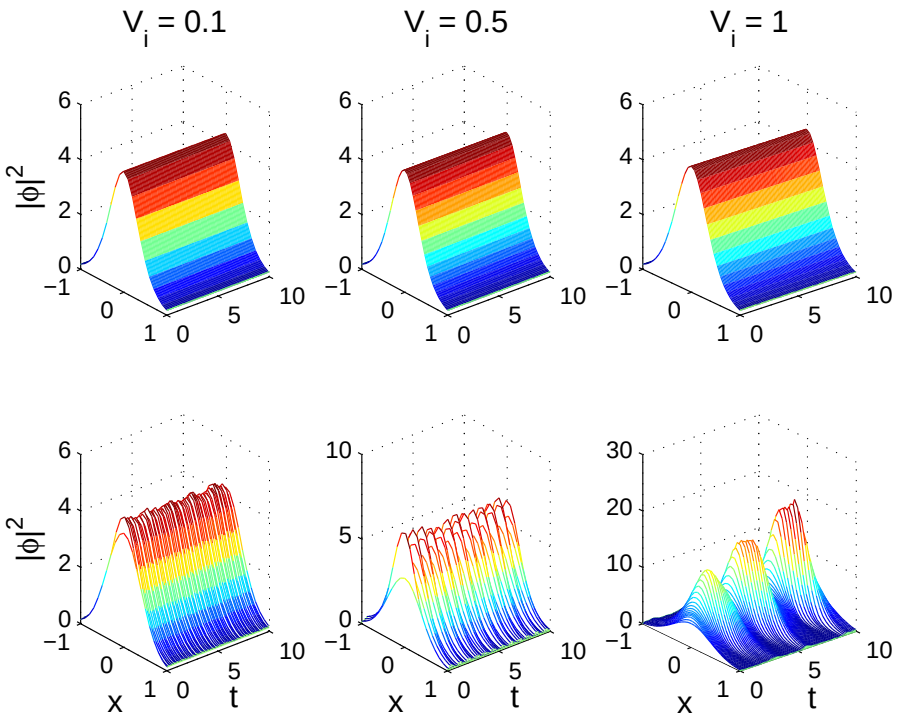

Figure 2.19: Dynamical evolution of the condensate for both numerical solutions (top row) and the corresponding variational results (bottom row) for $l = 1$ and $\mu = -3$; V_i values are as shown in the figure.

ference between the solitonic profile and the eigenmode associated with λ_{dom}. At the same time, an exponential growth of the perturbative mode occurs. After a given time, the perturbation becomes larger than the soliton width and the overall field is mainly composed by a very narrow bell-shaped wave positioned in the gain region undergoing very strong amplification supported by nonlinear self-focusing.

Physically, instability is strictly related with the presence of some linear eigenstates encompassing a complex eigenvalue, a general property of localized complex potentials, different to what happens in periodic systems[141, 142]. Thus, we can conclude that $\mathcal{PT}$-symmetric solitons

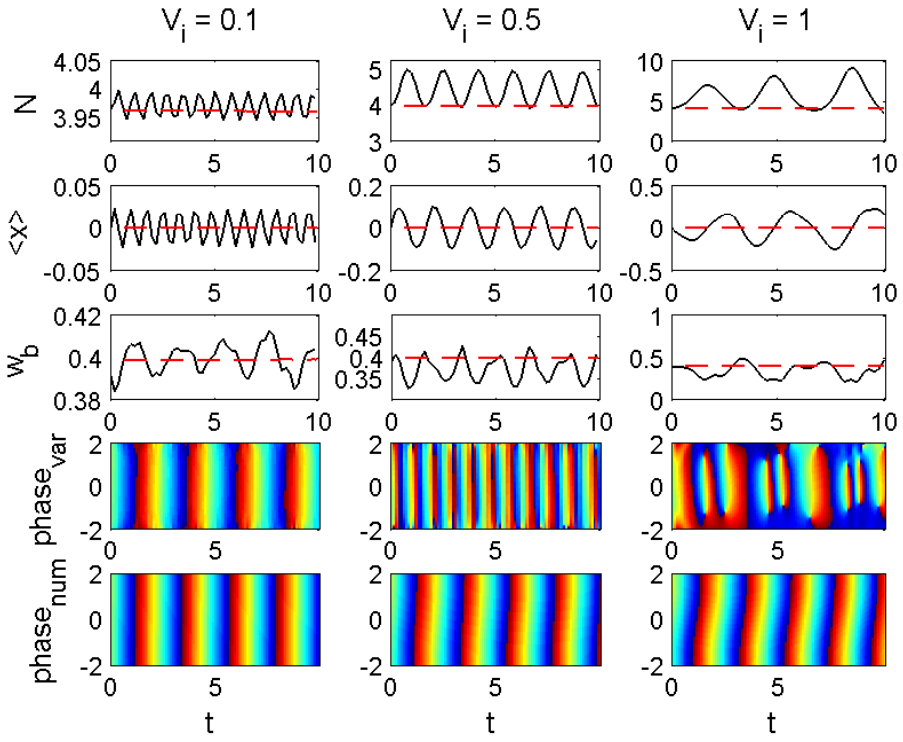

Figure 2.20: Dynamical evolution of the total number of particles N (top row), together with the center of mass $\langle x \rangle$ (second row) and width w_b (third row). Dashed lines correspond to evolution in time of the stationary solutions taken as input in the numerical code solving directly Eq. 2.7, whereas the solid lines correspond to the stationary regime computed with the variational approach. The evolution of both variational (fourth row) and numerical (last row) phase is plotted as well. The parameters are $l = 1$ and $\mu = -3$; V_i values are reported directly in the figure.

supported by localized potentials are in general unstable. The instability manifests appreciably at large propagation distances with respect to the Rayleigh length for $V_i < V_c$, whereas solitons survive for short distances when $V_i \geq V_c$. For example, in Ref.[146] authors claim solitons are stable, whereas we have demonstrated that solitons are actually subjected to a small exponential growth, an important detail in applications such as laser cavities.

To further verify this and also to check how variational solutions are similar to condensate profiles obtained numerically, we have compared the dynamical evolution of the solutions obtained from the two approaches. Dynamical evolution of the condensate is also necessary to corroborate the results from the BDG analysis. As a representative case, plots of the intensity evolution $|\phi|^2$ with time t for different V_i and $l = 1$ are shown in Fig.2.19. It has to be noted that numerically obtained stationary solutions are propagated with out the inclusion of any noise, so that the condensate maintains its stationary profile. Due to the differences between the semi-analytical solution and the exact soliton, the condensate does not preserve its shape on evolution. Instead, a breathing behavior (i.e., periodic oscillations on the wave size) jointly with an oscillatory trajectory is observed. Oscillations in the field survive and remain bounded for time scales much larger than $t_d = 2w_b^2/\omega_\perp$, at which a beam of width $w_b a_\perp$ expands by $\sqrt{2}w_b a_\perp$ in the free diffusive regime (for example a beam of width $w_b = 0.4$ taken at $t = 200$ corresponds to $625t_d$): we deduce that instability does not take place, i.e., exponential growth on propagation is ruled out, at least on realistic time lags. Whereas, in the $\mathcal{PT}$-broken state ($V_i = 1$), this no more holds true and the condensate experiences exponential growth together with oscillation in the trajectory at very small time scale.

The dynamic evolution of the number of particles N, the center of

mass $\langle x\rangle = \int |\phi|^2 x dx / \int |\phi|^2 dx$ and the size of the condensate are plotted in Fig.2.20, together with the phase distribution for both the numerical and variational solutions. The oscillating trajectory can be attributed to the non-stationary particle flux associated with discrepancies with respect to the actual solitary waves. Displacement from zero of the center of mass is proportional to the magnitude of V_i. The width of the beam oscillates around the actual width of the numerical soliton on propagation both for low and high V_i, trying to evolve into a stationary solution; correspondingly the particle number N also oscillates around the stationary density.

2.8 Summary of the chapter

We have used numerical and variational methods to obtain the solitonic solutions of a BEC subjected to a focusing nonlinearity and a trapping potential featuring $\mathcal{PT}$-symmetry. Starting from a mean field approach, a simplified one-dimensional equation governing the evolution of matter waves in a complex trapping potential is found. We study two families of complex potentials in order to understand the effects of the shape of the gain and loss mechanisms on the existence and features of the solitons. To this extent, a super-Gaussian trapping potential is chosen for the real part, coupled with two different families of functions for the gain/loss mechanisms. In the first type gain/loss varies together with the form of the real part of the potential, concentrating where the real potential varies; in the second type gain/loss spatial distribution remains almost invariant, overlapping spatially across the whole extension of the real part of the potential.

For the variational approach, suitable trial solutions based on the features of the system, that is, an even real part and an odd imaginary part for the stationary solution, was chosen. We found a good agreement be-

tween variational predictions and actual values for the soliton width and chemical potential, whereas in the phase profile larger discrepancies are found when the gain/loss regions become highly localized with respect to the matter wave, principally attributed to the improper choice of the variational function modeling the transverse profile of the phase. Ideally, such a function should model the convexity changes associated with the phase gradient occurring with increasing gain/loss in the system. The agreement between the two approaches is particularly good when the real part of the potential is Gaussian and the imaginary part is Hermite-Gaussian of order 1; the width, chemical potential and the phase predictions agree very well.

Appreciable deviations in the two approaches occur when the system is far away from the $\mathcal{PT}$-breaking point, i.e., when the gain/loss mechanism is very high, irrespective of the shape of the potential. We demonstrate that a lower threshold in the particle number for the existence of solitary solutions, strongly dependent on the imaginary component of the potential, exists, the existence region shrinking as the gain/loss magnitude grows up. The variational approach is capable to describe qualitatively the phenomenon, with a degree of accuracy on the order of 0.3%. Finally, we demonstrated that the threshold in particle number is much larger when the overlap between the imaginary potential and the field is large, due to the larger transverse flux required to achieve a stationary solution. We also carried out the stability analysis as well as the full dynamical evolution of both numerically and variationally obtained solutions and compared the density oscillations, width and center of mass variations from that of the actual solutions.

3

Soliton scattering by $\mathcal{PT}$ symmetric defects in a 1-D Bose-Einstein condensate.

In this chapter we study the unidirectional behavior shown by BEC trapped in 1-D super-Gaussian $\mathcal{PT}$ symmetric potential represented by Eq.2.7(in chapter 2). The unidirectional behavior is explained as the almost perfect transmission occuring in one direction and almost perfect reflection occuring in the other direction when light beams scattered off by a potential from two opposite directions. Scattering dynamics of matter waves by a potential is a textbook problem in quantum mechanics[147–151] and has been studied widely in different contexts: in particle physics, condensed matter physics and in nonlinear optics[152–154]. When matter wave is interacting with a defect, a resonant transmission or reflection occurs. Such behavior can find applications for practical purposes. Interaction of solitons resulting in chaotic scattering behavior has been considered in[155], where fractal behavior was observed for certain velocities and was explained by the n-bounce resonance phenomenon.

Interaction of solitons with potential barrier or well is the key mechanism for atom interferometers[156, 157], atom-surface interfaces[158] and matter-wave soliton interferometer[159]. Numerous theoretical[160–163] as well as experimental investigations[164, 165] concentrate on scattering of solitons from different type of potential barriers or wells. Eventhough

scattering of waves is studied in many contexts in physics, BEC seems to be a true candidate for the scattering studies as far as the above said applications are considered.

The significance of symmetries and spectral characteristics of optical systems are often analyzed using light scattering studies. Recently scattering by $\mathcal{PT}$ symmetric potential is more attended by researchers as it shows special properties. One of the main outcomes of scattering studies in $\mathcal{PT}$ symmetric nonlinear systems is the observation of nonreciprocal transport especially with low power threshold[78, 80]. It is noted that the Hermitian counter part does not show such unidirectional properties. Experimental realization of diode type transmission effect at the exceptional point(phase transition point) on-chip parity-time metamaterials is demonstrated in[87]. $\mathcal{PT}$ symmetric LCR circuit which shows the dual behavior of scattering at some characteristic frequencies, is experimentally demonstrated in[166]. The scattering of linear and nonlinear waves in a long waveguide array with a $\mathcal{PT}$ symmetric defect created by two waveguides is discussed[167, 168] in which they demonstrated that the reflected and transmitted linear and nonlinear waves can be substantially amplified by the $\mathcal{PT}$ symmetric defect.

Some other works in literature that deal with the scattering by $\mathcal{PT}$ defects which include scattering of gap solitons[169], scattering by $\mathcal{PT}$ Gaussian potential[170]. Scattering studies in $\mathcal{PT}$ symmetric nonlinear systems show nonreciprocal transport[80], repeated reflection transmission and trapping depending on the strength of the potential[171–174], multisoliton scattering[175] and magnetic flux controlled non-Hermitian $\mathcal{PT}$ system[174]. These studies are greatly acknowledged because of its importance in the field of quantum information processing[80], on-chip isolators and circulators[176].

3.1 Model

The GPE for $\mathcal{PT}$ symmetric BEC with one dimensional setting have already been discussed in chapter 2. For the sake of continuity, the model equation and the form of $\mathcal{PT}$ symmetric trapping potential are shown here again,

$$i\frac{\partial u}{\partial t} = -\frac{1}{2}\frac{\partial^2 u}{\partial x^2} - |u|^2 u + V(x)u, \tag{3.1}$$

where the real part of the potential is given by,

$$V_R = -V_r \exp(-x^{2l}) \ (l = 1, 2, \ldots), \tag{3.2}$$

and the imaginary part of the potential(type-A),

$$V_I^A(x) = -V_i x^{2l-1} \exp(-x^{2l}). \tag{3.3}$$

3.2 Scattering Dynamics

We study the scattering dynamics of a soliton given by [60],

$$\psi = A sech\left[A(x - x_0)\right] \exp(iv_{inc}x),$$

moving with a velocity v_{inc} towards the $\mathcal{PT}$-symmetric defect, coming from $\pm x_0$. A is the amplitude and inverse spatial width of the soliton. Dynamics is analyzed in terms of the reflection(R), transmission(T) and capture(C) coefficients which are defined as,

$$R = \frac{1}{P}\int_{-\infty}^{-h} |\psi|^2 dx, \tag{3.4}$$

$$T = \frac{1}{P}\int_{h}^{+\infty} |\psi|^2 dx, \tag{3.5}$$

$$C = \frac{1}{P}\int_{-h}^{h} |\psi|^2 dx, \tag{3.6}$$

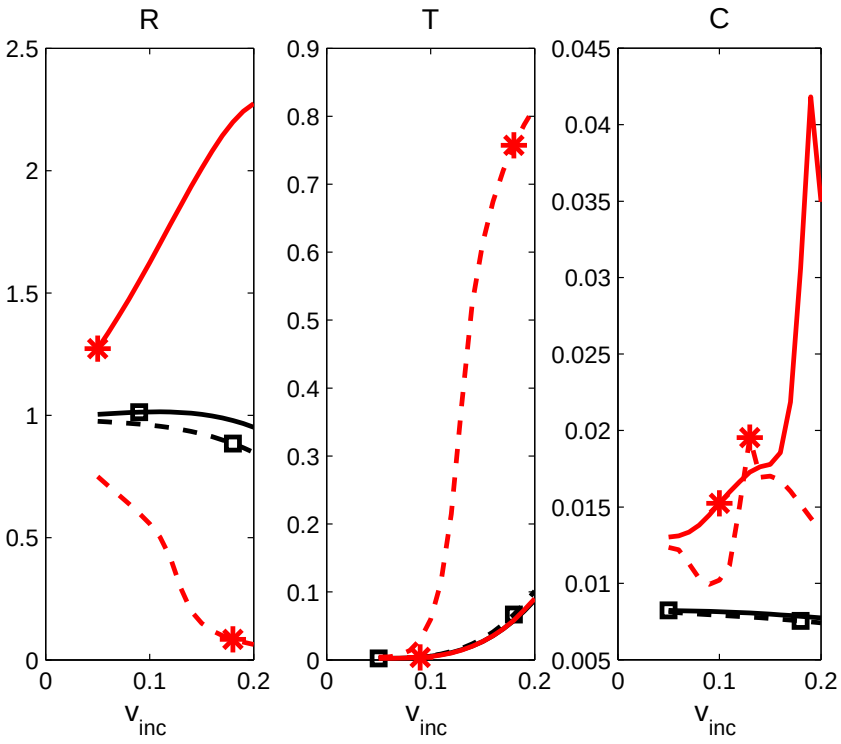

Figure 3.1: Variation of the reflection, transmission and capture with input velocity at the output plane $t = 400$. for $V_i = 0.1$ ($\square$) and $V_i = 0.7$. ($*$). Solid lines correspond to soliton impinging from the left ($x_0 = +10$) and dotted lines to that of solitons impinging from the right ($x_0 = -10$) of the defect. Here, $A = 0.3$, $l = 2$

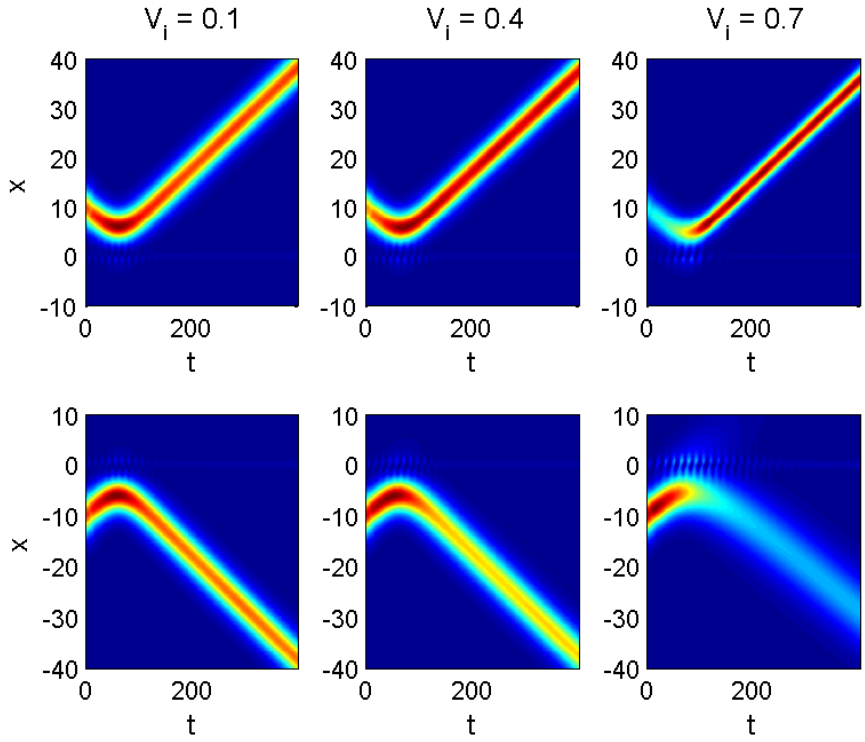

Figure 3.2: Intensity($|\psi|^2$) evolution in the plane x-t depicting the scattering dynamics of the impinging soliton for various V_i as marked for input velocity $v_{inc} = 0.1$. Here, $A = 0.3$, $l = 2$ and $x_0 = \pm 10$.

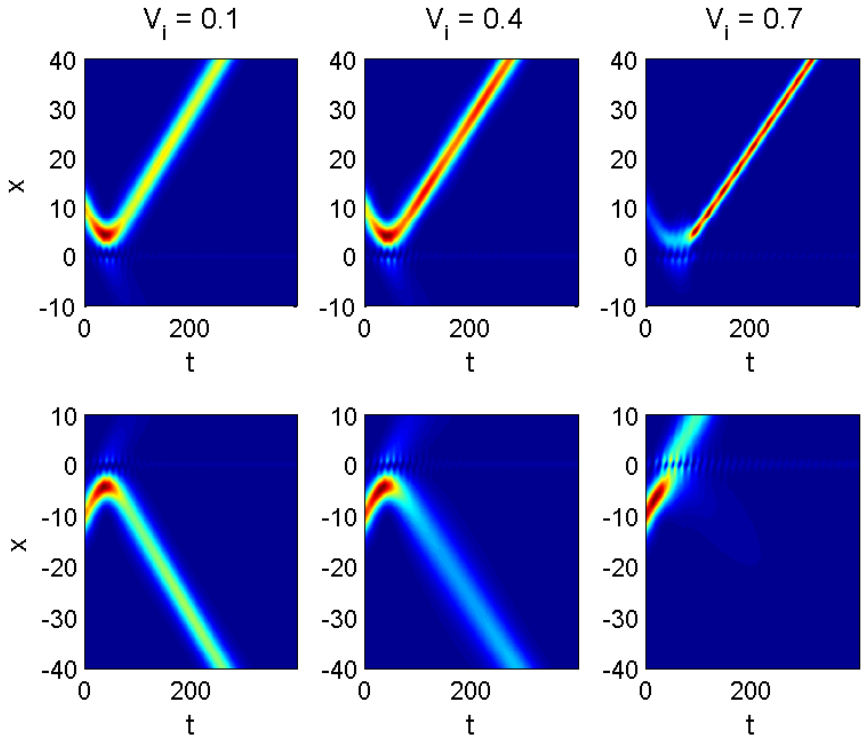

Figure 3.3: Intensity($|\psi|^2$) evolution in the plane x-t depicting the scattering dynamics of the impinging soliton for various V_i as marked for input velocity $v_{inc} = 0.2$. Here, $A = 0.3$, $l = 2$ and $x_0 = \pm 10$.

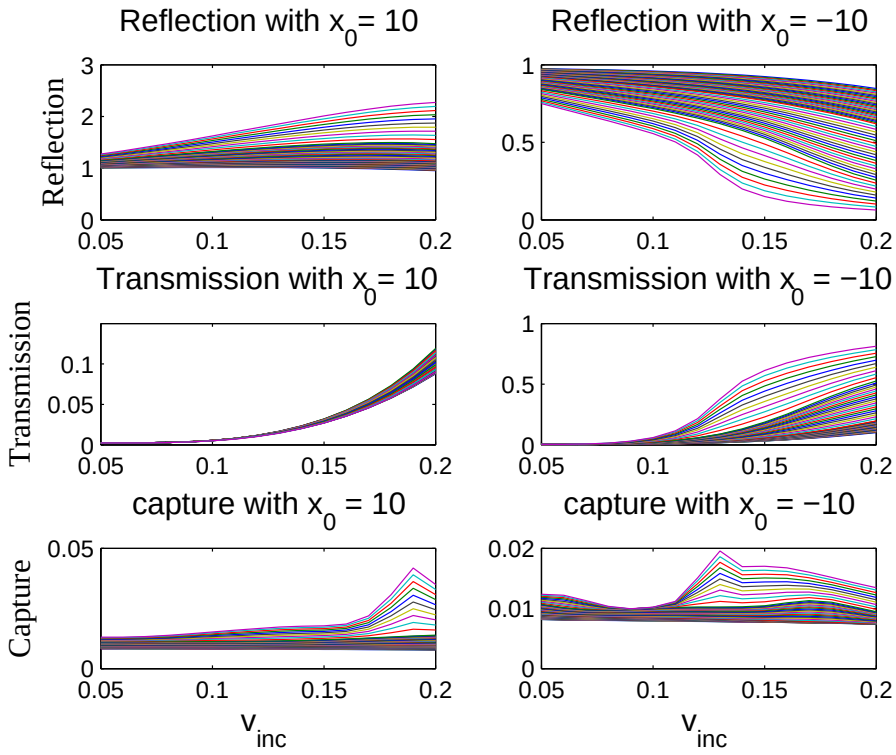

Figure 3.4: Variation of the reflection, transmission and capture coefficients with input velocity as a function of V_i calculated at $t = 400$. Here, $A = 0.3$, $l = 2$ and $x_0 = \pm 10$.

with the condition $R + T + C = 1$(if the defect is conservative) and $P = \int_{-\infty}^{+\infty} |\psi|^2 dx$ being the power of the input soliton. The width h is taken to be eight times the width of the real part of the $\mathcal{PT}$ potential.

Soliton-defect interaction is studied by numerically integrating Eq.4.1 using standard finite-difference beam propagation method. We fix the amplitude A of the input soliton(also the input width) and vary the velocity of the impinging soliton for varying magnitude of the imaginary part of the potential V_i. Thus transiting the defect from a $\mathcal{PT}$ unbroken to $\mathcal{PT}$ broken state, the RTC coefficients are calculated for sufficiently large propagation distances(allowing the soliton to emerge after the interaction).

We first consider the $l = 2$ defect. The $\mathcal{PT}$-breaking for this potential occurs at $V_i = 1.2$(as seen in chapter 2)when $V_r = 1$. Throughout this study the amplitude of the defect is fixed to be $V_r = 1$ unless specified otherwise. The fundamental soliton with hyperbolic secant profile and amplitude $A = 0.3$(width $\simeq 3.3$) is incident separately on to the $\mathcal{PT}$-symmetric defect from the gain side and the loss side. After sufficient propagation time, the RTC coefficients are calculated for different incident velocities. Fig.3.1 shows a typical profile for the RTC coefficient for varying velocities for two different V_i; one far below the $\mathcal{PT}$ breaking and the other near to the $\mathcal{PT}$ breaking. Solid lines correspond to dynamics when soliton beam is incident from the left and dashed lines correspond to dynamics when soliton is incident from the right. For very low V_i value, the dynamics for the beams incident from left or right is invariant(curves with $\square$), whereas for large V_i this invariance is broken and the dynamics shows a nonreciprocal behavior for increasing velocity(dashed line with $*$), i.e., with increasing angle of incidence. For example, for velocity $v_{inc} = 0.2$, the beam behavior changes from total reflection to total transmission(capture coefficient is negligible) depending on from which side of the defect the beam is incident on. The propagation dynamics(Intensity($|\psi|^2$) evolution in the x-t

plane) for the three representative V_i values are shown in Figs.3.2 and 3.3 where we have employed the standard beam propagation method.

The dependence of RTC coefficients as a function of V_i and velocity v_{inc} is shown in Fig.3.4. It is clearly evident that as V_i increases, the soliton-defect interaction can change from reciprocal to non-reciprocal behavior for increasing velocities(Figs.3.1-3.4). Moreover, the dynamics for a fixed V_i can change from total reflection to total transmission with increasing velocity, for example, the $V_i = 0.7$ case in Figs.3.2 and 3.3. The effect can be attributed to the transition of the system towards the $\mathcal{PT}$ broken state. As can be seen in Fig.3.1, the amplitude of the reflection coefficient increases with increasing V_i when the soliton is incident from the gain region, but a much narrower reflected beam(than the incident beam) is obtained. Whereas both the reflected and transmitted beams experience attenuation when the beam is incident from the loss side of the defect; a broader output beam is obtained.

With increasing amplitude A of the input soliton, i.e., with narrower input beams, the RTC coefficients have a much complex behavior. The beam when incident from the gain side gets significantly amplified and experiences multiple reflections(multiple emissions from the defect for low input velocities) together with capturing but no transmission, as seen in Fig.3.5. Whereas, when the incidence is from the loss side, a part of the beam gets captured and the other part gets transmitted together with amplification in beam power on propagation. It is to be noted that no part of the beam is reflected. We consider the case when $A = 1.5$. The input soliton has a width of 0.67, i.e., the soliton width is less than the width of the defect which is equal to one. Fig.3.5 shows typical propagation dynamics of the beam for two different V_i values. The observed complex scattering dynamics can be attributed to the system being near the exceptional point. To demonstrate this, we study the soliton-defect

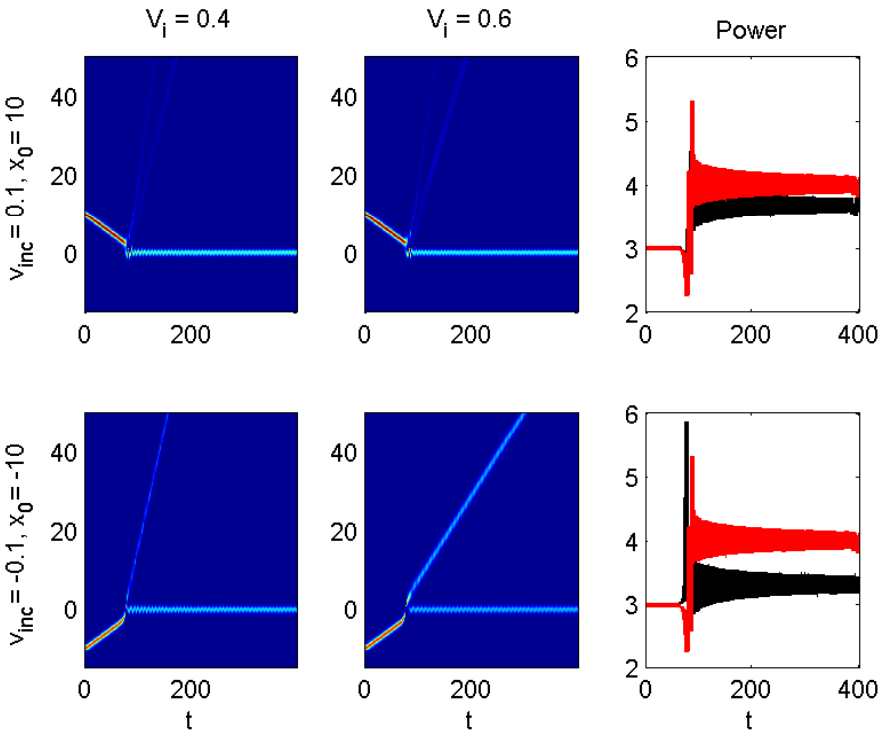

Figure 3.5: Intensity evolution (normalized at each t) in the plane x-t depicting the scattering dynamics of the impinging soliton for various V_i as marked for input velocity $v_{inc} = 0.1$. The last column shows the corresponding power evolution verus t, with the top curve (red) for high V_i and bottom curve (black) for low V_i. Here, $l = 2$, $A = 1.5$ and $x_0 = \pm 10$.

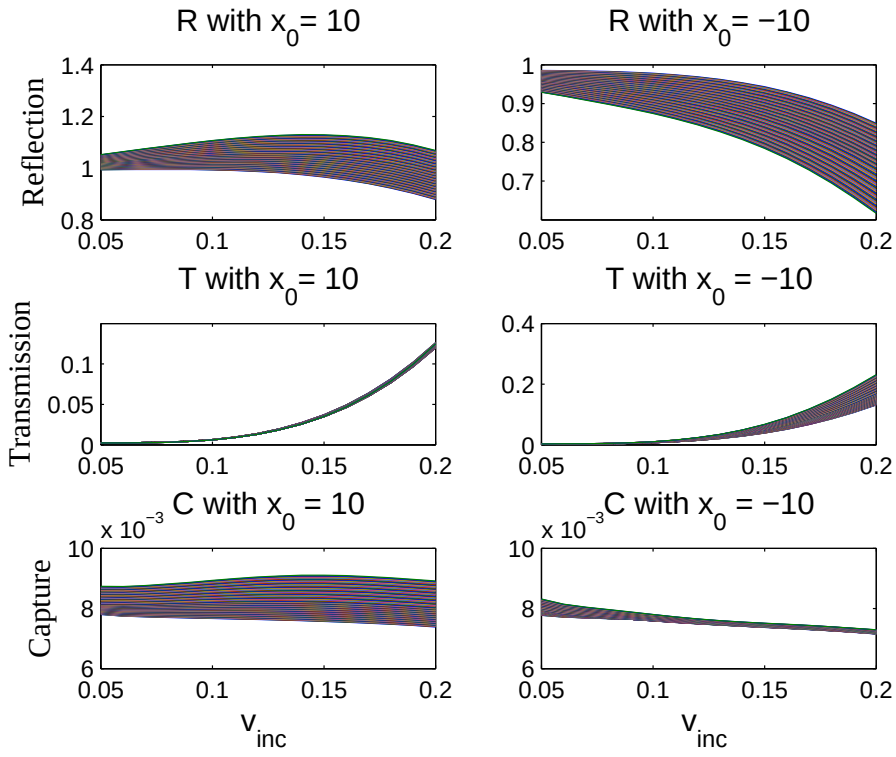

Figure 3.6: Variation of the reflection, transmission and capture coefficients with input velocity as a function of V_i calculated at $z = 400$. Here, $A = 0.3$, $l = 8$ and $x_0 = \pm 10$.

interaction for $l = 8$; in this case, the exceptional point is at $V_i = 4.2$(we obtained in chapter 2). Fig.3.6 plots the RTC coefficients for varying V_i values and is conspicuous by the absence of non-reciprocal behavior for any value of V_i as the defect is always below the exceptional point.

3.3 Summary of the chapter

We have analyzed the scattering of soliton by a $\mathcal{PT}$ symmetric defect, specifically studying the influence of the transverse profile of the imaginary component of the $\mathcal{PT}$-symmetric defect. We have demonstrated that, when the defect approaches the $\mathcal{PT}$-breaking point, the interaction of the soliton beam with the defect results in either transmission or reflection depending on the launch position of the beam i.e., whether the soliton is on the gain side or the loss side of the defect. The transition from reciprocal to non-reciprocal and vice versa can be obtained by varying the angle of incidence, i.e., the velocity of the input beam. Such a behavior is obtained near the exceptional point and is not seen for defects far below the $\mathcal{PT}$-breaking point. Variational analysis of soliton scattering by a $\mathcal{PT}$ symmetric potential in a 1D Bose-Einstein condensate(beyond mean field theory) has been done in chapter 5.

4

Existence, stability and dynamics of $\mathcal{PT}$ symmetric bright soliton in a repulsive BEC

Bright solitons supported by the complex potential in a BEC with repulsive interaction between the atoms of the condensate in a reduced 1D setting is discussed in this chapter. The localization is provided by the $\mathcal{PT}$-symmetric potential whereas the defocusing nature of nonlinearity tries to destroy the wave localization. Hereafter, the term bright solitons is used for these localized nonlinear waves with reference to their spatial shape, even if the confinement is actually provided by the $\mathcal{PT}$-symmetric potential. Even though all discussions are referred to the BEC case, generalization to the optical case is straightforward due to the correspondence between the two governing equations in the corresponding media: the NLSE and the GPE, respectively. The form of trapping potential is same as used in chapter 2. i.e., the BEC is harmonically trapped in two spatial dimensions, and is subjected to a super-Gaussian potential in the third spatial direction. A super-Gaussian profile for the trapping potential allows us to vary the trapping potential from a Gaussian to a square-well. Furthermore, the BEC interacts with the local environment by adding a potential profile accounting for gain and loss in the system. BEC behavior

in a $\mathcal{PT}$ symmetric potential encompassing a super-Gaussian profile and attracting inter-particle interaction has been described in chapter 2. In the repelling case discussed here, the $\mathcal{PT}$-symmetric complex potential is strong enough to compensate the effect due to linear diffusion and the reciprocal repulsion between the atoms below the exceptional point, whereas above the exceptional point self-localization is inhibited by the nonlinear effects. $\mathcal{PT}$ symmetric bright solitons in a self-defocusing nonlinearity have been discussed in a Scarff II trapping potential[106, 177], Rosen-Morse potential[178] and in a parabolic trapping potential[179, 180]. The last two potentials do not possess a $\mathcal{PT}$-breaking point. All these studies briefly discussed the existence of solitons, without going into details of stability range and existence curves with respect to the amplitude and transverse profile of the considered complex potential.

The derivation of the GPE and its form in reduced 1D BEC are discussed in chapters 1 and 2 and here, the GPE for repulsive condensate trapped in $\mathcal{PT}$ symmetric super-Gaussian potential is studied.

4.1 Mathematical formulation

At temperatures $T < T_c$(T_c is critical condensation temperature) and in dilute limit, i.e., the scattering length, a, is much less than the mean interparticle spacing, the evolution of BEC is well described by the GPE. Usually, the BECs are modeled inserting a harmonic potential modeling the trap for atoms, whereas the two particle interaction in the simplest case is described by a Kerr-like cubic nonlinearity. The flexibility of selecting trapping frequencies in each spatial direction determines the shape of the condensate: spherical, disk-shaped or cigar shaped condensates can be generated[181]. Such BEC systems in reduced dimensions have been studied earlier[182, 183]. The normalized one-dimensional GPE governing

the dynamics of the condensate is,

$$\imath\frac{\partial u}{\partial t} = -\frac{1}{2}\frac{\partial^2 u}{\partial x^2} + |u|^2 u + V(x)u, \tag{4.1}$$

with the time coordinate normalized as $t = Tw_\perp$ and the spatial coordinate as $x = X/a_\perp$, where, $w_\perp$ is the harmonic oscillator frequency in the transverse (Y, Z) direction and $a_\perp = \sqrt{\frac{\hbar}{mw_\perp}}$, with m the atomic mass.

In Eq.4.1, due to the sign of the nonlinear term, we are considering a positive scattering length resulting in repulsive interactions between the particles. For the trapping potential, we take $V(x)$ to be complex, i.e., $V(x) = V_R(x) + iV_I(x)$. We also assume that the potential is $\mathcal{PT}$-symmetric, therefore possessing a symmetric real part and an anti-symmetric imaginary part such that the potential obeys the necessary (but not sufficient) condition for possessing real eigenvalues, i.e., $V(x) = V^*(-x)$. The real part of the trapping potential is chosen to be of super-Gaussian form, i.e.,

$$V_R(x) = -V_r \exp(-x^{2l}). \tag{4.2}$$

The imaginary part of the potential is chosen such as to enable a complete understanding of flux of particles associated with $\mathcal{PT}$ potentials as detailed in chapter 2. The two different types of transverse profiles considered are,

$$\text{potential A: } V_I(x) = -V_i x^{2l-1} \exp(-x^{2l}), \tag{4.3}$$

and

$$\text{potential B: } V_I(x) = -V_i x \exp(-x^2). \tag{4.4}$$

According to their definitions, for type A, the transverse profile of V_I is proportional to the first derivative of V_R inverted in sign, thus it changes with the profile of V_R as l varies; for type B the profile does not depend on V_R, and it is chosen as a Hermite(super)-Gaussian function of first order.

4.2 Stationary solutions in the linear and nonlinear regime

The ground state stationary solutions of Eq.4.1 can be found making the ansatz $u(x,t) = \phi(x)e^{-i\mu t}$ which results in,

$$\mu\phi = -\frac{1}{2}\frac{d^2\phi}{dx^2} + (V_R + iV_I)\phi + |\phi|^2\,\phi, \tag{4.5}$$

with μ being the chemical potential and $\phi(x)$ being the time invariant transverse profile. For each value of the eigenvalue μ, a corresponding particle number, named $N = \int |\phi|^2 dx$, is associated, providing the nonlinear dispersion relationship for the condensate.

Stationary solutions of Eq.4.5 are found using standard relaxation technique based on Newton-Kantorovich method and pseudospectral differentiation with Fourier differentiation matrices[124]. We seek for bound states for different l and V_i values keeping $V_r = 1$. We recall from chapter 2 that in the linear case(with $V_r = 1$), the potential supports only the fundamental bound state and above a critical value of the imaginary part of the potential, the system ceases to have purely real eigenvalues. This critical point, also known as the $\mathcal{PT}$-symmetry breaking point or the exceptional point of the system, in the super-Gaussian potential occurs at, $V_c \approx lV_r/2 + 1/5$ for potentials of type A, providing $V_c \approx 0.7$ for $l = 1$, $V_c \approx 1.3$ for $l = 2$ and $V_c \approx 2.5$ for $l = 4$. For the potential of type B, the transition occurs at $V_c \geq V_r$ for $l \geq 2$ ($l = 1$ is analogous to type A), then undergoing small increases as l gets larger ($V_c \approx 1$ for $l = 2$ and $V_c \approx 1.2$ for $l = 4$).

Let us now study the stationary solutions in the nonlinear case when nonlinearity is defocusing, i.e., the higher the particle density the higher the potential is. Typical profiles of the solitons obtained numerically are depicted in Fig.4.1 for the two different potentials. The complex part of the

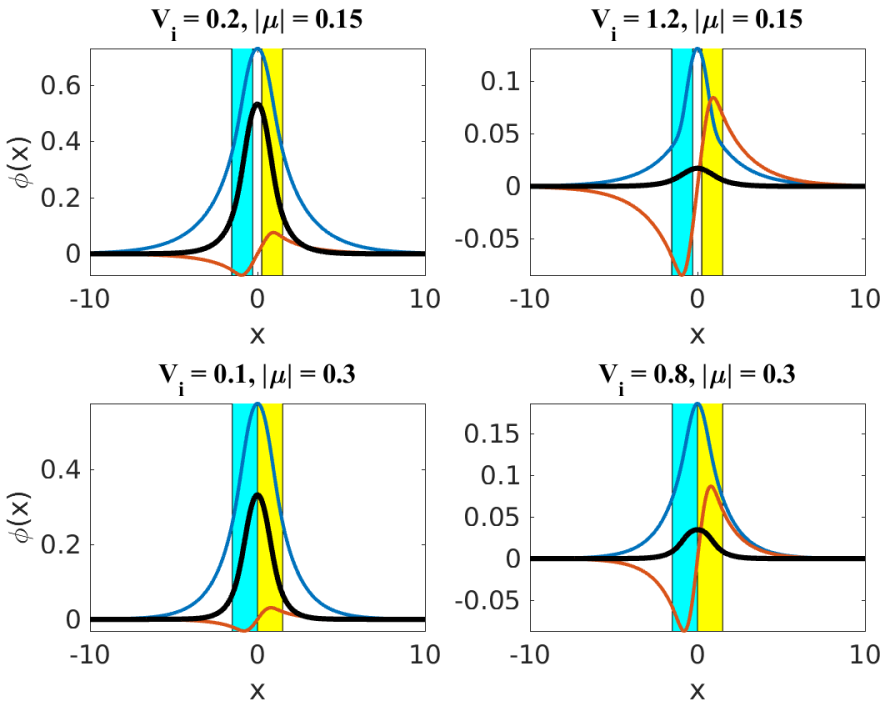

Figure 4.1: Typical solution profile for the two kinds of potential for $l = 2$ and different V_i values as marked. The symmetric curves represent the real part (blue curves) and the density distribution (black curves) of the solution, corresponding to the higher and to the lower amplittude, respectively. The asymmetric profile represents the imaginary part of the solution. The shaded area corresponds to the loss (cyan) and gain (yellow) regions. (Top row) Potential A: The particle number N for the two cases are 1.29 and 0.05, respectively. (Bottom row) Potential B: The particle number N for the two cases are 0.71 and 0.08, respectively. It can be seen that the magnitude of the imaginary part of the solution increases with V_i. Throughout the chapter the real part of the potential is taken as $V_r = 1$.

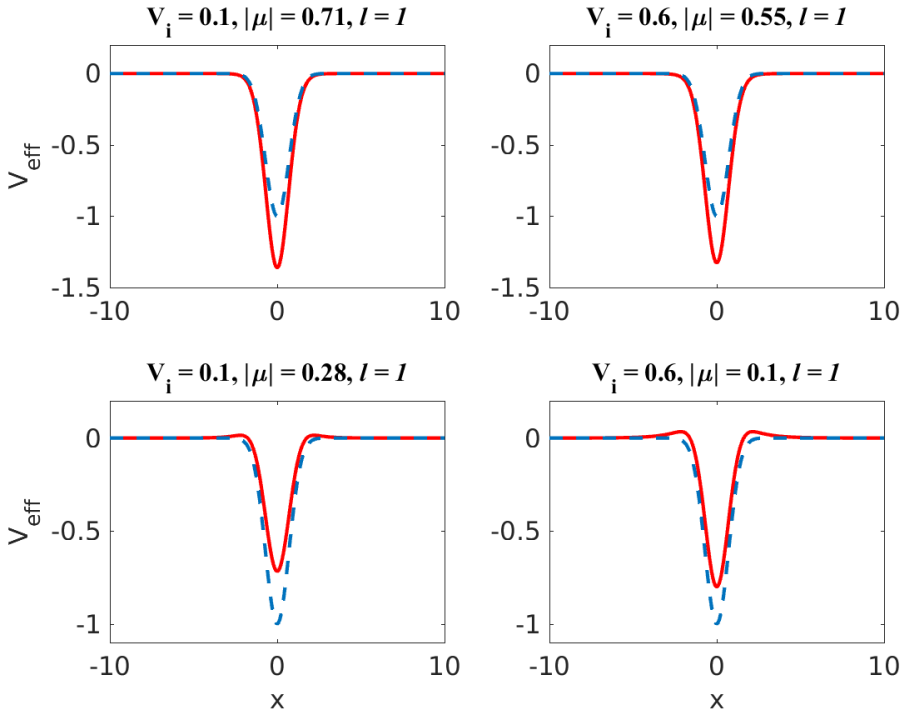

Figure 4.2: Comparison between focusing and defocusing nonlinearity in the presence of the same $\mathcal{PT}$-symmetric potential $V(x)$ with $l = 1$. Transverse profiles of the effective potential V_{eff} (solid lines) together with the $\mathcal{PT}$-symmetric potential V_R (dashed lines) for the focusing (top row) and defocusing (bottom row) nonlinearity; the particle number N is the same in the two cases and equal to 0.62. Left and right column correspond to $V_i = 0.1$ and $V_i = 0.6$, having a linear eigenvalue μ equal to -0.47 and -0.29, respectively. The nonlinear eigenvalue μ differs between the focusing and the defocusing case owing to the different overall potential acting on the condensate.

potential heavily affects the shape of the nonlinear stationary solutions: in fact, a time-invariant solution can be found only in the presence of a balance of the particle flux, the latter clearly depending on the spatial profile of the particle source-sinks. For a fixed shape of $V_I(x)$, an increase in the amplitude of the imaginary part V_i corresponds to an increase in the imaginary part of the soliton. Moreover, there is an upper cut-off for μ for any given pair V_i and l: Nonlinear shape-preserving solutions cease to exist above this cut-off value. This can be easily seen by analyzing the overall effective potential $V_{eff} = V_R \pm |\phi|^2$, the plus and minus sign corresponding to defocusing and focusing nonlinearity, respectively. Typical behavior is plotted in Fig.4.2. For the same particle number N, a focusing nonlinearity makes the overall potential V_{eff} deeper than the linear one: in this case, the eigenvalue μ spans from the linear value dictated by $V(x)$ to minus infinity for $N \to \infty$. In the defocusing case, the nonlinearity makes the overall potential V_{eff} shallower than the potential $V(x)$, and the nonlinear eigenvalues increase from the linear value to zero as N grows up. In fact, when V_{eff} is positive, wave trapping(i.e., bound states) is not observed. Particle number N versus the chemical potential μ are plotted in Fig.4.3 for various V_i values. With increasing V_i, the existence region of the solutions decreases.

Fig.4.4 summarizes the essential features of the fundamental soliton versus V_i for the defocusing nonlinearity. It reveals that no soliton solution exists above the $\mathcal{PT}$-breaking point, which is in sharp contrast with the focusing case(in chapter 2), where a nonlinear bounded solution always exist, irrespectively of the magnitude of V_i, i.e., even if the corresponding linear system is in the $\mathcal{PT}$-breaking point. The behavior can be explained with reference to the transverse flux of particle from the gain to the loss zone. To ensure a large enough migration of particles, the field must be trapped enough around the origin. Whereas in the attractive case

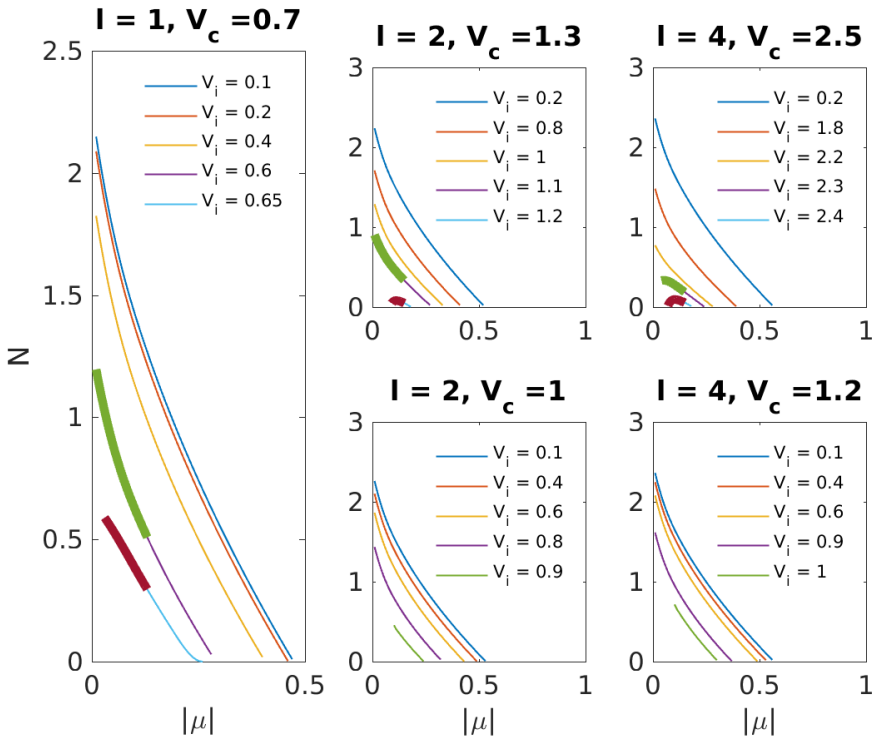

Figure 4.3: Particle number N versus μ existence curve for potentials of type A (top row) and of type B (bottom row). Each panel corresponds to a different l as labeled, whereas each curve corresponds to a value of V_i whose magnitude increases from top to bottom curves. The thicker lines represent the region where the solutions are unstable.

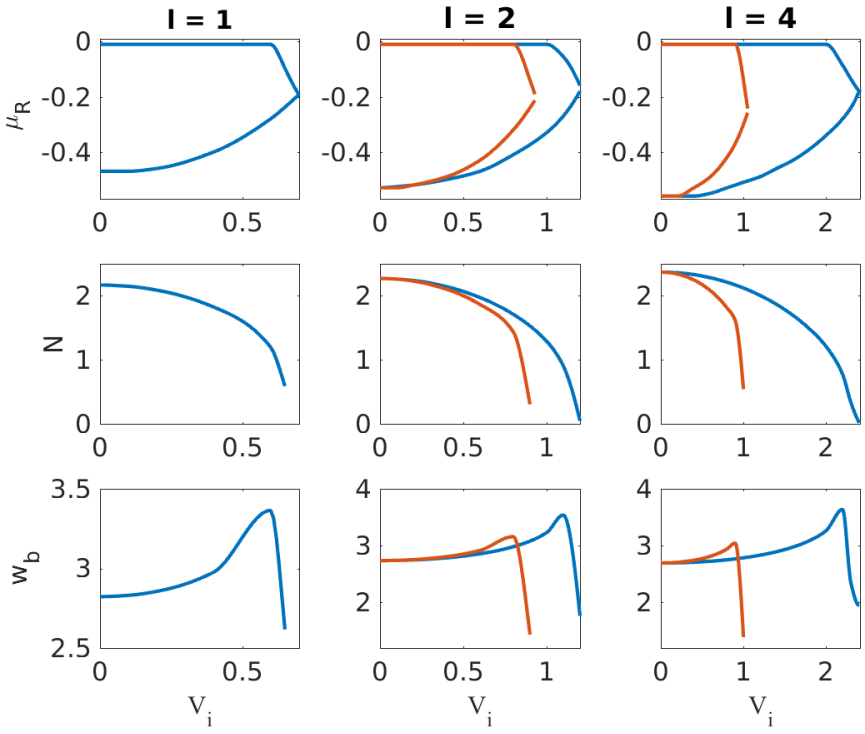

Figure 4.4: Overview of the soliton properties versus the $\mathcal{PT}$-symmetric potential for three different values of l. First row: Nonlinear spectrum of the condensate versus the magnitude of the imaginary potential V_i, plotted when the eigenvalue μ is real. Bottom curves are the minimum μ, thus corresponding to the linear case. Top lines report the maximum μ achievable for a fixed linear potential. Second (third) row: number of particles N (beam width w_b) corresponding to the first row for the maximum N supporting self-localization. In every panel the inner curves correspond to potentials of type B and outer curves to potential of type A, respectively.

the nonlinearity helps the confinement and it is always able to avoid the $\mathcal{PT}$-breaking. In the case of particle repulsion, the field confinement is contrasted by the nonlinearity.

In the defocusing case, soliton exists inside a finite band of the chemical potential, as explained above(Fig.4.2). The bottom edge of the band corresponds to the linear case, in turn depending both on l and V_i. Specifically, the larger V_i is owing to the smaller spatial confinement[140]. The maximum value of μ is usually zero, but it becomes negative in proximity of the exceptional point due to the appearance of large tails in the soliton profile(Fig.4.2). Moreover, the upper and lower edges of the allowed spectrum converge as V_i increases(first row in Fig.4.4): for V_i corresponding to the breaking of the $\mathcal{PT}$ symmetry, the interval degenerates into a single point for high l. Oppositely to self-focusing nonlinear media, for a given μ, the required N decreases with increasing magnitude of the imaginary part of the potential, in order to increase the spatial localization and compensate the flux. This holds true also for the particle number N corresponding to the maximum achievable $\mu_R = \text{Real}(\mu)$(the second row in Fig.4.4). It has to be noted that, in the limit $N \to 0$, the mean field approximation is no more valid. The width of the solitons defined as $w_b = \sqrt{\int x^2|\phi|^2dx / \int |\phi|^2dx}$ also shows an increasing behavior with V_i: in fact, for large V_i the nonlinear solutions do not maintain a Gaussian-like transverse profile due to the lateral peaks appearing in the effective potential(second row in Fig.4.2). Finally, the interval of V_i ensuring soliton existence, going from zero to the linear exceptional point, is larger for potentials of type A than for potentials of type B. When the parameter l increases, solitons exist for larger values of V_i due to the lower amount of flux to compensate the inhomogeneous gain/loss.

4.3 Linear Stability Analysis

We now proceed to address the stability of these stationary solutions upon small perturbations. For this we make use of the linear stability analysis(LSA) and perturb the stationary solution as

$$u = [\phi + a(x,t)] \exp(-i\mu t), \tag{4.6}$$

where $a(x,t) = p(x)\exp(i\lambda t) + q(x)\exp(-i\lambda^* t)$, with $p(x)$ and $q(x)$ being the eigenfunctions of the linearized eigenvalue problem. Substituting Eq.4.6 in Eq.4.1 and linearizing with respect to a, it yields the eigenvalue problem

$$\lambda \begin{bmatrix} p \\ q^* \end{bmatrix} = \begin{bmatrix} L_1 - iV_I(x) & -\phi^2 \\ (\phi^*)^2 & -L_1 - iV_I(x) \end{bmatrix} \begin{bmatrix} p \\ q^* \end{bmatrix}, \tag{4.7}$$

where $L_1 = \mu + \frac{1}{2}\frac{d^2}{dx^2} - 2|\phi|^2 - V_R$. A solution is linearly stable if $\mathrm{Im}(\lambda)$ is equal to zero for all λ. The differential operators are discretized using pseudospectral method based on Fourier differentiation matrices[124]. The eigenvalue problem is implemented in MatLab and the eigenvalues and eigenfunctions of discretized version of Eq.4.7 are obtained using the *eig* function. A grid of $[-40, 40]$ with number of points 1002 was chosen along x. According to the set of eigenvalues λ found from Eq.4.7, solitons can show three different responses to noise, in turn determining the stability of the solution. First, if all the eigenvalues are purely real, the given soliton is linearly stable. Second, if at least one of the eigenvalues is purely imaginary, the soliton shape is destroyed in evolution due to the exponential amplification of the initial noise with time. Finally, if eigenvalues are complex, i.e., with non-zero real part and the eigenvalues appear as quartets, oscillatory instability(OI) is observed[184].

LSA predicts stable solutions for both the potentials until $V_i = 0.5V_c$. For higher V_i, LSA predicts OI for both the families of potentials. Impor-

tantly, instability is predicted even for solutions in proximity of the linear limit, suggesting the presence of numerical artifacts in the LSA results. Even though the predicted instability values are small(in the range of 10^{-3}), they are not negligible when compared to the numerical accuracy. The corresponding eigenfunctions spread all over the numerical integration domain. All of these features suggest that the discretization of the grid leads to spurious results, the effect being particularly relevant close to the exceptional points. For example, for potential A, with $l = 4$, $V_i = 2.4$ and $\mu = -0.18$, the stationary solution is a low amplitude solution with $N \to 0$, i.e., the linear limit. Stationary solutions in the linear limit should be stable, but the LSA predicts an unphysical unstable behavior. Thus, all the LSA must be checked and compared with numerical simulations of the original system in the presence of noise. Accordingly, the unstable regions confirmed together with direct numerical integration of Eq.4.1 are marked by thicker lines in Fig.4.3. The details of the numerical analysis are discussed in the next section.

Looking at Fig.4.3, for defocusing nonlinearity solitons supported by potential B never shows instability for $l > 1$, whereas for potential A instability appears for V_i close to V_c and at the edge of the soliton existence region, i.e., for $|\mu| \to 0$.

4.4 Dynamical evolution

We numerically solve Eq.4.1 using the operator splitting technique. For the generic evolution equation,

$$u_t = \hat{A}u + \hat{B}u, \tag{4.8}$$

the solution $u(t + \Delta t)$ at time $t + \Delta t$ can be computed starting from $u(t)$ by using different splitting methods. In our case, operators $\hat{A}$ and $\hat{B}$ correspond to the diffusion term and to the overall effective potential

V_{eff}. For the diffusion term, the Crank-Nicolson scheme was utilized. According to the chosen splitting method(Lee, Strang or SWSS), the form solution can be obtained and is given in chapter 1. Due to the non-Hermitian nature of the system, numerical convergence strongly depends on the underlying operator splitting method used. For a conservative system(as well as for $V_i \ll V_c$), a simple Lee splitting with a first order accuracy is sufficient to achieve numerical convergence. As detailed below, in our case the dynamics of the condensate requires the symmetrically weighted sequential splitting (SWSS), which is second order accurate. We also employed the Strang method, encompassing a second order accuracy as well. Nonetheless, the Strang method fails for V_i values close to the exceptional point.

To illustrate the differences, we simulate the evolution of the stationary solution for fixed parameters with the three different methods for the case of potential A with parameters $l = 4$ and $V_i = 2.4 \approx V_c$. The results are shown in Fig.4.5. Note that in this case the gain-loss region is in a narrow region of the solution(the shaded regions). The numerical grid is [-30 30] with the number of points in the transverse direction $n_x = 5001$ and the time step $\Delta t = 1 \times 10^{-4}$. The evolution is studied until $t = 300$ with absorbing boundary condition. For both the Lee and Strang splitting the numerical noise accumulates on propagation and the solution becomes unstable after $z = 130$. For the SWSS case, for the same numerical parameters, the stationary evolution of the solution survives on longer distances. To address the stability of the obtained solutions, the stationary state is perturbed by an additive random Gaussian noise of magnitude 5% of the solution amplitude. The perturbed profile is now taken as the input for the numerical code with SWSS splitting. The field at short times smooths out its profile, but at the same time an oscillation between two different states develop. In other words, an internal mode of the soliton is

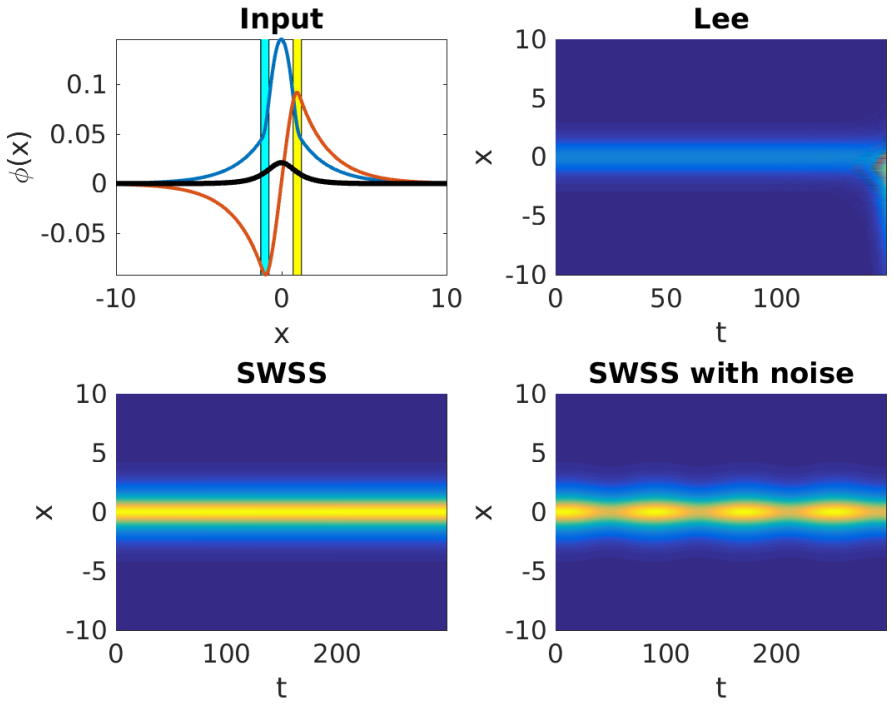

Figure 4.5: First panel shows the profile of the input stationary state for Potential A with $l = 4$, $V_i = 2.4$ and $\mu = -0.15$. The symmetric curves represent the real part of the solution (blue curve) and the density distribution (black curve), corresponding to the higher and to the lower magnitude, respectively. The asymmetric profile (red curve) represents the imaginary part of the solution. The shaded area corresponds to the loss (cyan) and gain (yellow) regions. The dynamical evolution of the stationary solution for different operator splitting method, as marked in the title, is shown in the other panels. For the same numerical parameters SWSS is more accurate than the other methods. The unstable dynamics of the solution in the presence of noise is depicted in the last panel. The initial solution is perturbed with a 5% Gaussian noise. Here $V_c \approx 2.5$

excited[145].

We carried out a systematic analysis of the evolution dynamics of the stationary states to compare with the instability predicted from LSA. We start with the case $l = 1$ where both the kinds of potentials are equivalent. In this case the transition from the gain to the loss region is continuous, i.e., there are no appreciable gaps around $x = 0$, as depicted by the shaded area in Fig.4.6. An unstable μ is chosen from the existence curve plotted in Fig.4.3. The soliton undergoes instability, as shown by the breathing-like behavior shown in Fig.4.6.

Summarizing, for low V_i, the condensate remains stable upon evolution for time scales much larger than characteristic diffusion range, $t_d = 0.5w_b^2/w_\perp$, i.e, time required by the condensate to broaden by a factor of $\sqrt{2}$ with respect to its original size. Finally, with increasing V_i, the condensate becomes unstable for a narrow range of $|\mu|$ for potential A whereas for potential B the condensate remains stable for all V_i values.

To compare our results with experimental repulsive BEC systems we consider two different BECs. For a BEC with ^{87}Rb [185] containing about $N_0 = 1500$ atoms, trapped in a harmonic potential with frequencies $\nu_\perp = 408$Hz, $\nu_x = 63$Hz, s wave scattering length $a = 95a_0$, a_0 is the Bohr radius, $a_\perp = 1.36\mu$m, diffusion time $t_d = 0.1$ms for a beam of width $w_b = 0.8$. Hence $t = 200$ in the normalized frame corresponds to $1.6 \times 10^6 t_d$. Similarly, for repulsive BEC with ^{87}Rb [186], $N = 1.5 \times 10^5$ and $\omega_\perp = 2\pi \times 425$Hz gives $t_d = 0.2$ms and hence $t = 200$ corresponds to $1.7 \times 10^6 t_d$.

4.5 Summary of the chapter

To conclude, we have addressed the existence and stability of stationary states of BEC with repulsive nonlinearity, the latter being trapped in a

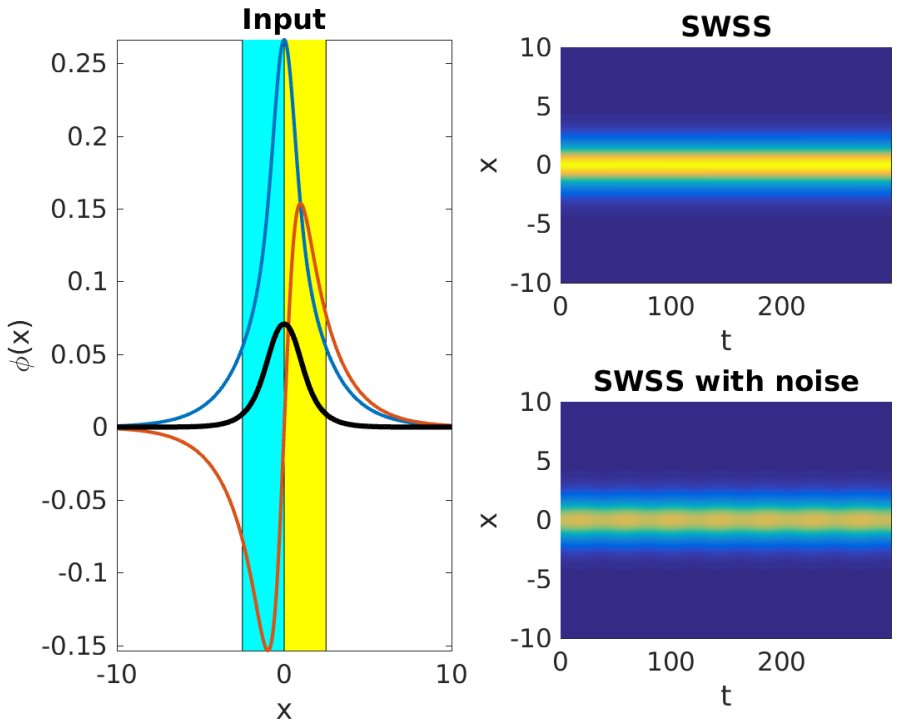

Figure 4.6: First panel shows the profile of the input stationary state for $l = 1$, $V_i = 0.65$ and $\mu = -0.12$. The symmetric curves represent the real part of the solution (blue curve) and the density distribution (black curve), corresponding to the higher and to the lower magnitude, respectively. The asymmetric profile (red curve) represents the imaginary part of the solution. The shaded area corresponds to the loss (cyan) and gain (yellow) regions. The dynamical evolution of the stationary solution using SWSSS is depicted with and without the inclusion of noise. The initial solution is perturbed with a 5% Gaussian noise. Here $V_c \approx 0.65$.

super-Gaussian $\mathcal{PT}$-symmetric potential. We demonstrate that the existence region greatly depends on the transverse profile of the gain-loss mechanism. For concreteness, we elaborated the ideas using the Gross-Pitaevskii equation with repulsive interaction between the atoms of the condensate, although the model can be applied to any nonlinear system including optics, acoustics and so on. We considered a cigar shaped condensate and studied the interplay among diffusion, repulsive nonlinearity and gain-loss mechanism on the existence of the matter wave solitons. The effects of different gain-loss profiles are further analyzed by considering two different types of transverse profiles for the imaginary part of the $\mathcal{PT}$-symmetric potential. In contrast with focusing media, where the nonlinearity is able to transit the system from a $\mathcal{PT}$-broken state (linear regime) to $\mathcal{PT}$-unbroken state (nonlinear regime), with the defocusing nonlinearity this transition does not occur. Thus, solitons do not exist above the linear exceptional point. $\mathcal{PT}$-symmetric matter wave solitons are found to be always stable when the transverse profile of the imaginary part of the complex potential remains invariant with the change in the real potential, i.e, potentials of type B. The complex potentials belonging to type A, whose imaginary part changes together with the real part, are found to support unstable solitons in proximity of the exceptional point(fixed by the linear potential) and at the edge of the soliton existence region versus nonlinear excitation.

5

Dynamics of BEC with $\mathcal{PT}$ symmetry beyond mean field theory.

We have seen in the previous chapters how the gain/loss mechanism(via modifying the form of trapping potential in to complex form) affects the properties of BEC by analyzing the ground state solution of the GPE. In this chapter, we are studying the collective excitations in the same system, i.e., in quasi 1-D BEC trapped in $\mathcal{PT}$ symmetric potential. Collective excitations represent a phenomenon that occurs within the macroscopic system consisting of a large number of interacting bosons and found that it is a successful tool for the investigation of the properties of BEC. The collective modes can be generated in BEC by different ways, one among them is varying the geometry of the trapping potential[187–193] and another by the modulation of the s-wave scattering length via Feshbach resonance[194–199]. The frequencies of collective excitations in dilute BEC have been measured experimentally for the first time at JILA[187]. It is noted that experimentally measured excitation frequencies[187, 189] match with the theoretical predictions[200–204]. Because of the nonlinearity in the BEC system, collective excitations show frequency shifts[197, 205–207], mode coupling[205–209], damping[188, 210] and also collapse and revival of oscillations[205, 211, 212]. Collective excitation interferometry that uses to sense the rotation using collective modes

of an interacting Bose-Einstein condensate[213]. The appearance of 1-D feature shown by experiments[214–216] on trapped Bose gases at low temperature paved more attention on collective excitations. The collective excitations of a one-dimensional Bose-Einstein condensate trapped in an anharmonic potential is studied in[217, 218]. The collective excitations of low-dimensional Bose-Einstein condensates with two and three body interactions in anharmonic potentials are detailed in[219]. The transition temperature, the depletion of the condensate atoms, and the collective excitations of a BEC with two and three-body interactions in an anharmonic trap at finite temperature are studied in[220].

Since the present thesis mainly concentrates on the effects of complex trapping potential(or we can say the gain/loss mechanism), it is also worthwhile to notice how the collective phenomena are affected by these type of complex trapping potential. In addition, we have considered the beyond mean field correction theory. Most of the theoretical works in $\mathcal{PT}$- symmetric BEC were detailed in the mean free field limit of GPE where a pure condensate is assumed. Such an explanation is inadequate and failed to follow the experimental values[221] when 1) the interaction with the environment is considered 2) the number density is high and 3) the dimension of the system is considered[222, 223]. Description of systems with these additional features and also trapped in $\mathcal{PT}$ symmetric potential needs detailed discussion.

Interactions among the particles of quantum degenerate gases play a major role in altering their features[24, 123]. These interactions in dilute gases are mainly binary and treated with an s wave scattering approach and the s wave scattering length, a characterizes the strength of interactions.

The present chapter deals with the collective excitations in BEC trapped in a $\mathcal{PT}$ symmetric potential with mean field correction terms added to

GPE. We use a Gaussian type of single well potential[224]. The Gaussian single well potential can be experimentally implemented[96, 97, 132]. We employ variational approach[143, 144, 217] to find out the excitation frequencies. In order to compare the results in purely real trapping potential and in complex $\mathcal{PT}$ potential, we consider two cases: 1) The real part of the potential is treated first, and then 2) the complex $\mathcal{PT}$ symmetric potential has been considered. In the former case, the motions of the center of mass and condensate width are coupled. But in the latter case, in addition to these, we have to consider the velocity of the center of mass also which plays a great role in determining the collective excitation frequencies.

We give a suitable theoretical model for 1-D BEC in a $\mathcal{PT}$ symmetric Gaussian potential in section 5.1. Variational approach to non-Hermitian system and evolution equations for variational parameters are obtained in section 5.2. The collective excitation frequencies of the system with the real part of the trapping potential and with complex $\mathcal{PT}$ symmetric potentials are separately discussed in 5.3, scattering of the soliton by the $\mathcal{PT}$ defect is studied in section 5.4 and finally concluded in 5.5.

5.1 Theoretical Model

In the mean field approximation, the BEC obeys the GPE[24, 123],

$$i\hbar\frac{\partial\psi}{\partial t} = -\frac{\hbar^2}{2m}\nabla^2\psi + g\left|\psi\right|^2\psi + V_{ext}(\mathbf{R})\psi, \tag{5.1}$$

with m is the atomic mass, $g = 4\pi\hbar^2 a/m$, a the scattering length, V_{ext} the trapping potential and $\mathbf{R} = (X, Y, Z)$ is the spatial coordinate. Here the interaction considered is only binary and it can be modified by including higher order correction terms. Hence, we start with three dimensional GPE with two, three body interactions and the mean field correction

terms[225–227],

$$\begin{aligned} \imath\hbar\frac{\partial\psi}{\partial t} =& -\frac{\hbar^2}{2m}\nabla^2\psi + V_{ext}(R)\psi + \epsilon_g g_0 \left|\psi\right|^2\psi + \epsilon_q q_0 \left|\psi\right|^3\psi \\ &+ \epsilon_p p_0 \psi\nabla^2\left|\psi\right|^2 + \epsilon_\chi\chi_0\left|\psi\right|^4\psi, \end{aligned} \tag{5.2}$$

where, $\epsilon_g = \epsilon_q = \epsilon_p = \epsilon_\chi = \pm 1 : -1$ for attractive interaction and $+1$ for repulsive interaction. $g_0 = 4\pi\hbar^2 a_s/m$ term corresponds to two body interaction, $q_0 = 32g_0a^{3/2}/3\sqrt{\pi}$ term[221, 228] corresponds to higher-order correction term to the two-body interaction due to quantum fluctuations(since quantum fluctuations are dramatically enhanced in low dimensional systems), $p_0 = 8\pi\hbar^2 a_s^3/3m$ term[229] corresponds to higher-order correction to the two-body interaction due to shape-dependent confinement and the final term corresponds to three body interaction, strength of which is calculated using effective field theory and for ultracold BECs, it is expressed as $39\pi(4\pi - 3\sqrt{3})\hbar^2 a_s^4/m$[230, 231].

When the trapping frequency in the perpendicular direction is very large compared to that in the x-direction such that the ground state in the perpendicular direction is hard to achieve; hence all atoms are confined in the ground state in the x-direction. Hence a quasi one dimensional case can be achieved. Assuming that the condensate is harmonically trapped in the Y and Z directions and with an axial trap potential $U(X)$ in the X direction, the external trapping potential can be written as $V_{ext} = (1/2)m\omega_\perp^2(Y^2 + Z^2) + U(X)$, with $w_\perp$ being the frequency of atomic oscillations in the radial direction and $U(X)$ is taken to be a Gaussian trap[224] in such a way that it satisfies $\mathcal{PT}$ symmetric conditions in BEC.

We proceed by assuming, $\psi(X, Y, Z, t) = \sigma(X, t)\chi(Y, Z)$, $\sigma(X, t) = \psi\exp\left(\frac{-iCt}{\hbar}\right)$ and $\chi(Y, Z) = (1/a_\perp\sqrt{\pi})\exp(-(Y^2 + Z^2)/2a_\perp^2)$. After substitution and and using the transformation: $t = T/\omega_X$, $a_\perp = \sqrt{\hbar/m\omega_\perp}$,

$x = Xa_\perp$ and $\psi = \psi/\sqrt{2a_s}$. we get,

$$\begin{aligned} \imath\frac{\partial\psi}{\partial T} =& -\frac{1}{2}\frac{\partial^2\psi}{\partial X^2} + g_0\left|\psi\right|^2\psi + U(X)\psi \\ &+ (\epsilon_g\tilde{g_0} - \epsilon_p\tilde{g_0}^{'})\left|\psi\right|^2\psi + \epsilon_q\tilde{q_0}\left|\psi\right|^3\psi \\ &+ \epsilon_p\tilde{p_0}\psi\frac{\partial^2}{\partial X^2}\left|\psi\right|^2 + \epsilon_\chi\tilde{\chi_0}\left|\psi\right|^4\psi, \end{aligned} \tag{5.3}$$

with $U(X) = \alpha X^2 + V_0\exp(-X^2) + iV_iX\exp(-X^2)$, $\alpha = \frac{\omega_x^2}{2\omega_\perp^2}$, $\tilde{g_0} = 1$, $\epsilon_g = \epsilon_q = \epsilon_p = \epsilon_\chi = \pm 1$, $\tilde{g_0}^{'} = 4a_s^2/3a_\perp^2$, $\tilde{q_0} = 64\sqrt{2}a_s/15\pi a_\perp$, $\tilde{p_0} = 4\pi a_\perp a_s^2/3$ and $\tilde{\chi_0} = \chi_0/12\pi^2 a_\perp^4 a_s^2\hbar\omega_\perp$. The first term in $U(X)$ is negligible compared with other two terms as α is of the order of 10^{-4} for the parameters that we take. The imaginary part in the potential refers to the interaction of BEC with the local environment and it is responsible for the influx and outflux of the particles in the system. Fig.5.1 represents the form of the trapping potential, $U(X)$ that we used in the present work.

To be concrete, taking the parameters of quasi-1D ^{7}Li condensate obtained experimentally[100], consisting of $N_0 = 6000$ atoms, with $a = -3a_B$ (a_B is the Bohr radius), $a_\perp = 1.3\mu m$, we have obtained $D_{co} = 0.007 \ll 1$ for $w_x/w_\perp = 1/100$, where $D_{co} = N_0 a w_x/a_\perp w_\perp$ is the cross-over constant, defined such that, if $D_{co} \ll 1$, the dynamics of the condensate can be described by Eq.5.3[232, 233]. Hence for quasi-1D attractive ^{7}Li condensate, $\tilde{g_0} = -1$, $\tilde{g_0}^{'} = 2\times 10^{-8}$, $\alpha = 10^{-4}$, $\tilde{q_0} = -2\times 10^{-4}$, $\tilde{p_0} = 2\times 10^{-25}$ and $\tilde{\chi_0} = 10^{-7}$.

5.2 Variational approach

We use the variational approach developed for dissipative systems[143, 144] for the $\mathcal{PT}$ symmetry and get the solutions of Eq.5.3. The notations used for further steps are $t = T$, $x = X$, $g_0 = (\epsilon_g\tilde{g_0} - \epsilon_p\tilde{g_0}^{'})$, $q_0 = \epsilon_q\tilde{q_0}$,

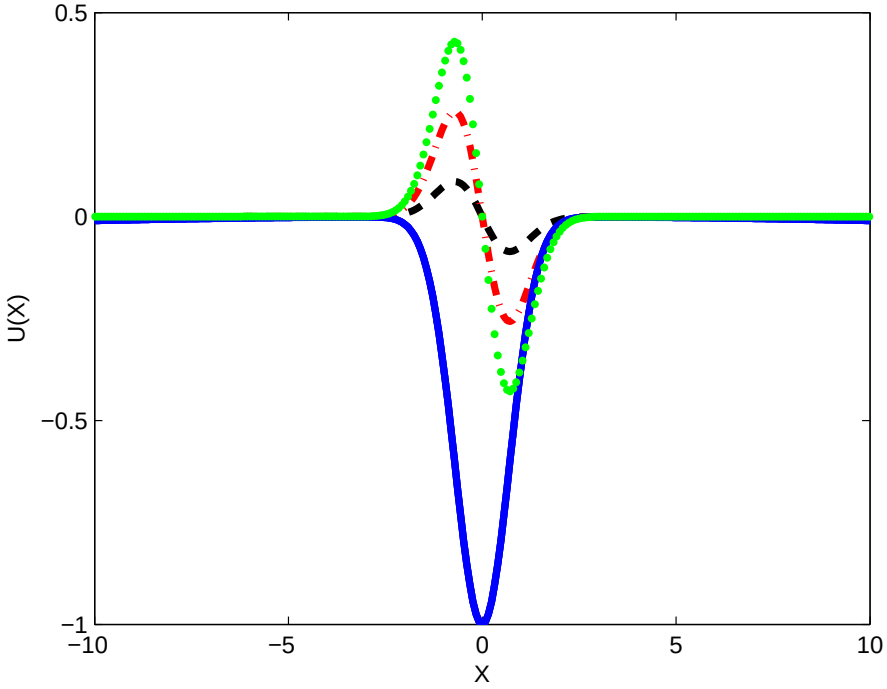

Figure 5.1: The symmetric blue curve(solid) represents the real part of the potential with $V_0 = -1$ and $\alpha = -10^{-4}$. Dashed, dashed dotted and dotted (anti-symmetric) curves are for V_i values: -0.2, -0.6 and -1 respectively.

$p_0 = \epsilon_p \tilde{p_0}$ and $\chi_0 = \epsilon_\chi \tilde{\chi_0}$. Hence the GPE takes the form,

$$\begin{aligned} &\imath\frac{\partial\psi}{\partial t} + \frac{1}{2}\frac{\partial^2\psi}{\partial x^2} - [\alpha x^2 + V_0 \exp(-x^2)]\psi \\ &- g_0 \left|\psi\right|^2 \psi - q_0 \left|\psi\right|^3 \psi - p_0\psi\frac{\partial^2}{\partial x^2}\left|\psi\right|^2 - \chi_0 \left|\psi\right|^4 \psi \\ &= \imath V_i x \exp(-x^2)\psi. \end{aligned} \tag{5.4}$$

We take a trial function of the form[217, 224],

$$\psi(x,t) = A\exp\left[-\frac{(x-\zeta)^2}{2\omega^2} + \imath v(x-\zeta) + \imath b(x-\zeta)^2\right], \tag{5.5}$$

with $A(t)$, $\zeta(t)$, $\omega(t)$, $v(t)$ and $b(t)$ are time dependent variational parameters representing the amplitude, center of mass location with speed and chirp respectively.

The Lagrangian for the GPE includes two terms $L = L_c + L_{nc}$[144], with L_c corresponding to conservative part and L_{nc}, to nonconservative part. L_{nc} is responsible for all the dissipative processes in the system and it is related to the R.H.S of Eq.5.4. Lagrangian for conservative part (L.H.S of Eq.5.4) is obtained and is written as,

$$\begin{aligned} L_c =& \frac{\imath}{2}(\psi\frac{\partial\psi^*}{\partial t} - \psi^*\frac{\partial\psi}{\partial t}) + \frac{1}{2}\left|\frac{\partial\psi}{\partial x}\right|^2 + [\alpha x^2 + V_0 \exp^{-x^2}]\left|\psi\right|^2 \\ &+ \frac{g_0}{2}\left|\psi\right|^4 + \frac{2q_0}{5}\left|\psi\right|^5 + \frac{p_0}{2}\left|\psi\right|^2\frac{\partial^2\left|\psi\right|^2}{\partial x^2} + \frac{\chi_0}{3}\left|\psi\right|^6. \end{aligned} \tag{5.6}$$

Integrating Eq.5.6 across the whole x axis provides the reduced Lagrangian

$\langle L_c \rangle = \int_{-\infty}^{+\infty} L_c dx,$

$$\begin{aligned}\langle L_c \rangle = & -Nv\frac{d\zeta}{dt} + \frac{N}{2}\frac{db}{dt}\omega^2 \\ & + \frac{N}{4\omega^2} + \frac{Nv^2}{2} + Nb^2\omega^2 + \frac{N\alpha}{2}(\omega^2 + 2\zeta^2) \\ & + \frac{V_0 N \exp^{-\frac{\zeta^2}{1+\omega^2}}}{\sqrt{1+\omega^2}} + \frac{g_0 N^2}{2\sqrt{2\pi}\omega} + \frac{2\sqrt{2}q_0 N^{\frac{5}{2}}}{5\sqrt{5}\pi^{\frac{3}{4}}\omega^{\frac{3}{2}}} \\ & - \frac{p_0 N^2}{2\sqrt{2\pi}\omega^3} + \frac{\chi_0 N^3}{3\sqrt{3}\pi\omega^2},\end{aligned} \tag{5.7}$$

where, $N = \int_{-\infty}^{\infty} |\psi|^2 \, dx = \sqrt{\pi} A^2 \omega$ and it is related to the total number of atoms N_0 by $N = 2|a_s|N_0/a_\perp$. For the quasi-1D ^{7}Li condensate $N_0 = 6000$ which gives $N = 1.5$.

The modified Lagrangian equations of motion for the dissipative systems (which accounts for both L_c and L_{nc} terms)[143, 144] ,

$$\frac{d}{dt}\frac{\partial \langle L_c \rangle}{\partial(\frac{\partial \eta}{\partial t})} - \frac{\partial \langle L_c \rangle}{\partial \eta} = 2Re \int Q \frac{\partial \psi^*}{\partial \eta} dx, \tag{5.8}$$

with $Q = \imath V_i x \exp(-x^2)\psi$.

Computing the variations with respect to the parameters, we obtain the approximate equations of motions for these parameters. Thus,

$$\frac{d\omega}{dt} = 2b\omega + V_i \zeta \kappa \omega (1+\omega^2)^{-1}(1 - 2\omega^4 - \omega^2 + 2\zeta^2\omega^2), \tag{5.9}$$

with $\kappa = \exp\left(-\frac{\zeta^2}{1+\omega^2}\right)/(1+\omega^2)^{5/2}$. The motion of the center of mass is given by the time derivative of ζ,

$$\frac{d\zeta}{dt} = v + V_i \kappa \omega^2 (1 + \omega^2 - 2\zeta^2), \tag{5.10}$$

and the variational equations for velocity, v and chirp b are given by,

$$\begin{aligned}\frac{dv}{dt} = & -2\alpha\zeta + 2\kappa(V_0\zeta(1+\omega^2) \\ & + V_i(v\zeta + v\zeta\omega^2 + \omega^2 b + \omega^4 b - 2\omega^2\zeta^2 b)),\end{aligned} \tag{5.11}$$

and,

$$\begin{aligned}\frac{db}{dt} =& \frac{1}{2\omega^4} - 2b^2 - \alpha + V_0\kappa(1+\omega^2-2\zeta^2) + \frac{g_0 N}{2\sqrt{2\pi}\omega^3} \\ &+ \frac{6\sqrt{2}q_0 N^{3/2}}{10\sqrt{5}\pi^{3/4}\omega^{7/2}} - \frac{3p_0 N}{2\sqrt{2\pi}\omega^5} + \frac{2\chi_0 N^2}{3\sqrt{3}\pi\omega^4}.\end{aligned} \tag{5.12}$$

Eqs.5.9, 5.10, 5.11 and 5.12 are solved numerically (Runge-Kutta method) and plotted in Figs.5.2 and 5.3 and have shown the time evolution of ω, v and ζ for different V_i values. For $|V_0| = 1$ case, the corresponding linear system shows a $\mathcal{PT}$ broken state when $|V_i| > |V_c|$(where, $|V_c| = 0.7$) with V_c known as $\mathcal{PT}$ breaking point(obtained in chapter 2). Hence the following three cases are selected. i.e., 1) $|V_i| = 0.2$ (far below the $\mathcal{PT}$ breaking), 2) $|V_i| = 0.6$ (just below the $\mathcal{PT}$ breaking) and 3) $|V_i| = 1$ (above the $\mathcal{PT}$ breaking point). From the bottom panel of Fig.5.2, it is clear that the condensate gets collapsed as it is well above V_c. The mean field correction terms are negligible for each case plotted here; i.e., for the time scale $(0, 30)$. As the time evolves(for example $t = (70, 90)$), the plots with the mean field correction terms(red dashed curve) show slight difference from that without correction terms(blue solid curve)(first row of Fig.5.3). Whereas the loss/gain term coefficient V_i increases, the effects from imaginary part of the $\mathcal{PT}$ potential is more predominant than that from the mean free field correction terms and hence both curves(red and blue) are overlapping(second row of Fig.5.3).

5.3 Collective excitations

Frequencies of collective oscillation modes are found in this section. We first differentiate Eqs.5.9 and 5.10 to get,

$$\begin{aligned}&\frac{d^2\zeta}{dt^2} + 2\alpha\zeta - 2V_0\kappa\zeta(1+\omega^2) - V_i\kappa(1+\omega^2)^{-2}\mu \\ &- V_i^2\kappa^2(1+\omega^2)^{-3}\eta = 0\end{aligned} \tag{5.13}$$

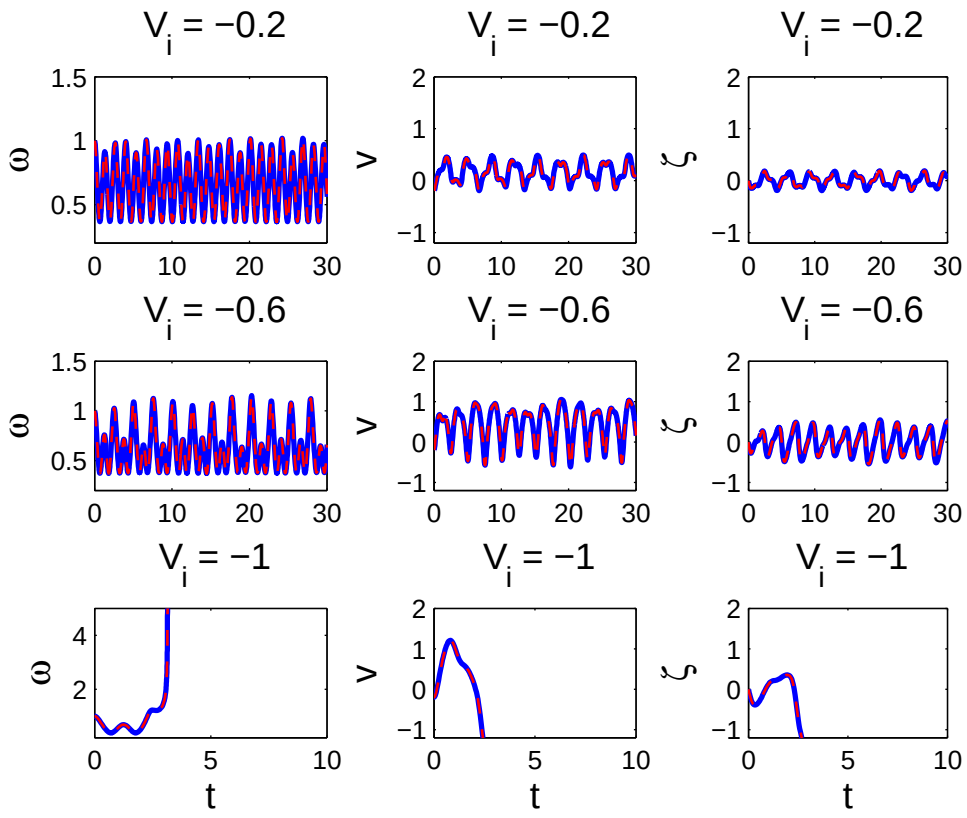

Figure 5.2: This figure depicts the time evolution of ω, v and ζ for different V_i values. For the last row $|V_i| > |V_c|$, where V_c is the $\mathcal{PT}$ breaking point of the system in the linear limit. Blue curves represent the evolution with out any mean field correction terms. Red dashed lines are that with correction terms. Both curves are overlapping for the initial range $[0, 30]$ of time. Initial conditions for the time evolution plot are, $V_0 = -1$, $\zeta_0 = 0$, $\omega_0 = 1$, $A = 1$, $v_0 = -0.2$ and $b_0 = 0.0021$.

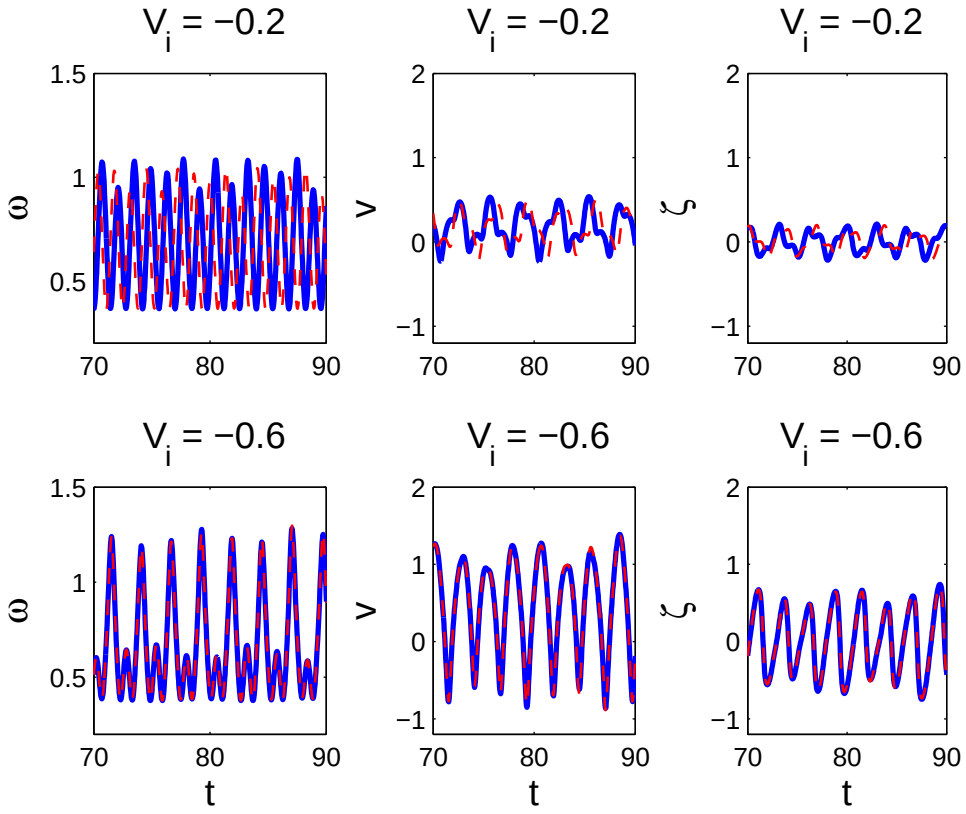

Figure 5.3: This figure depicts the time evolution of ω, v and ζ for different V_i values for the time scale range $(70, 90)$. Blue curves represents the evolution with out any mean field correction terms. Red dashed lines are that with correction terms. Both curves are overlapping in the bottom row. But, in the top row a slight deviation is observed. Initial conditions for the time evolution plot are, $V_0 = -1$, $\zeta_0 = 0$, $\omega_0 = 1$, $A = 1$, $v_0 = -0.2$ and $b_0 = 0.0021$.

$$\frac{d^2\omega}{dt^2} + 2\alpha\omega - \frac{1}{\omega^3} - \frac{g_0 N}{\sqrt{2\pi}\omega^2} - \frac{6\sqrt{2}q_0 N^{3/2}}{5\sqrt{5}\pi^{3/4}\omega^{5/2}} + \frac{3p_0 N}{\sqrt{2\pi}\omega^4} - \frac{4\chi_0 N^2}{3\sqrt{3}\pi\omega^3} - 2V_0\kappa(\omega + \omega^3 - 2\zeta^2\omega) - V_i\kappa(1+\omega^2)^{-3}\tilde{\mu} - V_i^2\kappa^2(1+\omega^2)^{-4}\tilde{\eta} = 0 \tag{5.14}$$

with

$\mu = b(6\omega^2 + 12\omega^4 + 6\omega^6) + v(2 - 6\omega^4 - 4\omega^6)\zeta + b(-12\omega^2 + 12\omega^6)\zeta^2 + v(4\omega^2 + 4\omega^4)\zeta^3 + (-8b\omega^4)\zeta^4$,

and $\eta = (2\omega^2 - 5\omega^4 - 31\omega^6 - 43\omega^8 - 23\omega^{10} - 4\omega^{12})\zeta + (-4\omega^2 + 28\omega^4 + 66\omega^6 + 32\omega^8 - 2\omega^{10})\zeta^3 + (-20\omega^4 - 4\omega^6 + 16\omega^8)\zeta^5 + (-8\omega^6)\zeta^7$.

$\tilde{\mu}$ is given as $\tilde{\mu} = (4b\zeta + v - 2v\zeta^2)\omega + (-4v\zeta^4 + 20b\zeta^3 + 2v\zeta^2 - 14b\zeta + v)\omega^3 + (8b\zeta^5 - 4v\zeta^4 + 10v\zeta^2 - 36b\zeta - 3v)\omega^5 + (-20b\zeta^3 + 6v\zeta^2 - 14b\zeta - 5v)\omega^7 + (16b\zeta - 2v)\omega^9$,

and $\tilde{\eta}$ is given by $\tilde{\eta} = (\zeta^2)\omega + (14\zeta^4 - 13\zeta^2 + 1)\omega^3 + (24\zeta^6 - 16\zeta^4 - 22\zeta^2 + 3)\omega^5 + (40\zeta^6 - 110\zeta^4 + 49\zeta^2)\omega^7 + (4\zeta^6 - 76\zeta^4 + 97\zeta^2 - 10)\omega^9 + (-4\zeta^4 + 42\zeta^2 - 15)\omega^{11} + (2\zeta^2 - 9)\omega^{13} - 2\omega^{15}$.

Substituting $\zeta = \zeta_0 + \delta\zeta$, $\omega = \omega_0 + \delta\omega$ and linearizing the Eqs5.13 and 5.14 around the equilibrium points (ζ_0, ω_0) we can find the collective excitation frequencies. The Gaussian (real potential) and $\mathcal{PT}$ symmetric (complex potential) traps are separately discussed and excitation frequencies are found in the following subsections.

5.3.1 Collective excitation in the Gaussian trap

We take $V_i = 0$ here, now the trap is Gaussian in its form and then Eqs.5.13 and 5.14 are coupled with coupling parameters: ζ, the center of mass position and ω, the condensate width. The equilibrium points corresponding to the stationary states of the condensate trapped in Gaussian trap are given by,

$$2\alpha\zeta_0 - 2V_0\kappa_0\zeta_0(1+\omega_0^2) = 0, \tag{5.15}$$

$$2\alpha\omega_0 - \frac{1}{\omega_0^3} - \frac{g_0 N}{\sqrt{2\pi}\omega_0^2} - \frac{6\sqrt{2}q_0 N^{3/2}}{5\sqrt{5}\pi^{3/4}\omega_0^{5/2}} + \frac{3p_0 N}{\sqrt{2\pi}\omega_0^4} - \frac{4\chi_0 N^2}{3\sqrt{3}\pi\omega_0^3} - 2V_0\kappa_0(\omega_0 + \omega_0^3 - 2\zeta_0^2\omega_0) = 0. \tag{5.16}$$

Hence the stable equilibrium points are obtained as,

$$\zeta_0 = 0, \tag{5.17}$$

and

$$2\alpha\omega_0 = \frac{1}{\omega_0^3} + \frac{g_0 N}{\sqrt{2\pi}\omega_0^2} + \frac{6\sqrt{2}q_0 N^{3/2}}{5\sqrt{5}\pi^{3/4}\omega_0^{5/2}} - \frac{3p_0 N}{\sqrt{2\pi}\omega_0^4} + \frac{4\chi_0 N^2}{3\sqrt{3}\pi\omega_0^3} + \frac{2V_0\omega_0}{(1+\omega_0^2)^{3/2}}. \tag{5.18}$$

Expanding Eqs.5.13 and 5.14 around the stable equilibrium points and linearizing it, we get,

$$\begin{bmatrix} \ddot{\delta\zeta} \\ \ddot{\delta\omega} \end{bmatrix} + \begin{bmatrix} m_1 & 0 \\ 0 & m_2 \end{bmatrix} \begin{bmatrix} \delta\zeta \\ \delta\omega \end{bmatrix} = 0, \tag{5.19}$$

where, the matrix M with elements

$m_1 = 2\alpha - (2V_0/(1+\omega_0^2)^{3/2})$ and

$m_2 = 2\alpha + (3/\omega_0^4) + (2g_0 N/\sqrt{2\pi}\omega_0^3) + (3\sqrt{2}q_0 N^{3/2}/\sqrt{5}\pi^{3/4}\omega_0^{7/2}) - (12p_0 N/\sqrt{2\pi}\omega_0^5) + (4\chi_0 N^2/\sqrt{3}\pi\omega_0^4) + (2V_0(-1+3\omega_0^4+2\omega_0^6)/(1+\omega_0^2)^{9/2})$.

The frequencies of the collective modes are related to the eigenvalues of the matrix M. Hence solving $\left|M - \Omega^2 I\right| = 0$, we get,

$$\Omega_1 = \sqrt{2}\sqrt{\alpha - \frac{V_0}{\left(\omega_0^2+1\right)^{3/2}}}, \tag{5.20}$$

$$\Omega_2 = \frac{\sqrt{I + \frac{60V_0\omega_0^{10}}{(\omega_0^2+1)^{9/2}} + \frac{90V_0\omega_0^8}{(\omega_0^2+1)^{9/2}} - \frac{30V_0\omega_0^4}{(\omega_0^2+1)^{9/2}} + 20\sqrt{3}\chi_0\omega_0^2 + 45}}{\sqrt{15}\omega_0^2}, \tag{5.21}$$

where N is substituted with $\sqrt{\pi}A^2\omega_0$ and $A = 1$. Also $I = 30\alpha\omega_0^4 + 15\sqrt{2}g_0\omega_0^2 - 90\sqrt{2}P_0 + 9\sqrt{10}q_0\omega_0^2$. Now we can write the equation of motion of the center of mass and width of the condensate as, $\zeta = A\sin(\Omega_1 t + \theta_1)$ and $\omega = \omega_0 + B\sin(\Omega_1 t + \theta_2)$ respectively, with A, B and θ are real constants.

Figs.5.4 and 5.5 show the behavior of the equilibrium width ω_0 and the collective excitation frequencies Ω_1, Ω_2 versus the number of atoms in the condensate, N. Solid blue curves are for $V_0 = -0.3$, dashed black curves for $V_0 = -0.7$ and dashed dotted red curves are for $V_0 = -1$. Boxes are corresponding curves with the mean field correction terms included. The range of N in the plots corresponds to N_0 values in the range 400 to 12000. As the depth of the trap V_0 is increased, the excitation frequencies shifted to higher values(Fig.5.5). Another point is, for each V_0, there exists a threshold value to N, N_c below which condensate width possesses positive values and above which the width of the condensate shows negative values meaning that the condensate gets collapsed. It is also observed the reappearance of width for further increase in N. For example, $V_0 = -0.3$ case, the critical number $N_c \approx 3.2$ and above this threshold value, the equilibrium width, $\omega_0 = -20.5935$(negative value for width) and a large positive value $\omega_0 = 22.0653$ for $N = 4$, as depicted in the inset of Fig.5.4. It is shown that the threshold in particle number, N_c has a strong depends on the trap parameter, V_0. As depth of the trap V_0 increases, the critical number N_c decreases.

5.3.2 Collective excitation in the $\mathcal{PT}$ symmetric trap

In this case, $V_i \neq 0$ and $V_0 \neq 0$, then the Eqs.5.9, 5.10, 5.11 and 5.12 are coupled, hence we have to analyze both $\frac{d^2v}{dt^2}$ and $\frac{d^2b}{dt^2}$ along with Eqs.5.13 and 5.14 to get,

$$\frac{d^2v}{dt^2} = \eta_1\zeta_t + \eta_2\omega_t + \eta_3 v_t + \eta_4 b_t, \tag{5.22}$$

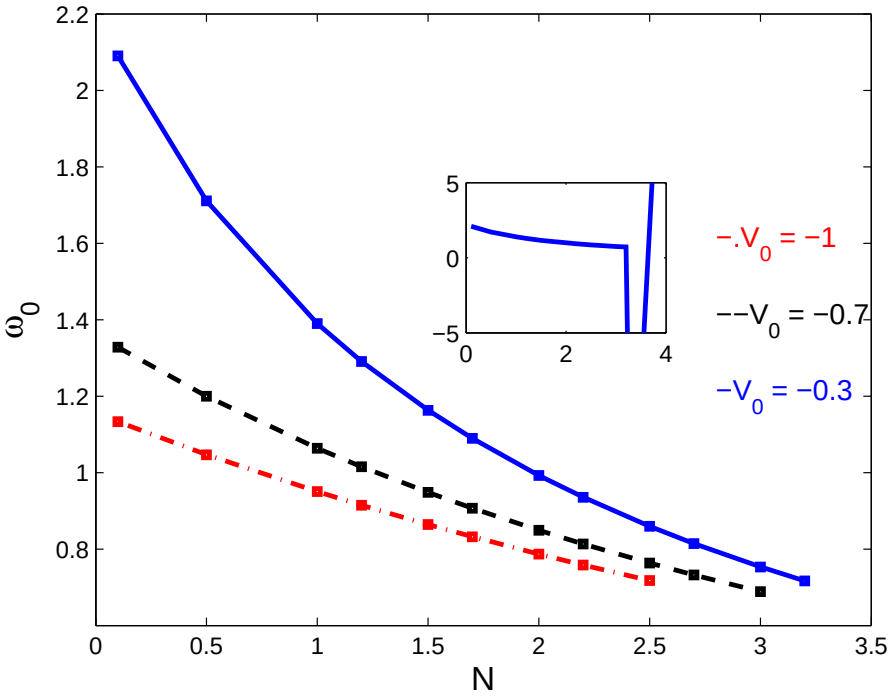

Figure 5.4: Equilibrium width ω_0 versus number of atoms in the condensate, N are depicted here. The range of N in the plots corresponds to N_0 values in the range 400 to 12000. Solid lines are for $V_0 = -0.3$, dashed lines for $V_0 = -0.7$ and dashed doted lines are for $V_0 = -1$. Corresponding boxes represents the mean field corrected values. It is obvious that for the parameters taken, the mean field correction values are negligible. The inset plot shows the behavior of ω_0 with $N > N_c$ for $V_0 = -0.3$.

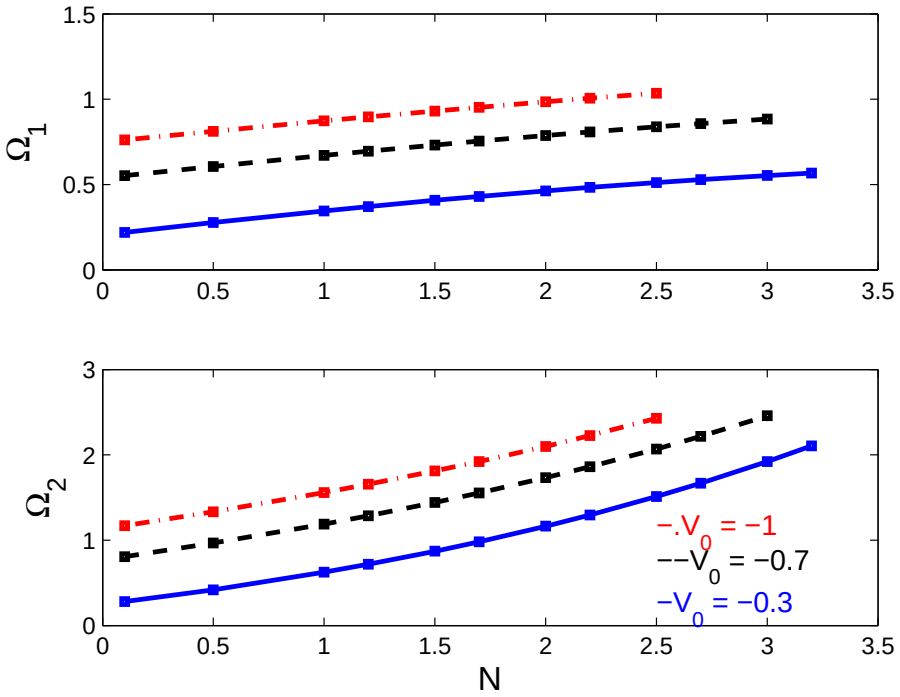

Figure 5.5: Excitation frequencies Ω_1 and Ω_2 versus number of atoms in the condensate, N are depicted here. The range of N in the plots corresponds to N_0 values in the range 400 to 12000. Solid lines are for $V_0 = -0.3$, dashed lines for $V_0 = -0.7$ and dashed doted lines are for $V_0 = -1$. Corresponding boxes represents the mean field corrected values. It is obvious that for the parameters taken, the mean field correction values are negligible.

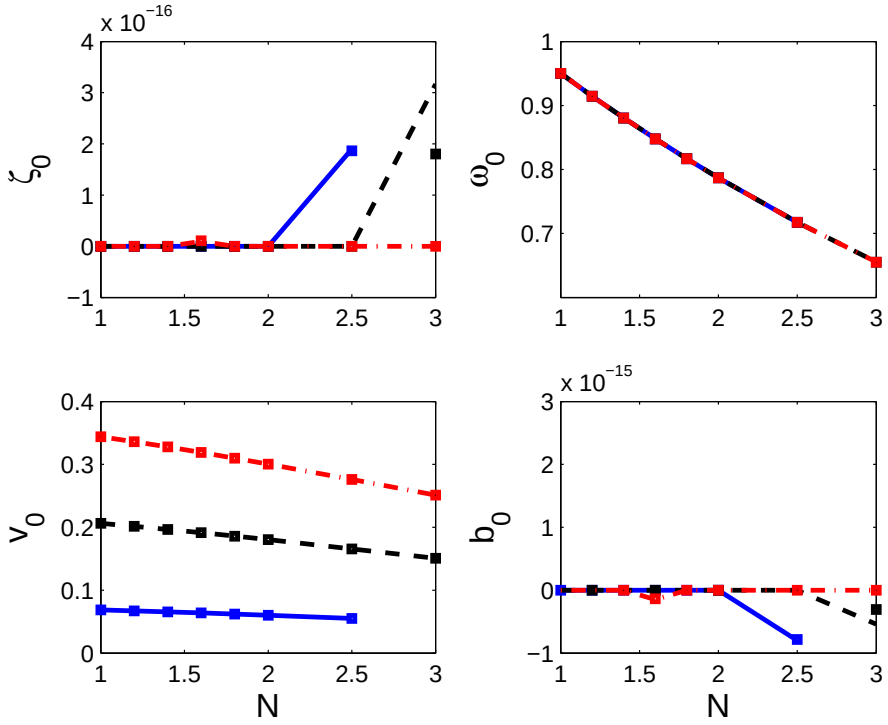

Figure 5.6: variation of equilibrium points ζ_0, ω_0, v_0, b_o versus N plot: The range of N in the plots corresponds to N_0 values in the range 4000 to 12000. Solid lines are for $V_i = -0.2$, dashed lines for $V_i = -0.6$ and dashed doted lines are for $V_i = -1$. Corresponding boxes represents the mean field corrected values.

$$\frac{d^2b}{dt^2} = -4bb_t + \mu_1\zeta_t + \mu_2\omega_t, \tag{5.23}$$

with ω_t, ζ_t, v_t and b_t(subscript denotes first derivative with respect to time) are given by Eqs. 5.9, 5.10, 5.11 and 5.12 respectively. And the expressions for the coefficients η_1, η_2, η_3, η_4, μ_1 and μ_2 are given in appendix.

By equating the second derivative terms in Eqs. 5.13, 5.14, 5.22 and 5.23 to zero and simultaneously solving the four equations to get the equilibrium points ζ_0, ω_0, v_0 and b_0. These equilibrium points versus N are plotted in Fig.5.6. The effect of the gain/loss parameter V_i to the system is very clear that it couples one more internal degree of freedom, namely the velocity of center of mass v to the position of the center of mass ζ and width ω. Another result to be pinpointed is that, as V_i increases, the corresponding v_0 has appreciable variation but there is no variation in the equilibrium width ω_0. This variation of v_0 represents a net motion of particles from the gain to loss regions, as required to conserve the overall particle number in the presence of V_i[141].

Next we expand Eqs. 5.13, 5.14, 5.22 and 5.23 around these equilibrium points and by linearizing, we will get the matrix equation as,

$$\begin{bmatrix} \ddot{\delta\zeta} \\ \ddot{\delta\omega} \\ \ddot{\delta v} \\ \ddot{\delta b} \end{bmatrix} + \begin{bmatrix} m_1 & m_2 & m_3 & m_4 \\ m_5 & m_6 & m_7 & m_8 \\ m_9 & m_{10} & m_{11} & m_{12} \\ m_{13} & m_{14} & m_{15} & m_{16} \end{bmatrix} \begin{bmatrix} \delta\zeta \\ \delta\omega \\ \delta v \\ \delta b \end{bmatrix} = 0. \tag{5.24}$$

Matrix elements (m_1 to m_{16}) are too long to be included in this thesis. Solving $|M - \Omega^2 I| = 0$ numerically, we get the frequencies Ω_1, Ω_2, Ω_3 and Ω_4 and their dependence on N are depicted in Fig.5.7.

Another main result is that the threshold number N_c for a particular V_0 value gets hiked as $|V_i|$ increases. For $V_0 = -1$ and $V_i = 0$, the N_c is obtained as $N_c = 2.5$, then we have checked N_c for $|V_i| = 0.2$ and found that $N_c = 2.5$ itself. When $|V_i| = 0.6$ (just below $\mathcal{PT}$ breaking), N_c is

hiked to $N_c = 3$ and for $|V_i| = 1$ also N_c is kept at this hiked value. Red curves in Fig.5.5 are for parameter values $|V_0| = 1$ and $V_i = 0$, and blue, black, red curves in Fig.5.7 correspond to $|V_0| = 1$ with different V_i values. The hike in the value of N_c is observed as V_i approaches its critical value $|V_c| = 0.7$. This hike in the critical number of atoms N_c (as $|V_i|$ is increased to and just below the exceptional point V_c) may be the reason for quasi stability of the condensate below the $\mathcal{PT}$ breaking point as noted in chapter 2.

Fig.5.7 represents the collective excitation frequencies versus N plots for different V_i values. It is noted that, in this range of N values and for the parameters taken, the mean field corrections are negligible. For example, without any correction terms, i.e., $\alpha = -10^{-4}$, $g_0 = -1$, $q_0 = 0$, $p_0 = 0$, $\chi_0 = 0$, $V_0 = -1$ and $V_i = -0.6$ the values obtained for $[N, \zeta_0, \omega_0, v_0, b_0, \Omega_1, \Omega_2, \Omega_3, \Omega_4]$ are [1.6, -1.38×10^{-30}, 0.84799, 0.191419, 6.31×10^{-30}, 0.983529, 0.984821, 1.87435, 2.13481]. When correction terms are included, i.e., $\alpha = -10^{-4}$, $\tilde{g_0}^{'} = -2 \times 10^{-8}$, $q_0 = -2 \times 10^{-4}$, $p_0 = 2 \times 10^{-25}$ and $\chi_0 = 0$, then the quantities become [1.6, -1.97×10^{-31}, 0.847934,0.19141, 2.761×10^{-30}, 0.983572, 0.984864, 1.87451, 2.13508]. As in the previous case ($V_i = 0$), here also, the sudden collapse of condensate occurs above N_c. The condensate restore its width with high positive value for the further increase in N.

Our studies on collective excitations in $\mathcal{PT}$ symmetric systems are dealt in general and have to be extended in the following respects to get additional new physics.

a) Some authors claim the stability of the solutions in deep potential than in shallow potentials[131, 234]. Hence, our studies(in which the depth of the trapping potential is small) have to be extended for checking the results with deep real part of the $\mathcal{PT}$ symmetric potential. We expect that when the complex part of the $\mathcal{PT}$ symmetric potential which is responsible

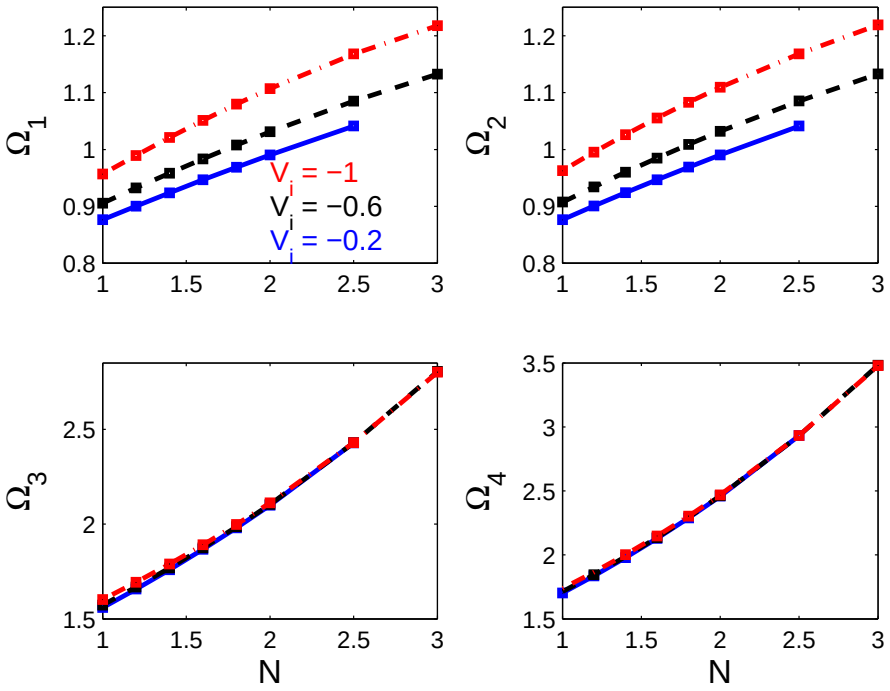

Figure 5.7: Collective excitation frequencies Ω_1, Ω_2, Ω_3 and Ω_4 versus number of atoms in the condensate N are depicted here. The range of N in the plots corresponds to N_0 values in the range 4000 to 12000. For all panels $V_0 = -1$. Solid lines are for $V_i = -0.2$, dashed lines for $V_i = -0.6$ and dashed doted lines are for $V_i = -1$. Corresponding boxes represents the mean field corrected values.

to instabilities is dominated by the real part(applying a deep real part of the $\mathcal{PT}$ symmetric potential), the condensate stabilizes.

b) The mean filed correction terms(with the given set of parameter values)could not neither arrest the collapse of the condensate nor suppress the reappearance of the excitation frequencies even in the absence of imaginary part of the complex potential. Hence we have to work more on the region of parameters where the corrections terms start to play on the excitation frequencies.

5.4 Scattering by the PT defect

We have studied numerically the scattering of solitons by $\mathcal{PT}$ defect in chapter 3 with the real part of the trapping potential is taken to be of the form $V_I^A(x) = -V_i x^{2l-1} \exp(-x^{2l})$, $l = 2$. There we have seen that the unidirectional properties shown by the system depends on both the angle of incidence and the depth of the imaginary part of the trapping potential. In this section we have tried to solve the scattering problem via variational approach for slightly different form of trapping potential, i.e., $l = 1$ case. The main attraction of this study is to look for the effect of the beyond mean filed correction terms on the scattering process.

The variational approach with trial function given in Eq.5.5 is apt to explain the scattering of soliton by the $\mathcal{PT}$ defect qualitatively. Here the defect is a nonlinear effective potential created by the combined effects of $\mathcal{PT}$ symmetric potential and nonlinear interaction terms in Eq.5.4 and this $\mathcal{PT}$ defect is kept at $\zeta = 0$ position. When a soliton (centered far away from the defect, i.e., $\zeta >> 0$) approaches the defect and allowed to interact with the defect for a sufficiently long interval of time, then depending on the value of V_i the following situations may occur; reflection, transmission and trapping of the soliton by the defect. It can be demonstrated by

solving numerically the variational Eqs.5.9, 5.10, 5.11 and 5.12 by Runge-Kutta method.

The soliton is made to approach the defect from $\zeta = 10$. The scattering properties shown by this Gaussian $\mathcal{PT}$ defect is illustrated in Fig.5.8. The different regimes of scattering are depicted by keeping the real part of the defect potential, $V_0 = -0.3$ as constant and varied the imaginary part V_i of the PT defect.The parameter values are $c_0 = -1$, $c_1 = c_2 = c_3 = 0$, $\alpha = -10^{-4}$. Three regimes: (a) reflection (solid black curve) with $V_i = -0.05$ (b) transmission (solid green curve) with $V_i = -0.4$ (c) trapping (solid blue curve) with $V_i = -0.7$ are obtained. The initial conditions used are, $\zeta_0 = 10$, $\omega_0 = 1$, $A = 1$, $v_0 = -0.2$ and $b_0 = 0.0021$. Thus we have found the three regimes of the scattering for present system by varying the gain/loss coefficient V_i.

For the same parameters with the launching position shifted to $\zeta = -10$ is shown in Fig.5.9. We can see that the scattering regimes in this case are not matching with the previous case ($\zeta = 10$); i.e., it depends on the launching position of incoming soliton (we got this type of unidirectional behavior in chapter 3 also).

Now we add the mean field correction terms and examine how these terms affect the scattering dynamics. For this, the trapping case with $V_i = -0.7$ and $V_0 = -0.3$ in the Fig.5.8(solid blue curve) is considered again to find the effects of the mean field correction and three body interaction terms and plotted the results in Fig.5.10. Here, solid blue curve represents the same case as that in the Fig.5.8(without any correction terms). The dashed red curve represents the time evolution of ζ with only the three body interaction term added, $c_3 = 10^{-7}$. The dashed doted line(Cyan) represents that with the mean field correction terms added, $c_0 = -1 - 2 \times 10^{-8}$, $c_1 = -2 \times 10^{-4}$ and $c_2 = 2 \times 10^{-25}$. It is observed that, when the three-body interaction term is added, the trapped soliton is propagated

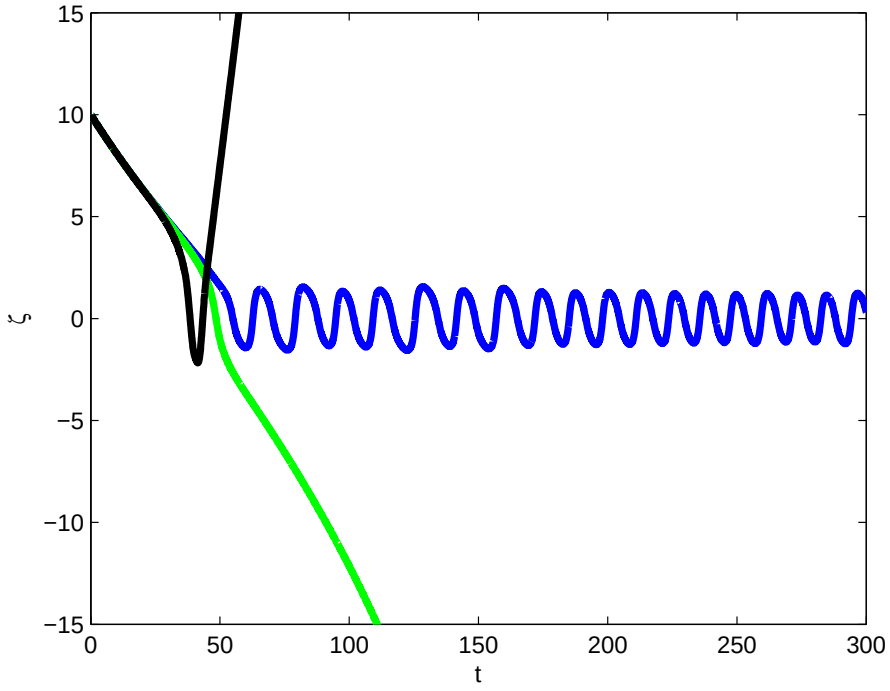

Figure 5.8: Time evolution of the center of mass: V_0 is kept at $V_0 = -0.3$ and V_i values are varied. The mean field correction terms are absent here. Figure consists of three cases, (a) reflection (solid black curve) with $V_i = -0.05$ (b) transmission (solid green curve) with $V_i = -0.4$ (c) trapping with $V_i = -0.7$. The initial conditions used are, $\zeta_0 = 10$, $\omega_0 = 1$, $A = 1$, $v_0 = -0.2$ and $b_0 = 0.0021$.

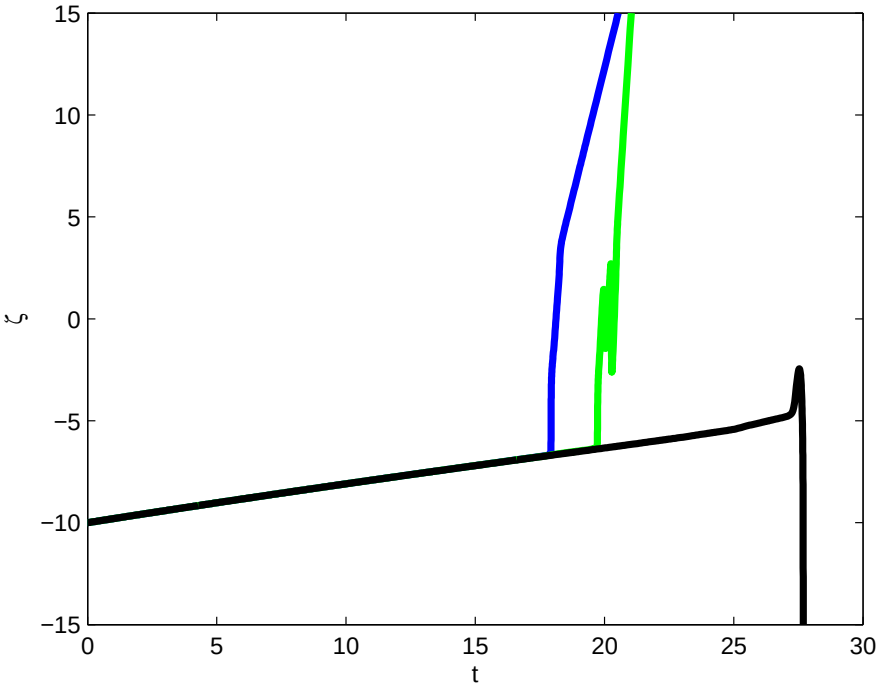

Figure 5.9: Time evolution of the center of mass: V_0 is kept at $V_0 = -0.3$ and V_i values are varied. All parameters are same as that in Fig. 5.8 except that the soliton has initially launched from loss side.

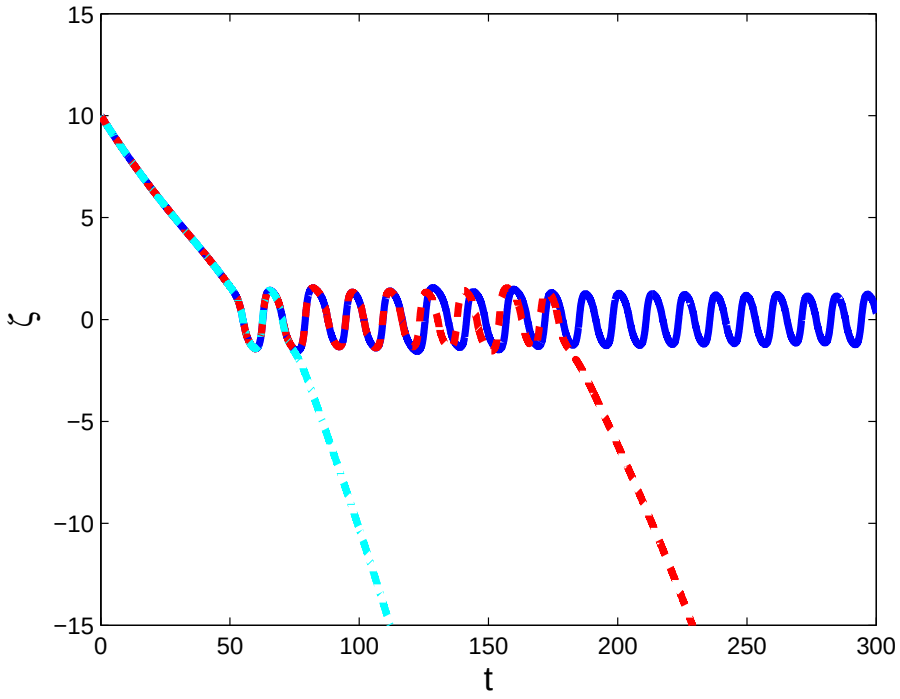

Figure 5.10: Time evolution of the center of mass: The trapping case with $V_i = -0.7$, $V_0 = -0.3$ and $c_0 = -1$ in the Fig.5.8 (solid blue lines) is considered with the mean correction and three body interaction terms added to it. The initial conditions used are, $\zeta_0 = 10$, $\omega_0 = 1$, $A = 1$, $v_0 = -0.2$ and $b_0 = 0.0021$. Dashed red curve represents the time evolution of ζ with three body interaction term alone is added i.e., $c_3 = 10^{-7}$. Dashed doted lines (Cyan) represents that with the mean field correction terms are added, $c_0 = -1 - 2 \times 10^{-8}$, $c_1 = -2 \times 10^{-4}$ and $c_2 = 2 \times 10^{-25}$.

for less time (compared to that with only two body interaction is present) and gets transmitted. Similarly for the addition of mean field correction terms, the trapping case is almost flipped in to a transmission regime.

5.5 Summary of the chapter

We have investigated collective excitations of a 1-D BEC trapped in a Gaussian $\mathcal{PT}$ symmetric potential well by solving the time-dependent GPE with the mean field correction terms(quantum fluctuations and effective range expansion). It is noted that the effects from these correction terms are negligible when we consider high values for gain/loss coefficient. Variational approach for dissipative systems are employed for analyzing the system. The equilibrium values for variational parameters are found out and excitation frequencies are plotted for cases with and without loss/gain coefficient term. If only the real part of the $\mathcal{PT}$ symmetric trapping potential is present, the expressions for collective excitation frequencies show that only the center of mass motion and the width of the condensate are coupled together and the excitation frequencies depend on the depth of the real potential. For the $\mathcal{PT}$ symmetric trapping potential, the motion of the center of mass, velocity of center of mass and width are coupled together to get the collective excitations of the system. i.e., addition of gain/loss terms(imaginary part of the $\mathcal{PT}$ symmetric trapping potential) to the system affects it in such a way that the velocity of the motion of the center of mass of the condensate is varied. This results in a net motion of particles from the gain to loss regions, as required to conserve the overall particle number in the presence of this imaginary part of the potential. The critical number N_c of the condensate (for a particular depth V_0 of the real part of the potential) gets hiked as the loss/gain coefficient V_i approaches its critical point V_c.

We have also investigated the scattering of soliton by the $\mathcal{PT}$ defect in a 1-D BEC. The scattering dynamics is influenced by varying the imaginary part(gain/loss profile) of the $\mathcal{PT}$ defect. It is noted that there is no noticeable effect from these correction terms for reflection and transmission processes, while the motion of the center of mass position is affected by the mean field correction terms once it gets trapped in the defect, i.e., in one case of the initial conditions, when the soliton is trapped and oscillates in the well, it is found that the correction terms introduce instabilities leading to an ejection of the soliton.

In order to make this work significant, we should have to perform the numerical simulations and compare it with that obtained from variational analysis. Also we have to carefully check the role of the real part of the $\mathcal{PT}$ symmetric potential since applying a deep real part of the $\mathcal{PT}$ symmetric potential, the condensate is found to stable over collapse. The aforesaid works are planned for future studies.

6

Conclusions and Future scopes

$\mathcal{PT}$ symmetry has found applications in several areas spanning from $\mathcal{PT}$-symmetric quantum oscillators[52] to linear [71, 77] and nonlinear optics [141, 142], from microwave cavities[76] and electronics[235, 236] to quantum field theory[237], engineering even the loss of the system makes the $\mathcal{PT}$ symmetric studies relevant in the current science.

In this thesis, we have mainly studied the interplay between the focusing/defocusing non-linearity with the $\mathcal{PT}$ symmetry in 1-D BEC. We have also addressed how the matter wave solitons behave when gain/loss mechanisms are varied. The effects of the transverse profile of gain or loss on the existence of solitons have been studied by considering two different kinds of localized photonic potentials differing in their imaginary part.

For the attractive condensates(focusing nonlinearity), it is found that nonlinearity is able to reestablish the $\mathcal{PT}$ symmetry which were broken in the absence of the Kerr effect. We have observed that solitons become strongly unstable when the underlying system is beyond the linear exceptional point. A much smaller instability is also found even below the exceptional point, resulting in an exponential amplification which is contrasting with the available literature. In the defocusig case, the nonlinearity is unable to transit the system from a $\mathcal{PT}$ broken state(linear regime) to $\mathcal{PT}$ unbroken state(nonlinear regime). Thus, solitons do not exist above the linear exceptional point. $\mathcal{PT}$ symmetric matter wave solitons are found to be always stable when the transverse profile of the imag-

inary part of the complex potential remains invariant with the change in the real potential. The complex potentials whose imaginary part changes together with the real part, support unstable solitons in proximity of the exceptional point(fixed by the linear potential) and at the edge of the soliton existence region versus nonlinear excitation. Our findings can be applied to the investigation of BEC in open systems(exchanging energy with the environment), for example in the design of matter wave 'laser' operating near the $\mathcal{PT}$-breaking point [100, 238].

We have also analyzed the scattering of soliton by a $\mathcal{PT}$-symmetric defect and it is obtained that the scattering properties depend on the magnitude of the imaginary part of the potential and can be tuned to reciprocal to non-reciprocal behavior by tuning the angle of incidence. Results are promising for $\mathcal{PT}$ diode devices in information handling [80] and in matter wave interferometry [239, 240].

Another topic of the study was the dynamics of BEC with $\mathcal{PT}$ symmetry beyond mean field theory. The scattering dynamics is greatly influenced by varying the imaginary part(gain/loss profile) of the $\mathcal{PT}$ defect. It is noted that no noticeable effect from these correction terms for reflection and transmission processes, while the motion of the center of mass position is greatly affected by the mean field correction terms once it gets trapped in the defect. We have also investigated the collective excitations of a 1-D BEC trapped in a Gaussian $\mathcal{PT}$ symmetric potential well. If only the real part of the $\mathcal{PT}$ symmetric trapping potential is present, the expressions for collective excitation frequencies show that only the center of mass motion and the width of the condensate are coupled together and the excitation frequencies depend on the depth of the real potential. Addition of gain/loss terms to the system affects it in such a way that the velocity of the motion of the center of mass of the condensate is varied. The critical number N_c of the condensate(for a particular depth V_0

of the real part of the potential) gets hiked as the loss/gain coefficient V_i approaches its critical point V_c.

6.1 Future scopes

The potential types seen in BEC like monopole and dipole interactions also satisfy the $\mathcal{PT}$ symmetric conditions. Hence $\mathcal{PT}$ symmetric studies can also be done in the context of monopolar and dipolar BEC. The $\mathcal{PT}$ symmetric studies can be extended to vortex solutions in a rotating Bose-Einstein condensate. Other topics of interest are the modulational instability and spin-orbit coupling in $\mathcal{PT}$ symmetric systems. The studies on general class of pseudo-Hermitian operators with special symmetries[237] are promising area to widen the concepts related to $\mathcal{PT}$ symmetry. These are some of the areas proposed for future studies.

Bibliography

[1] S. N. Bose. Plancks law and light quantum hypothesis. *Z. Phys*, 26:178, 1924.

[2] A. Einstein. *Sitzungsber. K. Preuss. Akad. Wiss. Phys. Math. Kl.*, 261, 1924.

[3] A. Einstein. *Sitzungsber. K. Preuss. Akad. Wiss. Phys. Math. Kl.*, 3, 1925.

[4] Alexander L Fetter and John Dirk Walecka. *Quantum theory of many-particle systems*. Courier Corporation, 2003.

[5] J. M. Leinaas and J. Myrheim. On the theory of identical particles. *Il Nuovo Cimento B*, 37(1):1, 1977.

[6] Steven Chu. Nobel lecture: The manipulation of neutral particles. *Rev. Mod. Phys.*, 70(3):685, 1998.

[7] William D. Phillips. Nobel lecture: Laser cooling and trapping of neutral atoms. *Rev. Mod. Phys.*, 70(3):721, 1998.

[8] Harald F Hess. Evaporative cooling of magnetically trapped and compressed spin-polarized hydrogen. *Phys. Rev. B*, 34(5):3476, 1986.

[9] M. H. Anderson, J. R. Ensher, M. R. Matthews, C. E. Wieman, and E. A. Cornell. in a dilute atomic vapor. *science*, 269:14, 1995.

[10] Kendall B. Davis, M. O. Mewes, Michael R. Andrews, N. J. Van Druten, D. S. Durfee, D. M. Kurn, and Wolfgang Ketterle. Bose-Einstein condensation in a gas of sodium atoms. *Phys. Rev. Lett.*, 75(22):3969, 1995.

[11] Cl. C. Bradley, C. A. Sackett, J. J. Tollett, and Randall G Hulet. Evidence of Bose-Einstein condensation in an atomic gas with attractive interactions. *Phys. Rev. Lett.*, 75(9):1687, 1995.

[12] Dale G Fried, Thomas C Killian, Lorenz Willmann, David Landhuis, Stephen C Moss, Daniel Kleppner, and Thomas J Greytak. Bose-Einstein condensation of atomic hydrogen. *Phys. Rev. Lett.*, 81(18):3811, 1998.

[13] F Pereira Dos Santos, Jérémie Léonard, Junmin Wang, CJ Barrelet, F Perales, E Rasel, CS Unnikrishnan, M Leduc, and C Cohen-Tannoudji. Bose-Einstein condensation of metastable helium. *Phys. Rev. Lett.*, 86(16):3459, 2001.

[14] Giovanni Modugno, Gabriele Ferrari, Giacomo Roati, Robert J Brecha, A Simoni, and Massimo Inguscio. Bose-Einstein condensation of potassium atoms by sympathetic cooling. *Science*, 294(5545):1320–1322, 2001.

[15] Tino Weber, Jens Herbig, Michael Mark, Hanns-Christoph Nägerl, and Rudolf Grimm. Bose-Einstein condensation of cesium. *Science*, 299(5604):232–235, 2003.

[16] Yosuke Takasu, Kenichi Maki, Kaduki Komori, Tetsushi Takano, Kazuhito Honda, Mitsutaka Kumakura, Tsutomu Yabuzaki, and Yoshiro Takahashi. Spin-singlet Bose-Einstein condensation of two-electron atoms. *Phys. Rev. Lett.*, 91(4):040404, 2003.

[17] Sebastian Kraft, Felix Vogt, Oliver Appel, Fritz Riehle, and Uwe Sterr. Bose-Einstein condensation of alkaline earth atoms: Ca 40. *Phys. Rev. Lett.*, 103(13):130401, 2009.

[18] Simon Stellmer, Meng Khoon Tey, Bo Huang, Rudolf Grimm, and Florian Schreck. Bose-Einstein condensation of strontium. *Phys. Rev. Lett.*, 103(20):200401, 2009.

[19] Y Natali Martinez de Escobar, BJ Desalvo, P. G. Mickelson, M Yan, and T. C. Killian. Bose-Einstein condensation of Sr 84. In *APS Division of Atomic, Molecular and Optical Physics Meeting Abstracts*, volume 1, page 6006, 2010.

[20] Axel Griesmaier, Jörg Werner, Sven Hensler, Jürgen Stuhler, and Tilman Pfau. Bose-Einstein condensation of chromium. *Phys. Rev. Lett.*, 94(16):160401, 2005.

[21] Mingwu Lu, Nathaniel Q Burdick, Seo Ho Youn, and Benjamin L Lev. Strongly dipolar Bose-Einstein condensate of dysprosium. *Phys. Rev. Lett.*, 107(19):190401, 2011.

[22] K Aikawa, A Frisch, M Mark, S Baier, A Rietzler, R Grimm, and F Ferlaino. Bose-Einstein condensation of erbium. *Phys. Rev. Lett.*, 108(21):210401, 2012.

[23] Lev Pitaevskii and Stringari. Bose-Einstein condensation, 2003.

[24] C. J. Pethick and H. Smith. *Bose-Einstein Condensation in Dilute Gases*. Cambridge University Press, 2002.

[25] C. A. Regal, M. Greiner, and D. S. Jin. Observation of resonance condensation of fermionic atom pairs. *Phys. Rev. Lett.*, 92:040403, Jan 2004.

[26] M. W. Zwierlein, C. A. Stan, C. H. Schunck, S. M. F. Raupach, A. J. Kerman, and W. Ketterle. Condensation of pairs of fermionic atoms near a feshbach resonance. *Phys. Rev. Lett.*, 92:120403, Mar 2004.

[27] Eugene P Gross. Structure of a quantized vortex in boson systems. *Il Nuovo Cimento (1955-1965)*, 20(3):454–477, 1961.

[28] L. P. Pitaevskii. Vortex linex in an imperfect Bose gas. *Sov. Phys. JETP*, 13:451, 1961.

[29] Mark Edwards and K Burnett. Numerical solution of the nonlinear Schrödinger equation for small samples of trapped neutral atoms. *Phys. Rev. A*, 51(2):1382, 1995.

[30] Catherine Sulem and Pierre-Louis Sulem. *The nonlinear Schrödinger equation: self-focusing and wave collapse*, volume 139. Springer Science, 2007.

[31] D. A. W. Hutchinson, E Zaremba, and A Griffin. Finite temperature excitations of a trapped Bose gas. *Phys. Rev. Lett.*, 78(10):1842, 1997.

[32] Nikolaos-Pindaros Proukakis. *Microscopic mean field theories of trapped Bose-Einstein condensates*. PhD thesis, University of Oxford, 1997.

[33] Anthony J Leggett. Bose-Einstein condensation in the alkali gases: Some fundamental concepts. *Rev. Mod. Phys.*, 73(2):307, 2001.

[34] Franco Dalfovo, Stefano Giorgini, Lev P Pitaevskii, and Sandro Stringari. Theory of Bose-Einstein condensation in trapped gases. *Rev. Mod. Phys.*, 71(3):463, 1999.

[35] N Bogolubov. On the theory of superfluidity. *J. Phys*, 11:23–29, 1947.

[36] Panayotis G. Kevrekidis, Dimitri J. Frantzeskakis, and Ricardo Carretero-Gonzalez. *Emergent nonlinear phenomena in Bose-Einstein condensates: theory and experiment*, volume 45. Springer Science & Business Media, 2007.

[37] Juha Javanainen. Noncondensate atoms in a trapped Bose gas. *Phys. Rev. A*, 54(5):R3722, 1996.

[38] Allan Griffin, Tetsuro Nikuni, and Eugene Zaremba. *Bose condensed gases at finite temperatures*. Cambridge University Press, 2009.

[39] Catherine Sulem and Pierre-Louis Sulem. The nonlinear Schrodinger equation. *Appl. math. sci.* , 139, 1999.

[40] Yuri S Kivshar and Govind Agrawal. *Optical solitons: from fibers to photonic crystals*. Academic press, 2003.

[41] L Khaykovich, F Schreck, G Ferrari, Thomas Bourdel, Julien Cubizolles, LD Carr, Yvan Castin, and Christophe Salomon. Formation of a matter-wave bright soliton. *Science*, 296(5571):1290-1293, 2002.

[42] Kevin E Strecker, Guthrie B Partridge, Andrew G Truscott, and Randall G Hulet. Formation and propagation of matter-wave soliton trains. *Nature*, 417(6885):150-153, 2002.

[43] Eric A Cornell and Carl E Wieman. Nobel lecture: Bose-Einstein condensation in a dilute gas, the first 70 years and some recent experiments. *Rev. Mod. Phys.*, 74(3):875, 2002.

[44] Wolfgang Ketterle. Nobel lecture: When atoms behave as waves: Bose-Einstein condensation and the atom laser. *Rev. Mod. Phys.*, 74(4):1131, 2002.

[45] D. M. Stamper-Kurn, MR Andrews, AP Chikkatur, Stenger Inouye, H-J Miesner, J Stenger, and W Ketterle. Optical confinement of a Bose-Einstein condensate. *Phys. Rev. Lett.* , 80(10):2027, 1998.

[46] M. D. Barrett, JA Sauer, and MS Chapman. All-optical formation of an atomic Bose-Einstein condensate. *Phys. Rev. Lett.*, 87(1):010404, 2001.

[47] John Weiner, Vanderlei S Bagnato, Sergio Zilio, and Paul S Julienne. Experiments and theory in cold and ultracold collisions. *Rev. Mod. Phys.*, 71(1):1, 1999.

[48] Rudolf Grimm, Matthias Weidemüller, and Yurii B Ovchinnikov. Optical dipole traps for neutral atoms. *Adv. At. Mol. Opt. Phy.*, 42:95-170, 2000.

[49] Steven Weinberg. *Lectures on quantum mechanics*. Cambridge University Press, 2015.

[50] Eugene Wigner. On unitary representations of the inhomogeneous lorentz group. *Annals of mathematics*, pages 149-204, 1939.

[51] Leslie E Ballentine. *Quantum mechanics: A modern development*. World scientific, 1998.

[52] Carl M. Bender and Stefan Boettcher. Real spectra in non-Hermitian Hamiltonians having PT symmetry. *Phys. Rev. Lett.*, 80:5243–5246, Jun 1998.

[53] Richard C Brower, Miguel A Furman, and Moshe Moshe. Critical exponents for the reggeon quantum spin model. *Phys. Lett. B*, 76(2):213-219, 1978.

[54] Benjamin C Harms, Stanley T Jones, and Chung-I Tan. New structure in the energy spectrum of reggeon quantum mechanics with quartic couplings. *Phys. Lett. B*, 91(2):291–295, 1980.

[55] Michael E Fisher. Yang-lee edge singularity and ϕ 3 field theory. *Phys. Rev. Lett.*, 40(25):1610, 1978.

[56] E Caliceti, S Graffi, and M Maioli. Perturbation theory of odd anharmonic oscillators. *Commun. Math. Phys.*, 75(1):51-66, 1980.

[57] P. A. M. Dirac and J. C. Polkinghorne. The principles of quantum mechanics. *Physics Today*, 11:32, 1958.

[58] Carl M Bender. PT symmetry in quantum physics: From a mathematical curiosity to optical experiments. *Europhysics News*, 47(2):17-20, 2016.

[59] Manuel Kreibich. Realizations of PT-symmetric Bose-Einstein condensates with time-dependent Hermitian potentials. PhD thesis, Stuttgart, Universität Stuttgart, Diss., 2015.

[60] R. Carretero-Gonzalez, D. J. Frantzeskakis, and P. G. Kevrekidis. Nonlinear waves in Bose-Einstein condensates: physical relevance and mathematical techniques. *Nonlinearity*, 21(7):R139.

[61] Dennis Dast, Daniel Haag, Holger Cartarius, Jörg Main, and Günter Wunner. Eigenvalue structure of a Bose-Einstein condensate in a PT symmetric double well. *J. Phys. A: Math. Theor.*, 46(37):375301, 2013.

[62] D O'dell, S Giovanazzi, G Kurizki, and V. M. Akulin. Bose-Einstein condensates with 1/r interatomic attraction: Electromagnetically induced gravity. *Phys. Rev. Lett.*, 84(25):5687, 2000.

[63] Thierry Lahaye, C Menotti, L Santos, M Lewenstein, and T Pfau. The physics of dipolar bosonic quantum gases. *Rep. Prog. Phys.*, 72(12):126401, 2009.

[64] Rüdiger Fortanier, Dennis Dast, Daniel Haag, Holger Cartarius, Jörg Main, Günter Wunner, and Robin Gutöhrlein. Dipolar Bose-Einstein condensates in a PT symmetric double-well potential. *Phys. Rev. A*, 89(6):063608, 2014.

[65] Ali Mostafazadeh. Pseudo-Hermiticity versus PT symmetry: the necessary condition for the reality of the spectrum of a non-Hermitian Hamiltonian. *J. Math. Phys.*, 43(1):205–214, 2002.

[66] Ali Mostafazadeh. Pseudo-Hermiticity versus PT symmetry: Ii. a complete characterization of non-Hermitian Hamiltonians with a real spectrum. *J. Math. Phys.*, 43, 2002.

[67] A Ruschhaupt, F Delgado, and JG Muga. Physical realization of PT-symmetric potential scattering in a planar slab waveguide. *J. Phys. A: Mathematical and General*, 38(9):L171, 2005.

[68] R El-Ganainy, K. G. Makris, D. N. Christodoulides, and Ziad H Musslimani. Theory of coupled optical pt-symmetric structures. *Opt. Lett.*, 32(17):2632-2634, 2007.

[69] Shachar Klaiman, Uwe Günther, and Nimrod Moiseyev. Visualization of branch points in PT-symmetric waveguides. *Phys. Rev. Lett.* , 101(8):080402, 2008.

[70] A. Guo, G. J. Salamo, D. Duchesne, R. Morandotti, M. Volatier-Ravat, V. Aimez, G. A. Siviloglou, and D. N. Christodoulides. Observation of PT-symmetry breaking in complex optical potentials. *Phys. Rev. Lett.*, 103:093902, 2009.

[71] C. E. Rüter, K. G. Makris, R. El-Ganainy, D. N. Christodoulides, M. Segev, and D. Kip. Observation of parity-time symmetry in optics. *Nat. Phys.*, 6:192–195, 2010.

[72] Liang Feng, Maurice Ayache, Jingqing Huang, Ye-Long Xu, Ming-Hui Lu, Yan-Feng Chen, Yeshaiahu Fainman, and Axel Scherer. Nonreciprocal light propagation in a silicon photonic circuit. *Science*, 333(6043):729-733, 2011.

[73] Mohammad-Ali Miri, Alois Regensburger, Ulf Peschel, and Demetrios N. Christodoulides. Optical mesh lattices with PT symmetry. *Phys. Rev. A*, 86:023807, Aug 2012.

[74] Alois Regensburger, Mohammad-Ali Miri, Christoph Bersch, Jakob Näger, Georgy Onishchukov, Demetrios N. Christodoulides, and Ulf Peschel. Observation of defect states in PT-symmetric optical lattices. *Phys. Rev. Lett.*, 110:223902, May 2013.

[75] Andrey A. Sukhorukov, Sergey V. Dmitriev, Sergey V. Suchkov, and Yuri S. Kivshar. Nonlocality in pt-symmetric waveguide arrays with gain and loss. *Opt. Lett.*, 37(11):2148-2150, Jun 2012.

[76] S. Bittner, B. Dietz, U. Günther, H. L. Harney, M. Miski-Oglu, A. Richter, and F. Schäfer. PT symmetry and spontaneous symmetry breaking in a microwave billiard. *Phys. Rev. Lett.*, 108:024101, Jan 2012.

[77] Y. D. Chong, Li Ge, and A. Douglas Stone. Symmetry breaking and laser-absorber modes in optical scattering systems. *Phys. Rev. Lett.*, 106:093902, Mar 2011.

[78] Zin Lin, Hamidreza Ramezani, Toni Eichelkraut, Tsampikos Kottos, Hui Cao, and Demetrios N. Christodoulides. Unidirectional invisibility induced by PT-symmetric periodic structures. *Phys. Rev. Lett.*, 106:213901, May 2011.

[79] Ali Mostafazadeh. Invisibility and PT symmetry. *Phys. Rev. A*, 87:012103, Jan 2013.

[80] Bo Peng, Şahin Kaya Özdemir, Fuchuan Lei, Faraz Monifi, Mariagiovanna Gianfreda, Gui Lu Long, Shanhui Fan, Franco Nori, Carl M Bender, and Lan Yang. Parity-time symmetric whispering-gallery microcavities. *Nature Physics*, 10(5):394–398, 2014.

[81] K. F. Zhao, M. Schaden, and Z. Wu. Enhanced magnetic resonance signal of spin-polarized rb atoms near surfaces of coated cells. *Phys. Rev. A*, 81:042903, Apr 2010.

[82] J. Rubinstein, P. Sternberg, and Q. Ma. Bifurcation diagram and pattern formation of phase slip centers in superconducting wires driven with electric currents. *Phys. Rev. Lett.*, 99:167003, Oct 2007.

[83] J. Schindler, Z. Lin, J. M. Lee, H. Ramezani, F. M. Ellis, and T. Kottos. Pt-symmetric electronics. *J.Phys.A: Math. Theor.*, 45:444029, 2012.

[84] Chao Zheng, Liang Hao, and Gui Lu Long. Observation of a fast evolution in a parity-time-symmetric system. *Philosophical Transactions of the Royal Society of London A: Mathematical, Physical and Engineering Sciences*, 371(1989), 2013.

[85] Fan Yang and Zhong Lei Mei. Guiding spps with pt-symmetry. *Scientific reports*, 5, 2015.

[86] Alexander Szameit, Mikael C. Rechtsman, Omri Bahat-Treidel, and Mordechai Segev. $\mathcal{PT}$. *Phys. Rev. A*, 84:021806, Aug 2011.

[87] Liang Feng, Ye-Long Xu, William S Fegadolli, Ming-Hui Lu, José EB Oliveira, Vilson R Almeida, Yan-Feng Chen, and Axel Scherer. Experimental demonstration of a unidirectional reflectionless parity-time

metamaterial at optical frequencies. *Nature materials*, 12(2):108–113, 2013.

[88] Eva Maria Graefe, H. J. Korsch, and A. E. Niederle. Mean-field dynamics of a non-hermitian Bose-hubbard dimer. *Phys. Rev. Lett.*, 101(15):150408, 2008.

[89] Eva Maria Graefe, H. J. Korsch, A. E. Niederle, et al. A non-Hermitian symmetric Bose Hubbard model: eigenvalue rings from unfolding higher-order exceptional points. *J. Phys. A: Math. Theor.*, 41(25):255206, 2008.

[90] Eva-Maria Graefe, Hans Jürgen Korsch, and Astrid Elisa Niederle. Quantum-classical correspondence for a non-Hermitian Bose-Hubbard dimer. *Phys. Rev. A*, 82(1):013629, 2010.

[91] Holger Cartarius and Günter Wunner. Model of a pt-symmetric Bose-Einstein condensate in a δ-function double-well potential. *Phys. Rev. A*, 86(1):013612, 2012.

[92] Manuel Kreibich, Jörg Main, Holger Cartarius, and Günter Wunner. Hermitian four-well potential as a realization of a PT-symmetric system. *Phys. Rev. A*, 87:051601, May 2013.

[93] Rudolf Grimm, Matthias Weidemller, and Yurii B. Ovchinnikov. Optical dipole traps for neutral atoms. *Advances In Atomic, Molecular, and Optical Physics*, 42:95-170, 2000.

[94] Y. Shin, G.-B. Jo, M. Saba, T. A. Pasquini, W. Ketterle, and D. E. Pritchard. Optical weak link between two spatially separated Bose-Einstein condensates. *Phys. Rev. Lett.*, 95:170402, Oct 2005.

[95] Tatjana Gericke, Peter Würtz, Daniel Reitz, Tim Langen, and Herwig Ott. High-resolution scanning electron microscopy of an ultracold quantum gas. *Nature Physics*, 4(12):949–953, 2008.

[96] Nicholas P Robins, Cristina Figl, Matthew Jeppesen, Graham R Dennis, and John D Close. A pumped atom laser. *Nature Physics*, 4(9):731–736, 2008.

[97] G. Barontini, R. Labouvie, F. Stubenrauch, A. Vogler, V. Guarrera, and H. Ott. Controlling the dynamics of an open many-body quantum system with localized dissipation. *Phys. Rev. Lett.*, 110:035302, Jan 2013.

[98] A Shabat and V Zakharov. Exact theory of two-dimensional self-focusing and one-dimensional self-modulation of waves in nonlinear media. *Soviet physics JETP*, 34(1):62, 1972.

[99] L. Khaykovich, F. Schreck, G. Ferrari, T. Bourdel, J. Cubizolles, L. D. Carr, Y. Castin, and C. Salomon. Formation of a Matter-Wave Bright Soliton. *Science*, 296(5571):1290–1293, 2002.

[100] Kevin E Strecker, Guthrie B Partridge, Andrew G Truscott, and Randall G Hulet. Formation and propagation of matter-wave soliton trains. *Nature*, 417:150–153, 2002.

[101] E. Tiesinga, B. J. Verhaar, and H. T. C. Stoof. Threshold and resonance phenomena in ultracold ground-state collisions. *Phys. Rev. A*, 47:4114–4122, May 1993.

[102] Yingji He, Xing Zhu, Dumitru Mihalache, Jinglin Liu, and Zhanxu Chen. Lattice solitons in PT-symmetric mixed linear-nonlinear optical lattices. *Phys. Rev. A*, 85:013831, Jan 2012.

[103] Fatkhulla Kh. Abdullaev, Yaroslav V. Kartashov, Vladimir V. Konotop, and Dmitry A. Zezyulin. Solitons in PT-symmetric nonlinear lattices. *Phys. Rev. A*, 83:041805, Apr 2011.

[104] V Achilleos, P. G. Kevrekidis, D. J. Frantzeskakis, and R Carretero-González. Dark solitons and vortices in pt-symmetric nonlinear media: from spontaneous symmetry breaking to nonlinear pt phase transitions. *Phys. Rev. A*, 86(1):013808, 2012.

[105] Xue-Feng Li, Xu Ni, Liang Feng, Ming-Hui Lu, Cheng He, and Yan-Feng Chen. Tunable unidirectional sound propagation through a sonic-crystal-based acoustic diode. *Phys. Rev. Lett.*, 106:084301, Feb 2011.

[106] Zhiwei Shi, Xiujuan Jiang, Xing Zhu, and Huagang Li. Bright spatial solitons in defocusing kerr media with PT-symmetric potentials. *Phys. Rev. A*, 84:053855, Nov 2011.

[107] Bikashkali Midya and Rajkumar Roychoudhury. Nonlinear localized modes in pt-symmetric optical media with competing gain and loss. *Annals of Physics*, 341:12–20, 2014.

[108] Avinash Khare, S. M. Al-Marzoug, and Hocine Bahlouli. Solitons in pt-symmetric potential with competing nonlinearity. *Phys. Lett. A*, 376(45):2880-2886, 2012.

[109] N. V. Alexeeva, IV Barashenkov, Andrey A Sukhorukov, and Yuri S Kivshar. Optical solitons in pt-symmetric nonlinear couplers with gain and loss. *Phys. Rev. A*, 85(6):063837, 2012.

[110] Rodislav Driben and Boris A Malomed. Stability of solitons in parity-time-symmetric couplers. *Opt. Lett.*, 36(22):4323-4325, 2011.

[111] R Driben and B. A. Malomed. Dynamics of higher-order solitons in regular and-symmetric nonlinear couplers. *EPL*, 99(5):54001, 2012.

[112] Sean Nixon, Lijuan Ge, and Jianke Yang. Stability analysis for solitons in PT-symmetric optical lattices. *Phys. Rev. A*, 85:023822, Feb 2012.

[113] Wei-Ping Zhong, Milivoj R Belić, and Tingwen Huang. Two-dimensional accessible solitons in pt-symmetric potentials. *Nonlinear Dynamics*, 70(3):2027–2034, 2012.

[114] Chao-Qing Dai and Yue-Yue Wang. A bright 2d spatial soliton in inhomogeneous Kerr media with pt-symmetric potentials. *Laser Physics*, 24(3):035401, 2014.

[115] Dan Anderson. Variational approach to nonlinear pulse propagation in optical fibers. *Phys. Rev. A*, 27(6):3135, 1983.

[116] Adrian Ankiewicz, Nail Akhmediev, and Natasha Devine. Dissipative solitons with a lagrangian approach. *Optical Fiber Technology*, 13(2):91-97, 2007.

[117] Zhang Fei, Vladimir V Konotop, Michel Peyrard, and Luis Vázquez. Kink dynamics in the periodically modulated φ 4 model. *Phys. Rev. E*, 48(1):548, 1993.

[118] Angel Sánchez, Alan R Bishop, and Francisco Domínguez-Adame. Kink stability, propagation, and length-scale competition in the periodically modulated sine-gordon equation. *Phys. Rev. E*, 49(5):4603, 1994.

[119] Vladimir V Konotop and Luis Vázquez. *Nonlinear random waves*. World Scientific, 1994.

[120] E Caglioti, S Trillo, B Crosignani, P Di Porto, and S Wabnitz. Finite-dimensional description of nonlinear pulse propagation in optical-fiber couplers with applications to soliton switching. *JOSA B*, 7(3):374-385, 1990.

[121] A. B. Aceves, A. D. Capobianco, B Constantini, C De Angelis, and G. F. Nalesso. Two-dimensional variational analysis of self-trapped solutions in planar waveguides. *Opt. Commun.*, 105(5):341-346, 1994.

[122] S Chávez Cerda, S. B. Cavalcanti, and J. M. Hickmann. A variational approach of nonlinear dissipative pulse propagation. *EPJ D-Atomic, Molecular, Optical and Plasma Physics*, 1(3):313–316, 1998.

[123] Lev. P. Pitaevskii and Sandro Stringari. *Bose-Einstein Condensation*. Oxford University Press, New York, 2003.

[124] Lloyd N. Trefethen. *Spectral Methods in MATLAB*. SIAM, Philadelphia, 2000.

[125] Claudio Canuto, M Yousuff Hussaini, Alfio Maria Quarteroni, A Thomas Jr, et al. *Spectral methods in fluid dynamics*. Springer Science & Business Media, 2012.

[126] David Gottlieb and Steven A Orszag. *Numerical analysis of spectral methods: theory and applications*. SIAM, 1977.

[127] Nimrod Moiseyev. *Non-Hermitian quantum mechanics*. Cambridge University Press, 2011.

[128] Shachar Klaiman, Uwe Günther, and Nimrod Moiseyev. Visualization of branch points in PT-symmetric waveguides. *Phys. Rev. Lett.*, 101:080402, Aug 2008.

[129] Holger Cartarius and Günter Wunner. Model of a PT-symmetric Bose-Einstein condensate in a δ-function double-well potential. *Phys. Rev. A*, 86:013612, Jul 2012.

[130] Holger Cartarius, Daniel Haag, Dennis Dast, and Gnter Wunner. Nonlinear Schrdinger equation for a PT -symmetric delta-function double well. *J. Phy. A: Math. Theor.*, 45(44):444008, 2012.

[131] Sumei Hu, Xuekai Ma, Daquan Lu, Zhenjun Yang, Yizhou Zheng, and Wei Hu. Solitons supported by complex PT symmetric Gaussian potentials. *Phys. Rev. A*, 84:043818, Oct 2011.

[132] Rudolf Grimm, Matthias Weidemüller, and Yurii B Ovchinnikov. Optical dipole traps for neutral atoms. *Advances in atomic, molecular, and optical physics*, 42:95–170, 2000.

[133] Pascal Böhi, Max F Riedel, Johannes Hoffrogge, Jakob Reichel, Theodor W Hänsch, and Philipp Treutlein. Coherent manipulation of Bose-Einstein condensates with state-dependent microwave potentials on an atom chip. *Nature Physics*, 5(8):592–597, 2009.

[134] Manuel Kreibich, Jörg Main, Holger Cartarius, and Günter Wunner. Realizing PT-symmetric non-Hermiticity with ultracold atoms and Hermitian multiwell potentials. *Phys. Rev. A*, 90:033630, Sep 2014.

[135] Jiteng Sheng, Mohammad-Ali Miri, Demetrios N. Christodoulides, and Min Xiao. PT symmetric optical potentials in a coherent atomic medium. *Phys. Rev. A*, 88:041803, Oct 2013.

[136] Víctor M. Pérez-García, Humberto Michinel, and Henar Herrero. Bose-Einstein solitons in highly asymmetric traps. *Phys. Rev. A*, 57:3837–3842, May 1998.

[137] G Theocharis, PG Kevrekidis, MK Oberthaler, and DJ Frantzeskakis. Dark matter-wave solitons in the dimensionality crossover. *Phys. Rev. A*, 76(4):045601, 2007.

[138] Kunal K. Das. Highly anisotropic Bose-Einstein condensates: Crossover to lower dimensionality. *Phys. Rev. A*, 66:053612, Nov 2002.

[139] Z. Ahmed. Real and complex discrete eigenvalues in an exactly solvable one-dimensional complex PT-invariant potential. *Phys. Lett. A*, 282:343-348, April 2001.

[140] Chandroth P. Jisha, Alessandro Alberucci, Valeriy A. Brazhnyi, and Gaetano Assanto. Nonlocal gap solitons in PT-symmetric periodic potentials with defocusing nonlinearity. *Phys. Rev. A*, 89:013812, Jan 2014.

[141] Z. H. Musslimani, K. G. Makris, R. El-Ganainy, and D. N. Christodoulides. Optical solitons in PT periodic potentials. *Phys. Rev. Lett.*, 100:030402, Jan 2008.

[142] Yaakov Lumer, Yonatan Plotnik, Mikael C. Rechtsman, and Mordechai Segev. Nonlinearly induced PT transition in photonic systems. *Phys. Rev. Lett.*, 111:263901, Dec 2013.

[143] Adrian Ankiewicz, Nail Akhmediev, and Natasha Devine. Dissipative solitons with a lagrangian approach. *Opt. Fiber Techn.*, 13(2):91 – 97, 2007.

[144] S. Chávez Cerda, S.B. Cavalcanti, and J.M. Hickmann. A variational approach of nonlinear dissipative pulse propagation. *EPJ D- Atomic, Molecular, Optical and Plasma Physics*, 1(3):313–316, 1998.

[145] Y. S. Kivshar and G. P. Agrawal. *Optical Solitons*. Academic Press, San Diego, CA, 2003.

[146] K.G. Makris, R. El-Ganainy, D.N. Christodoulides, and Z.H. Musslimani. Beam dynamics in pt symmetric optical lattices. *Phys. Rev. Lett.*, 100:103904, 2008.

[147] Lev Davidovich Landau, Evgenii Mikhailovich Lifshitz, JB Sykes, John Stewart Bell, and ME Rose. *Quantum mechanics, non-relativistic theory*, volume 11. 1958.

[148] Albert Messiah. *Quantum mechanics, v. 2*. North-Holland, 1961.

[149] Jun John Sakurai and Jim Napolitano. *Modern quantum mechanics*. Addison-Wesley, 2011.

[150] Leonard Sidney Rodberg and Raphael Morton Thaler. *Introduction to the quantum theory of scattering*. Academic Press, 1967.

[151] Ping Sheng. *Introduction to wave scattering, localization and mesoscopic phenomena*, volume 88. Springer Science & Business Media, 2006.

[152] R. W. Boyd. *Nonlinear Optics*. Academic Press, Boston, 1992.

[153] Yuri S Kivshar and Boris A Malomed. Dynamics of solitons in nearly integrable systems. *Rev. Mod. Phys.*, 61(4):763, 1989.

[154] I. M. Lifshitz and A. M. Kosevich. The dynamics of a crystal lattice with defects. *Rep. Prog. Phys.*, 29(1):217, 1966.

[155] Roy H Goodman and Richard Haberman. Chaotic scattering and the n-bounce resonance in solitary-wave interactions. *Phys. Rev. Lett.*, 98(10):104103, 2007.

[156] T. P. Billam, S. L. Cornish, and S. A. Gardiner. Realizing bright matter wave soliton collisions with controlled relative phase. *Phy. Rev. A*, 83(4):041602, 2011.

[157] Alexander D Cronin, Jörg Schmiedmayer, and David E Pritchard. Optics and interferometry with atoms and molecules. *Rev. Mod. Phys.*, 81(3):1051, 2009.

[158] S. L. Cornish, N. G. Parker, A. M. Martin, T. E. Judd, R. G. Scott, T. M. Fromhold, and C. S. Adams. Quantum reflection of bright matter-wave solitons. *Physica D: Nonlinear Phenomena*, 238(15):1299–1305, 2009.

[159] Hidetsugu Sakaguchi and Boris A Malomed. Matter-wave soliton interferometer based on a nonlinear splitter. *New J. Phys.*, 18(2):025020, 2016.

[160] Xiang D Cao and Boris A Malomed. Soliton-defect collisions in the nonlinear Schrödinger equation. *Phy. Lett. A*, 206(3):177–182, 1995.

[161] V. V. Konotop, Víctor M Pérez-García, Yi-Fa Tang, and Luis Vázquez. Interaction of a dark soliton with a localized impurity. *Phys. Lett. A*, 236(4):314–318, 1997.

[162] John L Helm, Thomas P Billam, and Simon A Gardiner. Bright matter-wave soliton collisions at narrow barriers. *Phys. Rev. A*, 85(5):053621, 2012.

[163] Thomas Ernst and Joachim Brand. Resonant trapping in the transport of a matter-wave soliton through a quantum well. *Phys. Rev. A*, 81(3):033614, 2010.

[164] P Engels and C Atherton. Stationary and nonstationary fluid flow of a Bose-Einstein condensate through a penetrable barrier. *Phys. Rev. Lett.*, 99(16):160405, 2007.

[165] D Dries, S. E. Pollack, J. M. Hitchcock, and R. G. Hulet. Dissipative transport of a Bose-Einstein condensate. *Phys. Rev. A*, 82(3):033603, 2010.

[166] Zin Lin, Joseph Schindler, Fred M. Ellis, and Tsampikos Kottos. Experimental observation of the dual behavior of PT-symmetric scattering. *Phys. Rev. A*, 85:050101, 2012.

[167] Sergey V. Dmitriev, Sergey V. Suchkov, Andrey A. Sukhorukov, and Yuri S. Kivshar. Scattering of linear and nonlinear waves in a waveguide array with a PT-symmetric defect. *Phys. Rev. A*, 84:013833, 2011.

[168] Sergey V Suchkov, Andrey A Sukhorukov, Sergey V Dmitriev, and Yuri S Kivshar. Scattering of the discrete solitons on the-symmetric defects. *EPL* , 100(5):54003, 2012.

[169] F Kh Abdullaev, VA Brazhnyi, and Mario Salerno. Scattering of gap solitons by pt-symmetric defects. *Phys. Rev. A*, 88(4):043829, 2013.

[170] S. M. Al-Marzoug. Scattering of solitons by complex pt symmetric Gaussian potentials. *Opt. Express*, 22(18):22080–22088, 2014.

[171] Roy H. Goodman, Philip J. Holmes, and Michael I. Weinstein. Strong nls soliton-defect interactions. *Physica D*, 192(3-4):215 – 248, 2004.

[172] Hidetsugu Sakaguchi and Mitsuaki Tamura. Scattering and trapping of nonlinear Schrodinger solitons in external potentials. *J. Phys. Soc. Jpn.*, 73(3):503–506, 2004.

[173] S. M. Al-Marzoug. Scattering of solitons by complex PT-symmetric gaussian potentials. *Opt. Express*, 22(18):22080–22088, 2014.

[174] X. Q. Li, X. Z. Zhang, G. Zhang, and Z. Song. Asymmetric transmission through a flux-controlled non-Hermitian scattering center. *Phys. Rev. A*, 91:032101, 2015.

[175] U. Al Khawaja, S. M. Al-Marzoug, H. Bahlouli, and Yuri S. Kivshar. Unidirectional soliton flows in PT-symmetric potentials. *Phys. Rev. A*, 88:023830, 2013.

[176] Hamidreza Ramezani, Tsampikos Kottos, Ramy El-Ganainy, and Demetrios N. Christodoulides. Unidirectional nonlinear PT-symmetric optical structures. *Phys. Rev. A*, 82:043803, 2010.

[177] Zhenya Yan, Zichao Wen, and Chao Hang. Spatial solitons and stability in self-focusing and defocusing kerr nonlinear media with generalized parity-time-symmetric Scarff-II potentials. *Phys. Rev. E*, 92:022913, 2015.

[178] Bikashkali Midya and Rajkumar Roychoudhury. Nonlinear localized modes in $\mathcal{PT}$-symmetric Rosen-Morse potential wells. *Phys. Rev. A*, 87:045803, 2013.

[179] Dmitry A. Zezyulin and Vladimir V. Konotop. Nonlinear modes in the harmonic PT-symmetric potential. *Phys. Rev. A*, 85:043840, 2012.

[180] Bikashkali Midya. Analytical stable Gaussian soliton supported by a parity-time symmetric potential with power-law nonlinearity. *Nonlinear Dyn.*, 79(1):409–415, 2014.

[181] Alexandre B. Tacla and Carlton M. Caves. Entanglement-based perturbation theory for highly anisotropic Bose-Einstein condensates. *Phys. Rev. A*, 84:053606, 2011.

[182] D. S. Petrov, G. V. Shlyapnikov, and J. T. M. Walraven. Regimes of Quantum Degeneracy in Trapped 1 D Gases. *Phys. Rev. Lett.*, 85:3745–3749, 2000.

[183] M. Olshanii. Atomic Scattering in the Presence of an External Confinement and a Gas of Impenetrable Bosons. *Phys. Rev. Lett.*, 81:938–941, 1998.

[184] I. V. Barashenkov, D. E. Pelinovsky, and E. V. Zemlyanaya. Vibrations and oscillatory instabilities of gap solitons. *Phys. Rev. Lett.*, 80:5117–5120, 1998.

[185] A Weller, J. P. Ronzheimer, C Gross, J Esteve, M. K. Oberthaler, D. J. Frantzeskakis, G Theocharis, and P. G. Kevrekidis. Experimental observation of oscillating and interacting matter wave dark solitons. *Phys. Rev. Lett.*, 101(13):130401, 2008.

[186] S. Burger, K. Bongs, S. Dettmer, W. Ertmer, K. Sengstock, A. Sanpera, G. V. Shlyapnikov, and M. Lewenstein. Dark solitons in Bose-Einstein condensates. *Phys. Rev. Lett.*, 83:5198–5201, 1999.

[187] D. S. Jin, J. R. Ensher, M. R. Matthews, C. E. Wieman, and E. A. Cornell. Collective excitations of a Bose-Einstein condensate in a dilute gas. *Phys. Rev. Lett.*, 77(3):420, 1996.

[188] D. M. Stamper-Kurn, H-J Miesner, S Inouye, MR Andrews, and W Ketterle. Collisionless and hydrodynamic excitations of a Bose-Einstein condensate. *Phys. Rev. Lett.*, 81(3):500, 1998.

[189] M.-O. Mewes, M. R. Andrews, N. J. van Druten, D. M. Kurn, D. S. Durfee, and W. Ketterle. Bose-Einstein condensation in a tightly confining dc magnetic trap. *Phys. Rev. Lett.*, 77:416–419, 1996.

[190] Frédéric Chevy, Vincent Bretin, Peter Rosenbusch, KW Madison, and Jean Dalibard. Transverse breathing mode of an elongated Bose-Einstein condensate. *Phys. Rev. Lett.*, 88(25):250402, 2002.

[191] H Ott, J Fortágh, S Kraft, A Günther, D Komma, and C Zimmermann. Nonlinear dynamics of a Bose-Einstein condensate in a magnetic waveguide. *Phys. Rev. Lett.*, 91(4):040402, 2003.

[192] M. H. Anderson, J. R. Ensher, M. R. Matthews, C. E. Wieman, and E. A. Cornell. Observation of Bose-Einstein condensation in a dilute atomic vapor. *Science*, 269(5221):198–201, 1995.

[193] K. B. Davis, M. O. Mewes, M. R. Andrews, N. J. van Druten, D. S. Durfee, D. M. Kurn, and W. Ketterle. Bose-Einstein condensation in a gas of sodium atoms. *Phys. Rev. Lett.*, 75:3969–3973, 1995.

[194] Scott E Pollack, D Dries, Mark Junker, Y. P. Chen, T. A. Corcovilos, and R. G. Hulet. Extreme tunability of interactions in a lithium-7 Bose-Einstein condensate. *Phys. Rev. Lett.*, 102(9):090402, 2009.

[195] S. E. Pollack, D Dries, R. G. Hulet, K. M. F. Magalhaes, E. A. L. Henn, E. R. F. Ramos, M. A. Caracanhas, and Vanderlei Salvador Bagnato. Collective excitation of a Bose-Einstein condensate by modulation of the atomic scattering length. *Phys. Rev. A*, 81(5):053627, 2010.

[196] S Sabari, R Vasantha Jayakantha Raja, K Porsezian, and P Muruganandam. Stability of trapless Bose-Einstein condensates with two- and three-body interactions. *J. Phys. B: Atomic, Molecular and Optical Physics*, 43(12):125302, 2010.

[197] Ivana Vidanović, Antun Balaž, Hamid Al-Jibbouri, and Axel Pelster. Nonlinear Bose-Einstein condensate dynamics induced by a har-

monic modulation of the s-wave scattering length. *Phys. Rev. A*, 84(1):013618, 2011.

[198] Alexandru I Nicolin. Faraday waves in Bose-Einstein condensates subject to anisotropic transverse confinement. *Rom. Rep. Phys*, 63(1329):7, 2011.

[199] William Cairncross and Axel Pelster. Parametric resonance in Bose-Einstein condensates. *arXiv preprint arXiv:1209.3148*, 2012.

[200] Mark Edwards, P. A. Ruprecht, K Burnett, R. J. Dodd, and Charles W Clark. Collective excitations of atomic Bose-Einstein condensates. *Phys. Rev. Lett.*, 77(9):1671, 1996.

[201] Sandro Stringari. Collective excitations of a trapped Bose-condensed gas. *Phys. Rev. Lett.*, 77(12):2360, 1996.

[202] Mark Edwards, R. J. Dodd, Charles W Clark, and K Burnett. Zero-temperature, mean-field theory of atomic Bose-Einstein condensates. *National Institute of Standards and Technology, Journal of Research*, 101(4):553–565, 1996.

[203] K. G. Singh and D. S. Rokhsar. Collective excitations of a confined Bose condensate. *Phys. Rev. Lett.*, 77(9):1667, 1996.

[204] Li You, W Hoston, and M Lewenstein. Low-energy excitations of trapped Bose condensates. *Phys. Rev. A*, 55(3):R1581, 1997.

[205] F Dalfovo, C Minniti, and L. P. Pitaevskii. Frequency shift and mode coupling in the nonlinear dynamics of a Bose-condensed gas. *Phys. Rev. A*, 56(6):4855, 1997.

[206] Ivana Vidanović, Hamid Al-Jibbouri, Antun Balaž, and Axel Pelster. Parametric and geometric resonances of collective oscillation

modes in Bose-Einstein condensates. *Phys. Scripta*, 2012(T149):014003, 2012.

[207] Hamid Al-Jibbouri, Ivana Vidanović, Antun Balaž, and Axel Pelster. Geometric resonances in Bose-Einstein condensates with two-and three-body interactions. *J. Phys. B: Atomic, Molecular and Optical Physics*, 46(6):065303, 2013.

[208] G Hechenblaikner, O. M. Marago, E Hodby, J Arlt, S Hopkins, and CJ Foot. Observation of harmonic generation and nonlinear coupling in the collective dynamics of a Bose-Einstein condensate. *Phys. Rev. Lett.* , 85(4):692, 2000.

[209] G Hechenblaikner, S. A. Morgan, E Hodby, O. M. Maragò, and C. J. Foot. Calculation of mode coupling for quadrupole excitations in a Bose-Einstein condenstate. *Phys. Rev. A*, 65(3):033612, 2002.

[210] L. P. Pitaevskii and S Stringari. Landau damping in dilute Bose gases. *Phys. Lett. A*, 235(4):398–402, 1997.

[211] L. P. Pitaevskii. Phenomenological theory of mode collapse-revival in a confined Bose gas. *Phys. Lett. A*, 229(6):406–410, 1997.

[212] R Graham, D. F. Walls, M. J. Collett, M Fliesser, and Ewan M Wright. Collapses and revivals of collective excitations in trapped Bose condensates. *Phys. Rev. A*, 57(1):503, 1998.

[213] G. Edward Marti, Ryan Olf, and Dan M. Stamper-Kurn. Collective excitation interferometry with a toroidal Bose-Einstein condensate. *Phys. Rev. A*, 91:013602, 2015.

[214] A. Görlitz, J. M. Vogels, A. E. Leanhardt, C. Raman, T. L. Gustavson, J. R. Abo-Shaeer, A. P. Chikkatur, S. Gupta, S. Inouye,

T. Rosenband, and W. Ketterle. Realization of Bose-Einstein condensates in lower dimensions. *Phys. Rev. Lett.*, 87:130402, 2001.

[215] F. Schreck, L. Khaykovich, K. L. Corwin, G. Ferrari, T. Bourdel, J. Cubizolles, and C. Salomon. Quasipure Bose-Einstein condensate immersed in a fermi sea. *Phys. Rev. Lett.*, 87:080403, 2001.

[216] S. Dettmer, D. Hellweg, P. Ryytty, J. J. Arlt, W. Ertmer, K. Sengstock, D. S. Petrov, G. V. Shlyapnikov, H. Kreutzmann, L. Santos, and M. Lewenstein. Observation of phase fluctuations in elongated Bose-Einstein condensates. *Phys. Rev. Lett.*, 87:160406, 2001.

[217] Guan-Qiang Li, Li-Bin Fu, Ju-Kui Xue, Xu-Zong Chen, and Jie Liu. Collective excitations of a Bose-Einstein condensate in an anharmonic trap. *Phys. Rev. A*, 74:055601, 2006.

[218] Ji-Xuan Hou. Collective excitations of a 1D Bose-Eeinstein condensate in an anharmonic trap. *Phys. Lett. A*, 368(5):366 – 370, 2007.

[219] Li Guan-Qiang, Peng Ping, Liu Jian-Ke, and Xue Ju-Kui. Collective excitations and nonlinear dynamics of 1d bec with two-and three-body interactions in anharmonic traps. *Commun. Theor. Phys.*, 50(5):1129, 2008.

[220] Li Hao-Cai, Chen Hai-Jun, and Xue Ju-Kui. Bose-Einstein condensates with two-and three-body interactions in an anharmonic trap at finite temperature. *Chin. Phys. Lett.*, 27(3):030304, 2010.

[221] Nir Navon, Swann Piatecki, Kenneth Günter, Benno Rem, Trong Canh Nguyen, Frédéric Chevy, Werner Krauth, and Christophe Salomon. Dynamics and thermodynamics of the low-temperature strongly interacting Bose gas. *Phys. Rev. Lett.*, 107(13):135301, 2011.

[222] Janne Ruostekoski and Dan F Walls. Bose-Einstein condensate in a double-well potential as an open quantum system. *Phys. Rev. A*, 58(1):R50, 1998.

[223] A Gammal, T Frederico, Lauro Tomio, and F Kh Abdullaev. Stability analysis of the d-dimensional nonlinear Schrödinger equation with trap and two-and three-body interactions. *Phys. Lett. A*, 267(5):305–311, 2000.

[224] S. M. Al-Marzoug. Scattering of solitons by complex pt symmetric Gaussian potentials. *Opt. Express*, 22(18):22080–22088, 2014.

[225] E Wamba, S Sabari, K Porsezian, A Mohamadou, and TC Kofané. Dynamical instability of a Bose-Einstein condensate with higher-order interactions in an optical potential through a variational approach. *Phys. Rev. E*, 89(5):052917, 2014.

[226] Etienne Wamba, Alidou Mohamadou, and Timoléon C Kofané. A variational approach to the modulational instability of a Bose-Einstein condensate in a parabolic trap. *J. Phys. B: Atomic, Molecular and Optical Physics*, 41(22):225403, 2008.

[227] Juan J Garcı, Vladimir V Konotop, Boris Malomed, et al. A quasi-local Gross–Pitaevskii equation for attractive Bose-Einstein condensates. *Mathematics and Computers in Simulation*, 62(1):21–30, 2003.

[228] T. D. Lee, Kerson Huang, and C. N. Yang. Eigenvalues and eigenfunctions of a Bose system of hard spheres and its low-temperature properties. *Phys. Rev.*, 106:1135–1145, 1957.

[229] Haixiang Fu, Yuzhu Wang, and Bo Gao. Beyond the fermi pseudopotential: A modified Gross-Pitaevskii equation. *Phys. Rev. A*, 67:053612, 2003.

[230] Eric Braaten, H.-W. Hammer, and Thomas Mehen. Dilute Bose-Einstein condensate with large scattering length. *Phys. Rev. Lett.*, 88:040401, 2002.

[231] A. Braaten, E.and Nieto. Quantum corrections to the energy density of a homogeneous Bose gas. *EPJ B- Condensed Matter and Complex Systems*, 11(1):143–159, 1999.

[232] G Theocharis, PG Kevrekidis, MK Oberthaler, and DJ Frantzeskakis. Dark matter-wave solitons in the dimensionality crossover. *Phys. Rev. A*, 76(4):045601, 2007.

[233] Kunal K Das. Highly anisotropic Bose-Einstein condensates: Crossover to lower dimensionality. *Phys. Rev. A*, 66(5):053612, 2002.

[234] Abdelâali Boudjemâa. Bose polaronic soliton-molecule and vector solitons in PT-symmetric potential. *j.cnsns*, 48:376–386, 2017.

[235] N. Bender, S. Factor, J. D. Bodyfelt, H. Ramezani, D. N. Christodoulides, F. M. Ellis, and T. Kottos. Observation of asymmetric transport in structures with active nonlinearities. *Phys. Rev. Lett.*, 110:234101, 2013.

[236] Joseph Schindler, Ang Li, Mei C. Zheng, F. M. Ellis, and Tsampikos Kottos. Experimental study of active LRC circuits with PT symmetries. *Phys. Rev. A*, 84:040101, 2011.

[237] Ali Mostafazadeh. Pseudo-Hermiticity versus pt symmetry: The necessary condition for the reality of the spectrum of a non-Hermitian Hamiltonian. *J. Math. Phys.*, 43(1):205–214, 2002.

[238] Shin Inouye, Tilman Pfau, Subhadeep Gupta, AP Chikkatur, A Görlitz, DE Pritchard, and Wolfgang Ketterle. Phase-coherent amplification of atomic matter waves. *Nature*, 402(6762):641–644, 1999.

[239] T Schumm, S Hofferberth, L Mauritz Andersson, S Wildermuth, S Groth, I Bar-Joseph, J Schmiedmayer, and P Krüger. Matter-wave interferometry in a double well on an atom chip. *Nature physics*, 1(1):57–62, 2005.

[240] T. P. Billam, S. L. Cornish, and S. A. Gardiner. Realizing bright-matter-wave-soliton collisions with controlled relative phase. *Phys. Rev. A*, 83:041602, 2011.